SMART MATERIALS FOR STRUCTURAL HEALTH MONITORING

Belinda-Lee Verijenko

Submitted in fulfilment of the requirements for a Doctoral degree.

20 January 2003

Supervisor: Professor S Adali

School of Mechanical Engineering

University of Natal

ABSTRACT

A new philosophy in structural health monitoring was explored, with the view to the creation of a smart mining bolt: one which would bear the normal load of any bolt used in South African gold mining tunnels, but at the same time be capable of monitoring its own level of damage. To this end, a survey of various smart materials currently used in structural health monitoring applications, was conducted, and a group known as strain memory alloys isolated as holding the most promise in this regard.

Strain memory alloys give an indication of peak strain based on an irreversible transformation from paramagnetic austenite to ferromagnetic martensite, which occurs in direct proportion to the amount of strain experienced by the material. A measurement of magnetic permeability can therefore be correlated to peak strain. An extensive study of the alloying chemistry, material processing and transformation characteristics was therefore carried out, including an analytical model for the quantification of the energy associated with martensitic nucleation, at a dislocation-disclination level.

The conditions within typical South African gold mining tunnels were evaluated, and a smart mining bolt design produced, based on the loading and environmental conditions present. Several material formulations were then proposed, melted, tested and evaluated against the relevant strength, corrosion and transformation criteria. A suitable material was selected and further tested. A working prototype bolt has been produced, and in situ tests of complete bolts, are scheduled to take place shortly.

ACKNOWLEDGEMENTS

For my husband: thank you for your support, your constant motivation, and your sacrificial heart – without you I would have never seen this through.

Heartfelt thanks and appreciation belong also to my parents: you made me who I am, and gave me the belief that I could climb any mountain.

And, lastly, but definitely not least, thank you to all the colleagues who have made contributions in some form or another to the successful completion of this research.

TABLE OF CONTENTS

LIST OF FIGURES

Chapter 5

Chapter 6

LIST OF TABLES

INTRODUCTION

In a world where aging infrastructure litters the landscape, and cutting edge technology demands on materials and structures are ever-growing, the need to monitor the health of critical structures, becomes one of paramount importance. This notion of periodically monitoring the state of safety critical equipment is by no means new. An entire branch of science owes its existence to the need to predict failure, and safely avoid it, but in the modern world where resources are limited and it is necessary to extend the life of structures beyond their intended limits, it is no longer feasible to rely merely on calculation of safe life intervals, and the prediction of possible crack initiation sites. It becomes necessary to know "the numbers", to have a picture of the stresses and strains experienced by any given structure.

There are currently many methods available for determining the presence of cracks, corrosion, localized damage etc. but where previously most non-destructive testing required equipment to be de-commissioned, or taken out of service, in order to carry out inspection, a new thrust in the market develops towards permanently attaching sensors to structures so that they can be continuously monitored. In this drive towards integrated systems, a variety of smart materials have found employment within these permanently attached sensors, including shape memory alloys, piezoelectrics, electrostrictive materials, magnetostrictive materials, electrorheologoical and magnetorheological fluids, and strain memory alloys.

Although, the attachment of sensors to structures for continuous monitoring is an important problem, which has received much attention [1,2,3], a new philosophy in the area of structural health monitoring begins to emerge: that of smart components. By constructing a component is such a way that it will be manufactured with the ability to monitor its own level of damage, much maintenance time and cost can be saved, which adds to the intrinsic advantages of structural health monitoring.

The aim of this research was to investigate the feasibility of creating a functioning smart component. As a candidate application, the problem of structural health in South African mining tunnels was considered. Because mining forms one of the major economic activities within the country, many thousands of people are employed to work at depths of up to 3700m below ground level. The safety of these people is dependent on the structural integrity of the haulage tunnels through which they move on a daily basis. These tunnels are subjected to high stress levels and seismic events, and are prone to collapse without warning, but at present there is no means of quantitatively assessing tunnel health. It is for this reason that a smart roof bolt was

1

proposed. Roof bolts are currently used to restrain and support the fractured rock mass of tunnel walls. The creation of a smart mining bolt capable of measuring its own level of deformation (caused by rock dilation and movement) would then give a picture of stresses and unseen rock movements within tunnel walls. This proposal produced a multi-disciplinary problem involving design, structural evaluation, manufacturing considerations, and most importantly the formulation of a material suitable to meet all the requirements (including cost) of the component.

In order to accomplish the task at hand, a survey of smart materials was conducted, and a group known as strain memory alloys (which encompass metastable alloys and TRIP steels) was identified to hold promise in this regard. Strain memory alloys, as the name suggests, give a measure of the strain (deformation) experienced by the material. This is accomplished by means of a crystallographic transformation from paramagnetic austenite (FCC) to ferromagnetic martensite (BCC), which proceeds on application of (and in direct proportion to) strain. A measurement of the magnetic permeability of the material can therefore be correlated to the amount of strain experienced by the material.

An in depth study of previous work in the field of metastable alloys was therefore required including alloying chemistry, processing, and transformation characteristics. Of paramount importance are the micromechanisms involved in transformation. If the influences on this parameter can be quantified, at a crystal lattice level, then the transformation characteristics of any candidate material become a controllable parameter, which can be accurately manipulated to provide damage information. In this regard, an analytical model of martensitic transformation mechanics including the energies involved due to thermal and strain contributions is considered.

Finally, several candidate materials are required to be formulated and evaluated against strength, cost, machinability, corrosion resistance, and transformation criteria. A prototype bolt, complete with damage extraction reading is to be produced and tested, but particular focus rests on the formulation, and testing of an appropriate material.

CHAPTER 1

STRUCTURAL HEALTH MONITORING

Since the beginning of the industrial revolution, there has been a need to quantify the health or remaining life of safety critical structures. From this need has developed a whole field of non-destructive testing techniques [4], and more recently, what has become known as structural health monitoring. Many of the techniques used in non-destructive testing may be adapted for use in the structural health monitoring field, but the fundamental differences between the two approaches lie in the methods of data acquisition.

Non-destructive testing (NDT) techniques vary from simple procedures for checking the presence of surface cracks, such as the die penetrant method, through to more complex techniques for the checking of internal flaws such as ultrasound, and eddy current methods. The common principle linking all non-destructive testing methods though, is the need to remove the structure from service in order to place sensors, make a direct measurement, and then assess damage. For this inspection procedure, trained personnel are usually required. In more recent years, there has been a swing away from this traditional approach of non-destructive testing, towards what is known as Structural Health Monitoring (SHM).

In contrast to traditional NDT, SHM seeks to monitor the health of a structure in-service [5,6,7]. Sensors are permanently attached onto the structure, or are placed within it. These may then be monitored on a continual basis, either remotely or physically. Quite often an assessment of accumulated damage is made on the basis of comparative readings (i.e.: a history). This philosophy then eliminates the need for equipment downtime, and provides a much better picture of overall structural health. The modification of traditional NDT methods for incorporation into SHM systems has also received a fair amount of attention, and such methods as Lamb waves, acoustic emission, modal analysis and ultrasonics can all be integrated into an automated SHM system [8].

Benefits of SHM therefore include the reduction of down-time, the reduction of human involvement, and the automation of data acquisition and analysis. All of which reduce the costs associated with determining the level of damage in a given structure.

1.1 Current methodologies in structural health monitoring

Structural health monitoring systems can be broadly divided into two categories: those that are active in nature and those that are passive in nature. The differences between the two categories can be best seen in the comparative table below [1,2,3,9-18]:

Table 1.1: Comparison of the active and passive structural health monitoring methodologies.

Active systems	Passive systems
Full-time power is required, and in the event of power failure, data will be lost.	Power is only required during sensor interrogation, and in the event of power failure, data is held safely within the sensor itself.
Active systems give instantaneous information and require a full time-history.	Passive systems are peak systems, that is, they record only successively higher levels of damage, i.e.: peak damage.
Data is continuously monitored and stored in an extensive data storage system.	Data is usually only interrogated after significant events, or at relevant time periods, but may be set up for continuous monitoring.
Extensive data reduction is usually required before analysis and health diagnosis	Minimal data reduction is required to analyse and subsequently diagnose health.
Some active sensors may also act in an actuator capacity, that is: they may be used to rectify damage or changes in the structure instead of only measuring damage [11,19].	Some passive systems may be set up to provide some stiffening in the presence of damage, but do not possess the same advantage of being able to actively control damage levels [20].
These systems are costly but highly accurate, suitable for laboratory conditions or where weather and environmental conditions are not likely to cause problems	Much less expensive, capable of detecting minute, gradual changes within a structure. These systems are also robust and suitable for outdoors environments.
Examples of active sensors are: Resistive strain gages Vibrating wire strain gages Piezoelectric transducers [9]	Examples of passive sensors are: TRIP gages (using strain memory alloys) Mechatronic gages Fibre Optic sensors [9]

A hybrid system may also be created wherein a passive sensor is coupled with a semi-active sensor, thereby making available current instantaneous information, as well as peak damage information. An example of such a system is one implemented on some railway bridges in the United States [1] where hybrid sensors are placed on the relevant bridge joints, and interrogated only at times of train crossing. In this way transport officials receive current information regarding load/deformation as well as the peak, accumulated damage in the bridge.

The choice of structural health monitoring system can be seen to be governed by a number of factors, including cost, accuracy, ruggedness, and information/control requirements. In situations where control as well as monitoring is required of the system, the active option must be chosen. For example, several researchers have had success with controlling damage in carbon reinforced plastic (composite) panels, by the embedding of films or ribbons of various smart materials such as piezoelectrics, electrostrictive and magnetostrictive materials, and shape memory alloys [11,19,21,22]. In this case the smart material sensors were not only used in a damage assessment capacity, but also in a damage correction capacity – materials such as these can even be used to generate an out-of-phase stress field to reduce fatigue stress and strain amplitude, thereby limiting fatigue damage.

In many other situations, however, passive technology is far more practical, and cost effective. It is only recently though, that passive sensors have seen development and use in any significant proportion compared to the market segments occupied by the traditional NDT and active SHM streams.

A complete Structural Health Monitoring system consists of three parts:

1) The sensor itself. The type of measurement required will determine the sensor choice, but there is usually an array of sensors attached to a structure of appreciable size. These sensors may all measure the same parameter (just at different locations) or they may measure a variety of parameters such as temperature, radiation, deformation, and crack propagation. These sensors need to be attached to or integrated into the structure without compromising the efficient operation of the structure.

2) Signal Processing. The sensors will all generate signals that need to be processed and fed to the point where data is interpreted and damage assessment made. This may mean physical interrogation by personnel, or be a hard-wiring or remote link set-up depending on the physical accessibility of the structure and the budget of course.

3) Data processing and analysis.

The brief review of current SHM methodologies reveals a trend towards the use of smart materials in many areas of sensor technology. It therefore bears a slightly deeper investigation into the various kinds of smart materials in use.

1.2 Smart materials and their use in structural health monitoring

A smart material can be defined as one that has more than one co-ordinated response to a given input. What this means is that if one response is measured the other parameter can be directly predicted. Some of the more prominent smart materials and their application to sensor technology are discussed briefly in the following section.

1.2.1 Piezoelectricity

Piezoelectric behaviour [23-48] was first observed more than a century ago in specially prepared natural crystals. When a piezoelectric material is placed under mechanical stress, it produces a charge on the crystal surfaces. Conversely, when an electrical voltage is applied across the crystal, the physical dimensions change. This is illustrated in Figure 1.1 shown below.
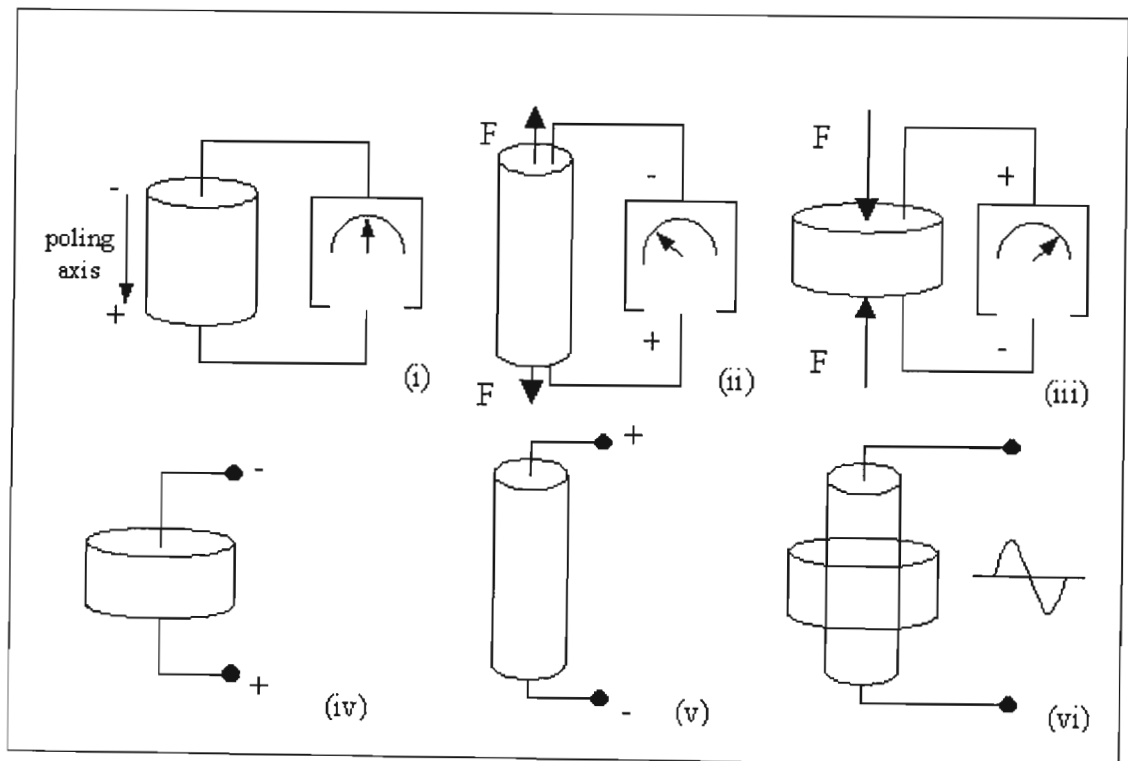
Figure 1. 1: The piezoelectric effect in a PZT crystal

A poling voltage is applied to the crystal (i). If a tensile force is then applied to the crystal (ii) the voltage produced by the crystal between the electrodes will be of opposite polarity to the

poling voltage; whereas, a compressive force (iii) will produce a voltage of the same polarity as the poling voltage. Likewise, if the voltage is applied to the crystal (iv and v) then corresponding physical dimension changes occur. If an alternating current is applied to the electrodes (as in figure (vi) of Figure 1.1) the physical dimensions of the crystal will change with the same frequency as the alternating current. Clearly the above behaviour makes piezoelectrics very useful for structural health monitoring, as they can be used as either transducers or actuators.

There are various physical, dielectric and piezoelectric properties that are used to characterise piezoelectric materials and compare their performance against one another. A summary of these properties is given in Table 1.2 below.

Table 1.2: Summary of the various properties of piezoelectric material [246].

Physical Properties	
Curie temperature	The temperature above which spontaneous polarisation and piezoelectric behaviour cease to exist.
Maximum operating temperature	The safe use temperature for piezoelectric materials to ensure continued piezoelectric behaviour. Generally, the operating temperature is 50-60% of the curie temperature.
Mechanical Q	A dimensionless number that describes the merit of the material as a harmonic oscillator. Q is the reciprocal of the mechanical damping factor.
Dielectric Properties	
Dielectric constant, K	This is the ratio of the amount of charge a material can store compared to the charge stored by a comparable vacuum. (Units of capacitance*length/area).
Dissipation factor	A measure of the electrical loss in the material. It is the ratio of the effective series resistance to the effective series reactance.
Ageing	The polarisation of the material gradually decreases with time. Ageing is the time decay given as a percentage per decade of time.
Piezoelectric Properties	
Coupling coefficient	A measure of converting electrical energy to mechanical energy, and vice versa. It is the square root of the ratio of stored electrical energy to the mechanical energy input.

Although the piezoelectric effect was first observed in specially cut natural crystals (of which 20 classes were found) it is possible to manufacture artificial crystals that display the same behaviour, and have dielectric constants up to 100 times higher. Piezoceramics are said to be

such a class of "artificial piezoelectrics" and are manufactured by sintering metallic oxide powders. They can be produced in a variety of different shapes, sizes and with tailored physical and piezoelectric properties.

Noteworthy materials displaying piezoelectric behaviour include:
- Quartz crystals
  - They are extremely stable, rugged and compact.
  - High material stress limit of ~140 MPa
  - Temperature resistance up to 500°C
  - Very high rigidity, high linearity and negligible hysteresis
  - Almost constant sensitivity over a wide temperature range
  - Ultra high insulation resistance (10^4 ohms)
- Lead zirconate titanate (PZT)
  - There are many variants of PZT, both hard and soft
  - PZT has excellent machinability
  - High dielectric strength
  - High mechanical strength
  - Optical transparency available
- Polyvinylidene fluoride (PVDF)
- Lead metaniobate
- Bismuth titanate
- Barium titanate

Piezoelectric materials have found application in many fields including such diverse applications as ultra-high-fidelity stereo speakers and vibration damping on snow skis. But specifically pertaining to structural health monitoring systems, piezoelectric materials are currently used in transducers for measuring pressure, force and acceleration. These transducers may be regarded as under-damped spring-mass systems with a single degree of freedom. They are modelled by the classical second order differential equation whose solution is:

$$\frac{a_o}{a_b} \cong \frac{1}{\sqrt{\left[1-\left(\frac{\omega}{\omega_n}\right)^2\right]^2 + \left(\frac{1}{Q^2}\right)\left(\frac{\omega}{\omega_n}\right)^2}} \tag{1.1}$$

where:

ω_n = undamped natural (resonant) frequency

ω = frequency at any given point on the curve

a_0 = output acceleration

a_b = mounting base or reference acceleration

Q = factor of amplitude increase at resonance

Quartz transducers have Q of around 10 to 40, hence:

$$\text{Phase lag} \cong \frac{60}{Q}\left(\frac{\omega}{\omega_n}\right) \text{ for } \left(\frac{\omega}{\omega_n}\right) \leq \frac{2}{5} \qquad (1.2)$$

It must be said that piezoelectric materials can only really be used in active SHM systems. Since transducers based on these materials only experience an electrical output when there is a change in load, truly static measurements cannot be made. They are however useful in situations where both transducer and actuator are required such as mentioned in section 1.1.

1.2.2 Electrostriction

Electrostrictive materials [49-61] may be considered similar to piezoelectric materials in that they display a displacement proportional to applied electric field, but there are a couple of noticeable differences between the two classes of material. The first of these differences lies in the fact that electrostrictive materials display displacement or strain proportional to the square of the applied electric field, and the second is that they do not possess any spontaneous polarisation. These fundamental differences can most clearly be illustrated in Figure 1.2 below which compares piezoelectric and electrostrictive material behaviour.

It can be clearly seen that piezoelectric materials are able to either contract or expand, depending on the direction of the applied voltage. Electrostrictive materials, however, operate on the principle that the electric field separates positively and negatively charged ions, thereby causing an expansion of a material cell, and therefore an overall expansion.

Electrostrictive materials include:

> Lead magnesium niobate (PMN)
> Polyurethane
> Polyether
> Amorphous polybutadiene
> Poly(dimethylsiloxane)
> Liquid crystal elastomers
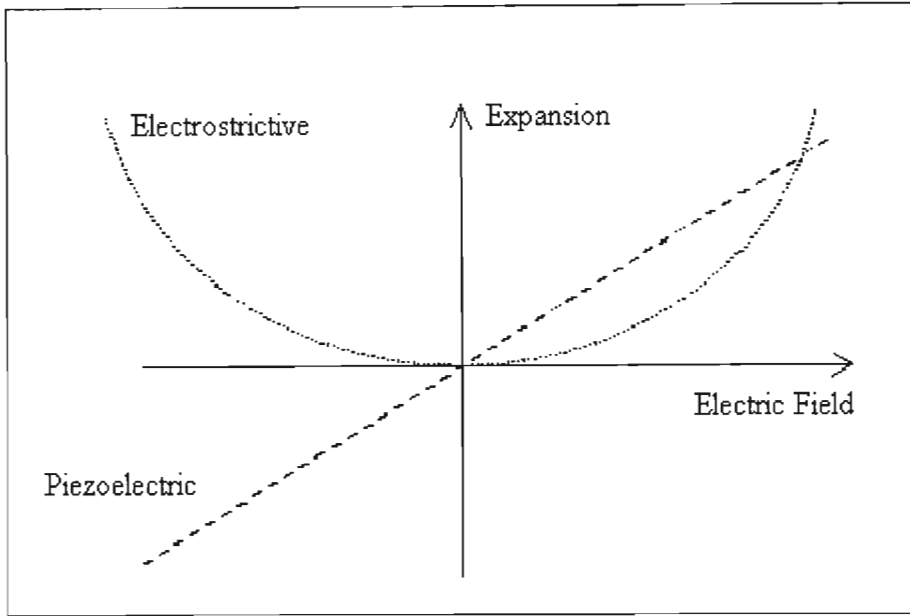
Figure 1. 2: Expansion of piezoelectric and electrostrictive materials vs electric field.

If one compares the most common piezoelectric material (PZT) with a common electrostrictive material (PMN) the differences in the capabilities of the two material classes becomes obvious.

Table 1.3: Comparison of PZT and PMN materials.

Piezoelectric (PZT)	Electrostrictive (PMN)
PZT ceramics are actually isotropic until a poling voltage is applied, at which point they become aniostropic and behave like piezoelectrics.	PMN materials change length proportional to the square of the applied voltage.
Creep ranges up to 15% in PZT. See the graph below for a comparison.	PMN is unpoled and therefore more stable, so that long term creep is kept to much lower levels.
Both materials are susceptible to hysteresis.	Electrostrictive materials experience much less hysteresis.
PZT has a much more constant expansion coefficient over a large variety of temperatures	PMN has a better coefficient of thermal expansion

While coefficients such as the dielectric, coupling and compliance constants are easily defined for piezoelectrics, the situation is not so straightforward for electrostrictive materials, since the

material is non-linear. It is however possible to use electrostrictive materials in certain structural health monitoring applications where compression will not be experienced. Since they have low hysteresis and are available in various sizes and geometries, they can find specialised application in for example active vibration control of thin plates.

1.2.3 Magnetostriction

Certain ferromagnetic materials display a property known as magnetostriction, [62-72] or a change in shape when a magnetic field is applied. Of particular interest in this class of materials is one known as Terfenol-D. An engineered material, Terfenol-D contains iron, terbium and dysprosium (the latter two being rare earth elements) and displays magnetostrictive properties far superior to other known materials in this class. It boasts a change in length of more than 0,1% when exposed to a magnetic field of 500 oersted. This combined with wide bandwidth, and microsecond response, make Terfenol-D a very useful but expensive smart material. It is currently produced in a variety of shapes including thin films, monoliths, and powder for composite applications.

Magnetostrictive materials such as Terfenol-D have found application in many areas, including industrial vibrators, tomography, robotics, and space structures [9,73]. As a structural health monitoring sensor, magnetostrictive materials could be used in an active or passive configuration. An example of an active system is what is known as a non-contact torque sensor: a thin film or ribbon is wrapped around the specimen that is subjected to some sort of torque. The change in magnetic induction is then related to the torque on the specimen. Another example of the use of magnetostrictive material used in combination with other smart sensors is that of fibre optic magnetic field sensors. In this case the change in length of a magnetostrictive element (in the presence of a magnetic field) is used to change the optical path length of a fibre optic sensor.

The only disadvantage hampering the greater use of magnetostrictive materials, lies in their cost.

All of the materials mentioned in the preceding sections are well developed, and substantial research has been conducted to produce commercially viable products utilising their individual unique capabilities. Their use in sensing technologies or as part of SHM systems is well-documented, and thoroughly tested. There is, however, one more group of smart materials that has not been as well documented or researched as all the rest. This material forms the basis for a new philosophy of structural health monitoring.

1.3 A new philosophy in structural health monitoring

Until recently, research in the area of structural health monitoring has focused almost entirely on accomplishing structural health interrogation by means of attaching permanent sensors to a structure and either actively or passively monitoring those sensors. A new approach that has recently emerged involves using a smart material as a structural component or a section of a structure. That is, a smart structure is produced – one that bears the normal load but has the added capacity to monitor its own level of damage.

There are very few currently available smart materials that could act in this dual role of load-bearing and self-sensing, not only from a strength perspective, but also a cost consideration. One group of materials that does fit the bill, however, is that known as <u>strain memory alloys</u>. Fundamentally, these are metastable alloys with an austenitic crystal structure at room temperature. Upon application of strain, however, this austenite is transformed to martensite. Provided that the temperature is kept reasonably constant, the transformation occurs at a rate directly proportional to the amount of strain applied to the material. Because the austenite is paramagnetic, and the α martensite is ferromagnetic, a measurement of the change in magnetic behaviour, will therefore provide an indication of strain. This correlation between strain and volume fraction of martensite is illustrated in Figure 1.3 below. It is particularly useful that the slope and incubation strain (see Figure 1.3) can be tailored through chemistry and processing to almost any desired sensitivity.

Strain memory alloys have already found application in sensing technology [9,74] but the stronger classes such as TRIP steel, may be used in load-bearing applications as well [20,75,76,77]. Originally developed as a replacement for ultra high strength low alloy steels, TRIP (TRansformation Induced Plasticity) steels possess extraordinary combinations of strength and ductility, brought about by the transformation from austenite to martensite. This formation of martensite delays the onset of necking in a tensile test: the inclination to produce a localised contraction in the tensile test piece triggers the transformation in that region. The transformation then slowly spreads along the gage length, moving outwards from the centre, until the whole specimen is martensitic. The specimen then fractures at the UTS of the martensitic phase. This same mechanism can be used to prevent the propagation of micro-cracks, since the formation of martensite at the tip of the crack relaxes the stress concentration and suppresses further propagation [78]. It was research into this group of metastable alloys that first produced the notion of constructing smart components [20].
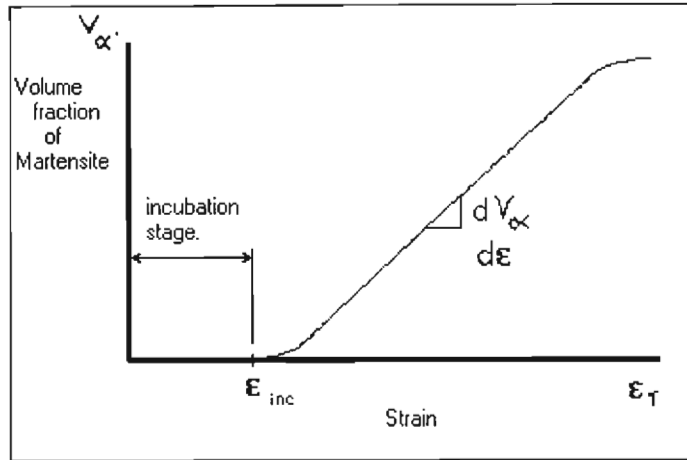
Figure 1. 3: The development of martensite, dependent on strain

The irreversible transformation from paramagnetic austenite to ferromagnetic martensite means that only successively higher strain readings will be registered within the crystal structure of the material. An indication of peak strain encountered by the material is therefore available to the engineer. Shown below in Figure 1.4 is the operation of a sensor that uses a strain memory alloy element as its strain indicator.
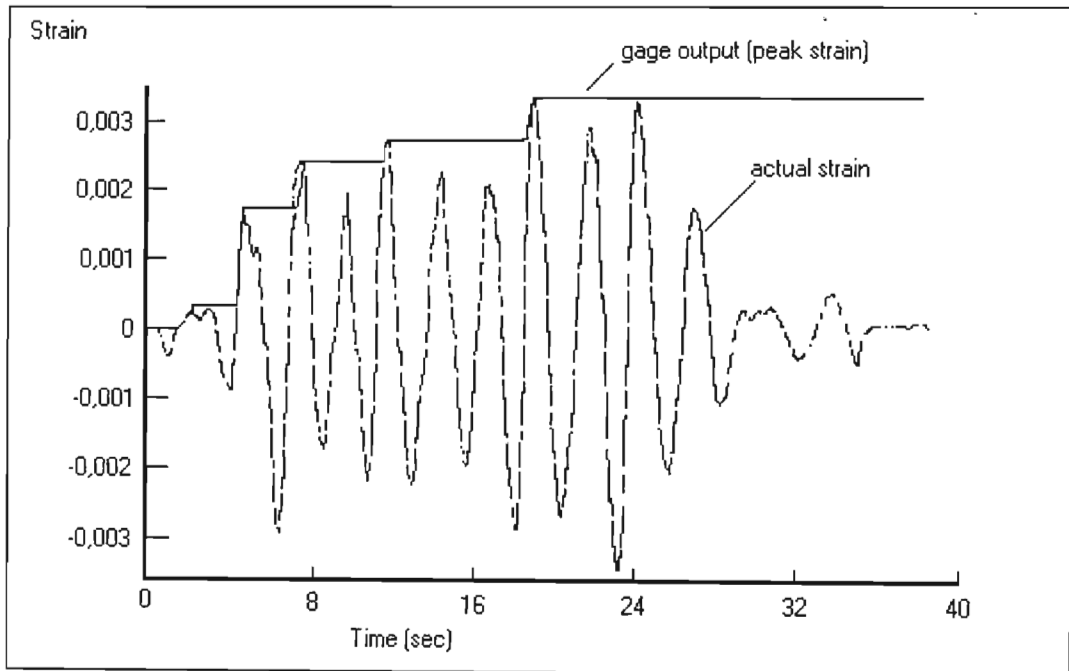
Figure 1. 4: The operation of a passive peak sensor based in strain memory alloys

The above sensor takes readings in the absence of any power, in fact the only time during which power will be required is the short period while the material is interrogated to check levels of

magnetism and this power will be required only inside the interrogation instrument. In the case of smart components, the measuring instrument may actually be integrated into the structure itself, if clever design methods are employed.

Although strain sensors based on strain memory alloys have focused on measuring tensile strains, it is possible to measure compressive and shear deformations as well. It is not however possible to differentiate between tensile and compressive strains since the material is incapable of distinguishing one type of loading from another. In using this technology as a means of damage indication, two issues need to be considered, the first is that the type of loading the sensor or smart component will encounter must be known with some degree of certainty in order that a correlation between transformation and damage can be made; and the second requires the identification of the factors influencing transformation micromechanisms, so that transformation becomes a controllable parameter in material development.

The versatility, strength, and cost advantage of strain memory alloys make them ideal for a number of applications currently under investigation for commercial viability:

> Smart composite panels for use in windmill blades: thin metastable wires can be inserted into the composite weave at primary manufacturing stage, providing not only a stronger laminate, but also a diagnostic tool, in these structures which are susceptible to sudden, catastrophic failure.

> Smart Aircraft bolt: the bolts attaching the wings of a C130 aircraft must presently be inspected for damage by jacking up and removing the wings of the aircraft, an operation that takes more than 200 manhours each time it occurs as part of periodic routine maintenance. The use of a smart bolt constructed from TRIP steel, would mean that bolts could effectively be tested in situ with a probe, and replaced only if necessary.

> Smart re-bar: earthquake prone regions such as Japan and California need some means of assessing the effects of seismic activity on their civil infrastructure (bridges and buildings). Use of smart reinforcing rods would provide a cost-effective and easy means of providing peace of mind for communities in those regions.

The forthcoming chapters will present a study of how this technology was used to create a smart component aimed at improving safety within the South African mining industry, including the material development, a study of micromechanisms of transformation, as well as the actual prototype design, complete with sensing equipment for damage interrogation.

CHAPTER 2

STRUCTURAL HEALTH MONITORING IN SOUTH AFRICAN GOLD MINES

South Africa's largest export is gold, making gold mining one of the most crucial economic activities in the country. As such, many thousands of people are employed in the industry, a large proportion of whom spend their working day underground. The safety of these thousands of workers in the more than one hundred gold mines is of paramount importance. Every year approximately 800km of haulage tunnels are developed, at enormous cost, in fact many billions of Rands [79]. The movement of miners through these haulage tunnels gives the structural integrity of the tunnels one of the most important roles to play in guaranteeing the safety of all personnel who work underground. Tunnel health is therefore both a safety concern and a financial issue.

Because most of the tunnels in South African gold mines are at relatively great depths, the pressures experienced by these tunnels cause them to close over time, thereby requiring rehabilitation. Movement of rock slabs relative to one another in the walls of the tunnel can be unseen by the naked eye, but pose danger to tunnel integrity. Another danger lurks in the form of rockbursts caused by seismic events underground. These sudden "explosions" of pieces of tunnel wall effect great damage, and may even trap miners if they close the tunnel completely. The total lack of any means to quantify the unseen happenings within tunnel walls poses therefore the greatest threat to human life, and the greatest financial risk as well. A means of quantitatively measuring the structural health of tunnels would thus not only aid the engineer in forming a picture of the stresses in tunnel walls, but would also ensure that tunnels could have extra support added (relatively cheap) before collapse requires rehabilitation, which is expensive.

Current strategy for tunnel design and support is done on an empirical basis, simply due to the fact that many of the factors affecting tunnel stability are difficult to quantify and even more difficult to model analytically or numerically. The selection of support systems in any given situation (and conditions vary considerably) is therefore left largely to the experience and discretion of the rock engineer [80].

This notion of quantitatively monitoring the structural health (or stress state) of tunnels is by no means new. In fact the CSIR (South African Council of Scientific and Industrial Research –

division of mining technology) commissioned a study to determine the requirements for instituting a cost effective in situ stress measurement program. Some of the requirements [81,82] identified can be summarised as follows:

1. The technique should be undemanding on the requirement for services provided by the mine. This would mean no water or cable-fed power; and as little impact as possible on mining production, exploration operations, and time input of personnel.
2. The technique must be low cost in regard to all aspects; that is, cost of preparation, installation, instrumentation, and measurement time.
3. Many measurements should be made in a single shift
4. Flexibility in taking measurements would also be an important criteria – the time required for preparation (to take a measurement) should be a small as possible, and measurements should be possible in excavations of limited size.
5. The technique employed should preferably not require the retrieval of rock cores and laboratory testing to determine deformation properties of the rock mass.
6. And, lastly, the technique should be immune to the harsh conditions that exist underground.

This may seem like quite a rigorous list of requirements for the implementation of structural health monitoring, but the reality of the underground environment, and the operational environment dictate that in order for the system to be implemented by any substantial number of mines, it must fulfil the above list. Since warnings of rock movements would not only save lives, but also prevent extra financial burden to mines, this project is given high priority by the South African mining industry. However, in order to develop a means of structurally monitoring tunnels, an understanding of tunnel conditions, and the costs involved, is vital.

2.1 Tunnel conditions

The underground environment is by all standards a harsh environment, with the result that there are two aspects that need to be considered when examining tunnel conditions:
1) The most obvious is that of tunnel structure, and the support systems that create stable tunnels;
2) Equally important from an instrumentation point of view: the environmental conditions that any sensor, electronics or processing equipment must be robust enough to withstand. This includes the fact that miners with no special training would install the SHM system.

Typical "atmospheric" conditions for South African underground excavations are summarised in the table below:

Table 2.1: Summary of environmental conditions within South African mines [81,83,84]

Parameter	Typical values and ranges
Humidity	Generally humidity approaches 100% underground, a difficult condition for human workers, but even more so for electronic equipment which must be properly sealed
Air velocity	All ventilation and cooling is supplied from above the ground, and air velocity ranges from 0m/s to 10m/s.
Air temperature	Air temperature may range from 18^0C to over 35^0C depending on one's relative position to the nearest air-conditioning duct.
Rock temperature	Rock temperature increases with depth (as expected) varying from 19^0C at a depth of 570m (Rustenberg platinum mine) to 41^0C at a depth of 3350m (Kloof gold mine).
Noise levels	Noise levels result from machinery operation (jackhammers etc), blasting, and also naturally from rock slipping. Most vibration occurs between 4 and 900Hz, and noise levels go up to 130dB.
Dust levels	Dust is a factor easily overlooked but blasting creates clouds of it periodically. Since this dust doesn't have anywhere to escape to, it settles on surfaces – another factor to consider in sensor selection. Typically dust concentrations of more than 2 mg/m^3 (for prolonged periods) are considered unacceptable.

The data presented in the table above, indicate several possible hazards for any sensor to be placed underground. Humidity is of concern from the perspective of possible rusting of components. Significant levels of corrosive agents are also present in some rock types, meaning that any exposed sensor components should be constructed from alloys with good corrosion resistance (such as stainless steel or aluminium) or from inert substances such as plastics or fibre reinforced plastics. Any electronics employed would also have to be exceptionally well sealed against moisture and dust, and should definitely not be temperature sensitive. The actual data acquisition should be insensitive to noise and vibration and whatever natural ferromagnetism is present in the rock mass.

From a structural perspective, the creation of a mining tunnel has associated with it an initial blasting operation, as well as possible further blasts for tunnel enlargement. By their very nature these blasts cause the rock mass to fracture, and while a stable-looking tunnel is left in the wake of tunnelling operations the condition of the rock mass is actually anything but stable. The degree of fracturing of the rock mass forming side-walls and roof walls, is a function not only of the depth at which mining takes place (South African deep mines behave significantly differently to shallow mines found elsewhere in the world) but also the type of ground or rock that is being tunnelled. In addition, these tunnels are often subjected to seismic events of varying proportions [85,86,87,88]. The ability of support systems to absorb *kinetic* energy becomes important during rock-bursts, which may cause rock to be accelerated to velocities of more than 3m/s. Under "static" conditions tunnel support does work in the order or 4-6 kJ per square metre. However, during a rock-burst this same system may be required to absorb up to 25kJ of seismic energy per square metre [89].

Most tunnels in South African gold mines are "square" in shape, three by three metres. At depths greater than 2000m the creation of these tunnels commonly has associated with it an elliptical envelope of fractured rock as seen in the figure below.
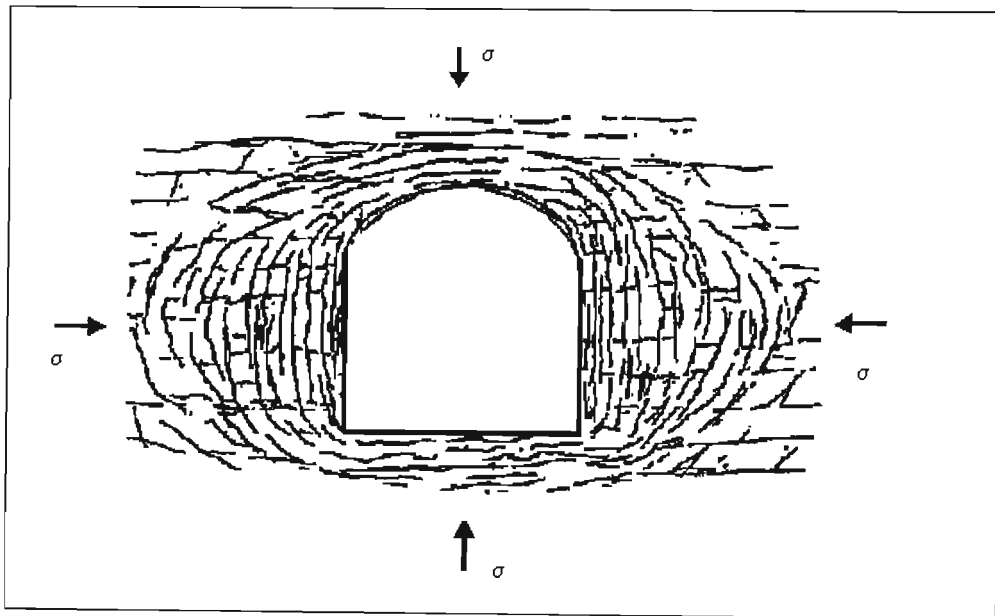
Figure 2. 1: Stresses and fractured rock region commonly associated with tunnel blasting

In the figure shown above, the maximum principle stress occurs in the vertical direction or parallel to the minor axis of the ellipse, and the minimum principle stress occurs in the horizontal direction or parallel to the major axis of the ellipse. It is also noticeable that rock

splitting occurs parallel to the maximum principle compressive stress. Slabbing therefore occurs preferentially in the sidewalls, with the sizes of the slabs being dependent on the rock type, and stress level.

Support is then added to create a stable tunnel as shown in the Figure 2.2 below. There are two basic ways of creating stability within the tunnel. Either one creates a zone of supported rock fragments which form a stable arch-like structure, (Figure 2.2(a)) or if it is possible, long tendons may be used to anchor the fractured rock to stable (non-fragmented) rock above as shown in Figure 2.2 (b) below.
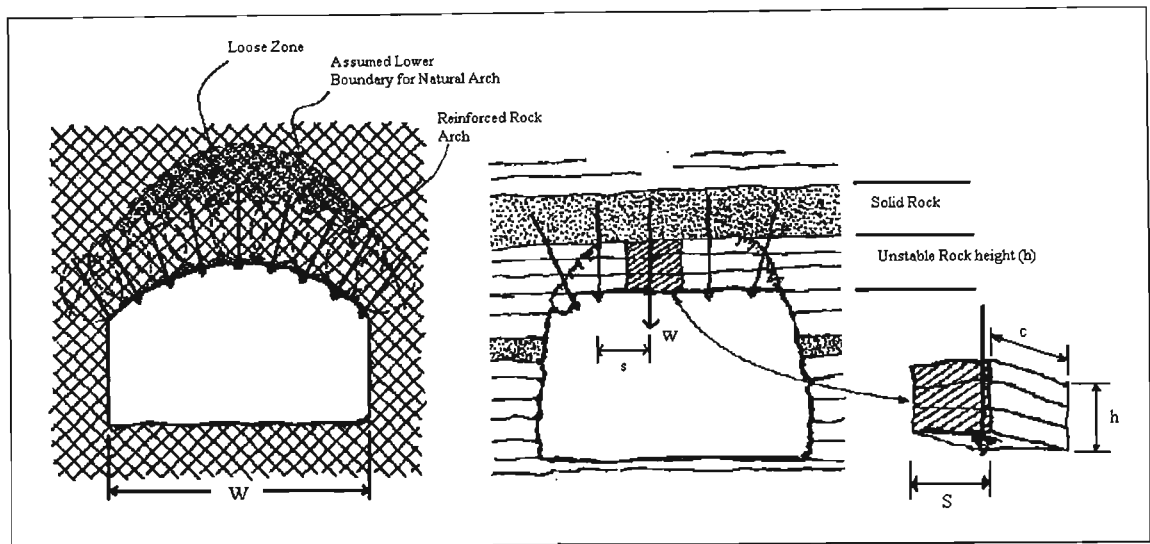
Figure 2. 2: **Methods of reinforcing a tunnel**

(a) An arch of compressed rock fragments is created to support the further fractured zone above it.

(b) The fractured rock is anchored to solid rock above it.

2.2 Support systems currently available

The quality of the support within the tunnel effectively determines the stability, lifespan and safety of the tunnel. Factors such as the depth at which the tunnel is to be constructed, the type of rock present, the presence of faults, dykes or other geological phenomenon, and the shape of the tunnel all have an influence on the type of support structures which should be used. Added to the above is the fact that there is an interaction between the supports and the rock mass, which influences the type of loading set up in tunnel walls. One type or a combination of support mechanisms may be used to achieve stable tunnels. Figure 2.3 below shows a typical arrangement of support systems used together. Of these, however, only the tendons hold promise for the creation of a smart component capable of accurate measurement of stresses in

the rock mass. Because there are many types of tendons available and currently in use, these will be examined in some depth, before the design of a smart mining bolt is attempted.
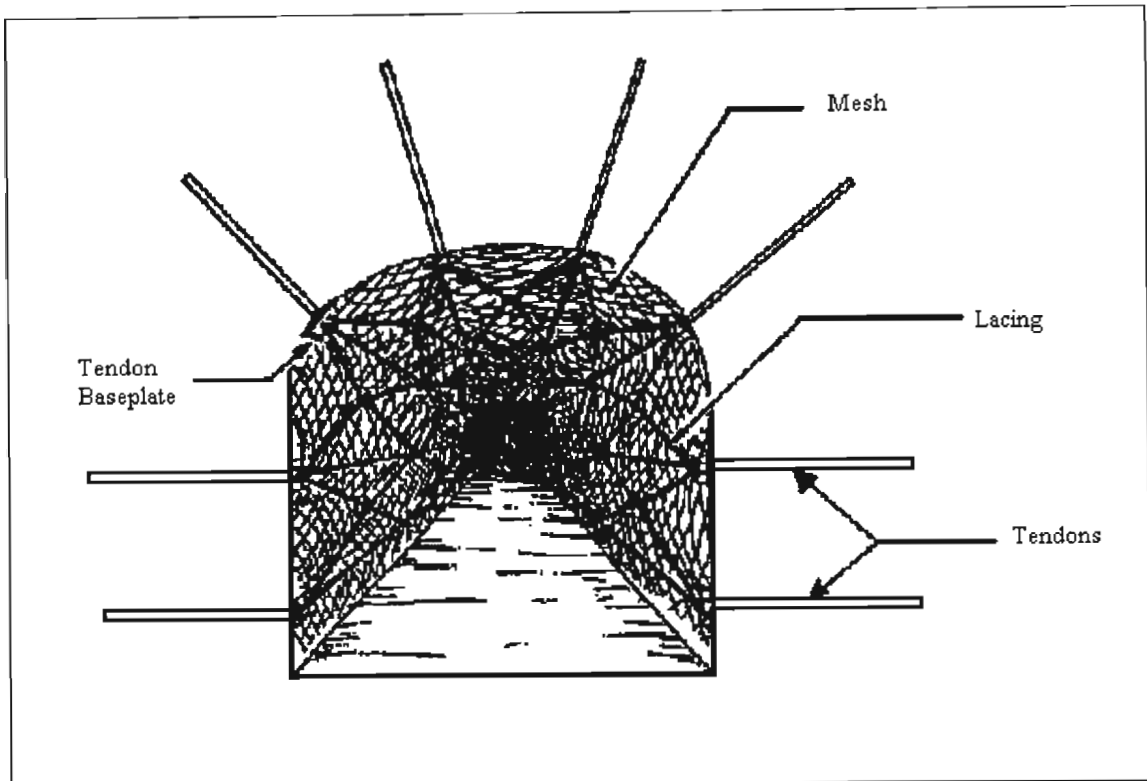
Figure 2. 3: Illustration of all major tunnel support systems

In the broadest sense, tendons are reinforcing elements, which may be of bar form, cable or tube form, that are inserted into the tunnel walls by means of a borehole, and are then anchored either by grouting or frictional means. There are many different types of tendons available on the market, but they can be categorised into three basic groups as discussed below.

2.2.1 Continuous mechanical coupled elements

These, as the name suggests, are coupled to the rock mass along the entire length of the element. This is usually achieved by grouting, either with a substance resembling cement, or a set of resin cartridges which when mixed, will harden to form an effective bond. Tendons of this nature are seldom of smooth surface finish, and usually possess "irregularity" in cross-section to enhance the bonding between grout and tendon. The load is therefore transferred from the rock to the tendon via the grout. Some examples of common CMC anchors are shown in Table 2.2 below, along with a schematic that details the principle of operation.

Table 2.2: Continuously mechanically coupled rock anchors
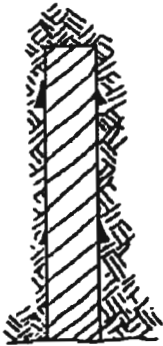
Type	Diagram	Examples
Continuous Mechanical Coupled (CMC) All fully grouted bars and cables including: -Full column grouted smooth and ripple bar in straight and shepherd's crook configurations, diameters between 16 and 20mm, lengths between 1.5 and 3m. -post-grouted, smooth bar rock studs (end anchored), diameters 16 to 20mm and lengths 1.5 to 3m. -full column grouted (smooth or ripple) bar type lacing bolts (with forged lacing eye), diameters 16 to 20mm and lengths 1.5 to 3m. -end anchored, post grouted cable tendons, 4 to 6m long.	[79]	[89] Shepherd's Crook [89] Threaded and smooth rock anchors [89] Yielding Groutable Stud

2.2.2 Continuous friction coupled elements

This type of tendon uses friction to create the interface between bolt and rock. The example shown in Table 2.3 below, is manufactured by Steeledale, and consists of a long length of open seam tube, onto which is welded a steel ring that retains a bearing plate. This type of anchor is inserted by drilling a hole slightly smaller in diameter than the unrestrained anchor, and then driving the anchor into the bored rock hole, by means of a jackhammer, or equivalent tool [89]. Although these bolts are quick to install and stand up to the blast vibrations fairly well, they suffer some critical limitations. The initial friction lock strength per metre of embedded length in competent rock is actually very low, meaning that effective support of wedges, blocks and

slabs in fractured rock (around tunnel edges) cannot be guaranteed. Furthermore, the diameter of the drilled borehole is required to fit fairly tight tolerances with respect to bolt diameter – slight inaccuracy in borehole drilling could substantially lower the frictional forces between the bolt and the rock face [80]. Recently, various advances in design [90] have produced a more efficient CFC bolt that can be pre-tensioned.
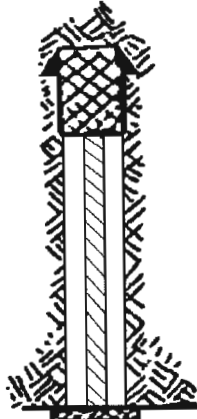
Table 2.3: Continuously friction coupled rock anchors

Type	Diagram	Example
Continuous Friction Coupled (CFC) Split sets and Swellex bolts	 [79]	 [89] Friction rock anchors

2.2.3 Discrete mechanical and friction coupled elements

These are usually only coupled at their ends either by grouting (mechanical) or some kind of expansion shell (frictional). The expanding shell bolt shown in the table below is inserted into the borehole and then torqued to draw the expander plug down into the anchor, thereby forcing the leaves to expand in a radial fashion. The serrated or roughened leaves make contact with the rock and hold by friction. A base/bearing plate is then attached at the rock face, and as soon as bonding at the anchor end has been accomplished, the bolt is then placed in tension by tightening the nut against the bearing plate. Because the bolt is in tension, the rock is placed in compression, effectively creating a natural self-supporting arch. The fact that these bolts can be tensioned makes them an active supporting system rather than passive as the previous category (CMC) is. In particular cone anchored tendons have been found to be capable of controlling large ground movements (axial >100mm, and shear <68mm) as well as reducing damage resulting from rock-bursts [80,89].

Table 2.4: Discrete mechanical and friction coupled rock anchors

Type	Diagram	Examples
Discrete Mechanical and Friction Coupled (DMFC) Mechanical or resin end-anchored bars and cables.	 [79]	 [89] Expanding Shell bolt [89] Mbobobar

The rock anchors presented in the preceding sections are the most common ones, but do not comprise all those that are available. Different anchors are used in different circumstances, for different loading conditions, and also have different costs attached to them. Before designing a smart mining bolt, it is a worthwhile exercise to briefly examine the support systems most often chosen by tunnel engineers, as well as understand the structural reasons for which they choose these supports. The costs involved in purchasing, hauling and installing each of the bolts discussed above, also play a significant role in the decisions mine management make with regards to effective creation of stable tunnels.

2.3 Determination of support requirements.

A method of determining which supports should be used under various circumstances is vital to the engineer and should take cognisance of the following factors:

> - The strength of the intact rock
> - The quality of the rock, which is determined by coring a sample and testing
> - The joint spacing, quality and orientation

➢ The effect of the presence of ground water

➢ The orientation of discontinuities with respect to a planned tunnel

➢ The seismic risk

➢ The size and type of the planned excavation, and

➢ The in-situ stresses.

Wiseman (1979) used a Rockwall Condition Factor (RCF) to determine the extent of support required in given ground conditions.

The Rockwall Condition Factor is given by the equation:

$$RCF = (2\sigma_1 - \sigma_3)/F\sigma_c \qquad\qquad (2.1)$$

where: σ_1 and σ_3 are the maximum and minimum principle stresses (respectively) within the plane of excavation (see Fig. 2.1), σ_c is the uniaxial compressive strength for the rock mass, and F is the factor by which σ_c is downgraded. This empirical factor F depends on the excavation size and the rock mass condition. In highly discontinuous rock, F is set to 0.5, and in very large excavations (larger than 6 x 6m) F is downgraded a further 10%.

It has been found experimentally that for an RCF< 0.7 good conditions prevail with minimum support, while for 0.7 < RCF < 1.4, average conditions prevail with typical support systems, and for RCF > 1.4 poor ground condition prevailed, with the need for specialised support systems. Actual support selection and spacing of the supports is also based on the stress conditions expected in the tunnel.

Table 2.5 gives a summary of the suggested support selections based on RCF criteria. However, although the table below makes recommendations of different bolt types for different conditions, this poses a logistical nightmare for mine management, which must then buy in several different bolt types, and ensure that these are correctly distributed to the various differing ground conditions within the myriad of mining tunnels and excavations underground. For this reason, mines tend to standardise on one or two bolt/tendon types; thereby simplifying matters. It is at this point that cost is factored into the equation. For this reason a table of comparative costs of support systems is presented in Table 2.6. Although the data was collated in 1999 and an increase in the prices shown is to be expected, it is still useful from a comparative perspective.

Table 2.5: Summary of support system selection based on ground conditions [79].

Support recommendations for good ground conditions (RCF <0.7)		
Case	**Primary Support**	**Secondary Support**
Static stress conditions	Spot support where necessary – split sets, rock studs etc.	Spot support where necessary – rock studs etc.
Stress changes anticipated	Spot support where necessary – split sets, rock studs etc.	Fully grouted tendons > 1.5m in length, installed on a basic 2m pattern. Support resistance: 30-50kN/m². Rope lacing on sidewalls only.
Seismic activity anticipated	Split sets or tendons > 1.2m long, installed as close to the face as possible, on basic 2m or 1.5m pattern. Support resistance: 30 – 50kN/m².	Fully grouted (preferably yielding) tendons > 1.5m long, installed on basic 2m pattern. Support resistance: 50kN/m². Mesh and lacing on all walls
Support recommendation for average ground conditions (0.7 < RCF < 1.4)		
Case	**Primary Support**	**Secondary Support**
Static stress conditions	Rock studs or tendons > 1.5m long, installed as close to the face as possible, on basic 2m pattern. Support resistance: 30 – 50 kN/m².	Steel strapping of rope lacing integrated with primary support tendons; or shotcrete.
Stress changes anticipated	Fully grouted tendons > 1.8m long, installed as close to the face as possible, on basic 2m or 1.5m pattern. Support resistance: 40 – 60kN/m².	Rope lacing and wire mesh integrated with primary support tendons.
Seismic activity anticipated	Fully grouted (preferably yielding) tendons > 1.8m long, installed as close to the face as possible, on 1.5m or double 2m pattern. Support resistance: 80 – 110kN/m².	Rope lacing and wire mesh integrated with primary support tendons, plus optional shotcrete.
Support recommendations for poor ground conditions (RCF > 1.4)		
Case	**Primary Support**	**Secondary Support**
Static stress conditions	If necessary, shotcrete to the face, then fully grouted tendons, length >1.8m on basic 1.5m pattern as close to the face as possible. Support resistance: 80-110kN/m².	Steel wire mesh integrated with primary support: optional shotcrete.
Stress changes anticipated	If necessary, shotcrete to the face, then fully grouted tendons, length >1.8m on basic 1m or double 2m pattern, as close to the face as possible. Support resistance: 120 – 230kN/m².	Rope lacing and wire mesh integrated with primary support. Add integral shotcrete in long-life tunnels. If necessary, additional hangingwall support comprising grouted steel ropes.
Seismic activity anticipated	If necessary, shotcrete to the face, then fully grouted tendons, length > 2.3m on basic 1m pattern, as close to the face as possible. Support resistance: 220 – 290kN/m².	Rope lacing and wire mesh integrated with primary support. Add integral shotcrete in long life tunnels. If necessary, additional hangingwall support comprising grouted steel ropes.

Table 2.6: Comparative costs for various support systems in 1999 [80].

Description	Specification	Cost
Shotcrete	25mm thickness	R61 – R65 /m^2
	50mm thickness	R75 – R115 /m^2
	75mm thickness	R125 - R170 /m^2
	100mm thickness	R195 - R210 /m^2
All shotcrete calculations include a factor of 1.4 to allow for rebound off tunnel walls, however, when shotcreting over wire mesh this figure could go as high as 1.8. Also, if steel fibre (average of 40kg per m^3 sprayed) were added an additional R400/m^3 should be added to the costs above.		
Diamond mesh	75mm x 3mm	R41 - R47 /m^2
Diamond mesh and 12mm lacing	75mm x 3mm	R70 - R79 /m^2
Cable anchor, grout and tension	4m	R270 – R290 /unit
Freyssinet yield anchor, grout and tension	6m	R315 – R330 /unit
	8m	R 380 – R395 /unit
	10m	R430 –R440 /unit
Split sets	1.5m x 36mm	R44 – R52 /unit
	1.8m x 36mm	R50 – R59 /unit
Anchor bolts	1.5m x 20mm	R55 – R66 /unit
Point anchor bolt with resin capsules and post grout	1.8m x 20mm	R61 – R68 /unit
Anchor bolt and full column resin capsules	2.2m x 20mm	R 85 – R96 /unit
Gewi bars	1.5m x 20mm	R56 – R65 /unit
	1.8m x 20mm	R62 – R70 /unit
Shepherd's crook and pumped grout (ripple or smooth)	2.4m x 16mm	R37 – R43 /unit
Shepherd's crook cone bolt	2.2m x 16mm	R50 – R54 /unit
Cone bolt (straight)	2.2m x 22mm	R52 – R58 /unit

All the costs shown in table 2.6 [80] include material, labour and plant costs, since the greater cost often lies in haulage and installation of support systems rather than the actual material cost. Costs are also region specific in that variations are experienced due to transportation costs and availability being greater or lesser, dependent on mine location. It is therefore particularly important for smart bolts to be easily hauled down shafts and through tunnels, and installed with minimum fuss and extra care on the part of miners.

2.4 Implementing a structural health monitoring solution

By way of summation, the requirements for the implementation of a structural health monitoring system in South African mining tunnels, have been identified as follows:

➢ The environmental conditions dictate that all sensing equipment be corrosion resistant, and well sealed against moisture and dust. Noise and vibration levels, as well as substantial temperature variation should also be taken into account.

➢ A brief study of the tunnel support systems available and their installation dictates that any smart system should be hauled, and installed with an absolute minimum of "extra care", and should preferably withstand installation by the ordinary mine worker. Interrogation of the SHM system should not require specialised personnel, and should be available remotely due to the fact that South African tunnels are usually 3m high and physical access to sensors or sensing equipment is not always feasible.

➢ Tables 2.5 and 2.6 show that the most versatile type of bolt is a fully grouted bolt and although Shepherd's Crook bolt are the least expensive, greater support and versatility is derived from bolts that can be pre-tensioned.

It should be said that an Australian mining company has already produced an instrument that can actually determine the health of mining bolts. The instrument uses an ultrasound or dynamic frequency response type approach [91]. It is, however, not only expensive, but also requires qualified personnel to perform the interrogation. The fact that the bolts must also be physically reached by these personnel makes this an NDT approach rather than an SHM approach to the problem. The objective of this study is to produce a smart mining bolt that, once installed, will not need to be recovered, or touched in any way, but will bear the usual load of a mining bolt while at the same time produce information regarding its own state of health, which can be correlated to the stress state of the tunnel, thereby warning of rock dilation (which would eventually tend to close the tunnel up) as well as potentially hazardous large scale rock movements likely to cause catastrophic collapse.

CHAPTER 3

MINING BOLT DESIGN

The creation of a smart mining anchor or bolt seems deceptively easy. Although the concept is relatively straight forward, there is a multitude of design challenges that must be met. Among the issues requiring attention are the following:

> A cost effective material must be developed with the correct transformation characteristics for the stresses and strains experienced in mining tunnels, as well as satisfy the SABS standards. [All material development issues are addressed in the next chapter.]

> A knowledge of the loading conditions experienced by the bolt will also be required in order to ensure damage is actually detected, and enable correlation between bolt material transformation and rock movement, or tunnel health.

> Conformation to the SABS standard for mining bolts in terms of design, and strength.

> The physical design or type of bolt must be chosen, i.e. continuously mechanically coupled etc.

> And, perhaps the most important, some means of actually extracting a damage reading from an in situ bolt must be provided for, i.e. the sensing design.

The production of a prototype is unfortunately complicated by the fact that the above issues are all inter-related, as shown in the flow diagram (Figure 3.1) below. Each of these design issues will, however be examined systematically, and the final prototype presented in the sections that follow.
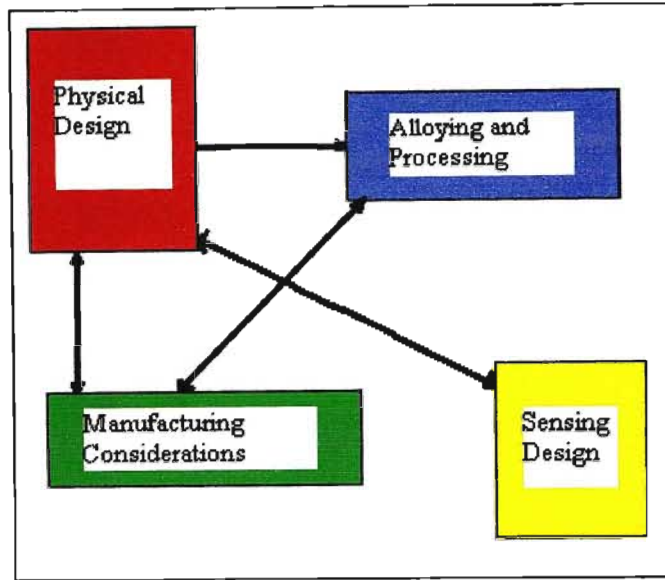
Figure 3. 1: Inter-relationship between various design aspects of the smart mining bolt

3.1 Damage detection extraction

Perhaps the most difficult of the problems to solve, a means of measuring the change in the magnetic behaviour of the material must be found and integrated into the bolt design in such a way as to minimise installation complications, and subsequent data acquisition. The method chosen must also be able to withstand the environmental conditions presented in the previous chapter in Table 2.1, and not require any power lines or data cables to be run on the tunnel surface. A broad search of the magnetic reading methods was therefore conducted [92-107].

3.1.1 Magnetism and magnetic susceptibility

Different materials behave differently in the presence of a magnetic field. In the case of strain memory alloys there is a change from paramagnetic to ferromagnetic (see glossary for definitions) behaviour. To measure this change, a magnetic field must be applied to the material. Essentially magnetic field can be defined in terms of its strength (H) and the magnetic flux density (B).

Consider a thin conductor with current (i) passing through it: a magnetic field is produced around the conductor as shown in the figure below. Field strength (H) is then expressed in vector form:

$$dH = \frac{idl \times r}{4\pi r^3} \qquad \oint H dl = i \qquad \text{OR} \quad \nabla \times H = S \qquad (3.1)$$

where S is the current density measured in A/cm^2.
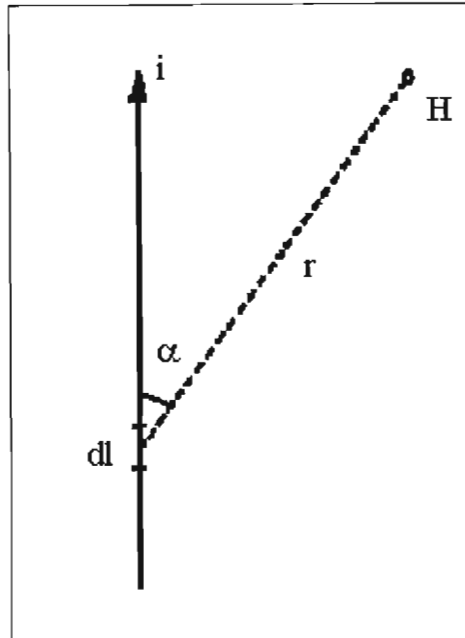
Figure 3. 2: Definition of magnetic field strength H [108]

Flux density B (measured in Tesla or Gauss) may be explained by considering a coil coupled with a magnetic field that is changing with time – a voltage develops at the terminals of the coil, yielding the relationship:

Voltage $v = -\dfrac{d\phi}{dt}$ OR $v = -N\dfrac{d\phi}{dt}$ for N windings, where $\phi = \oint_A BdA$.   (3.2)

Methods of measuring "magnetism" can therefore either measure field strength H or the flux density B. Shown below is a list of some of the methods used to quantify magnetic effects, classified according to their measurement principle [84].
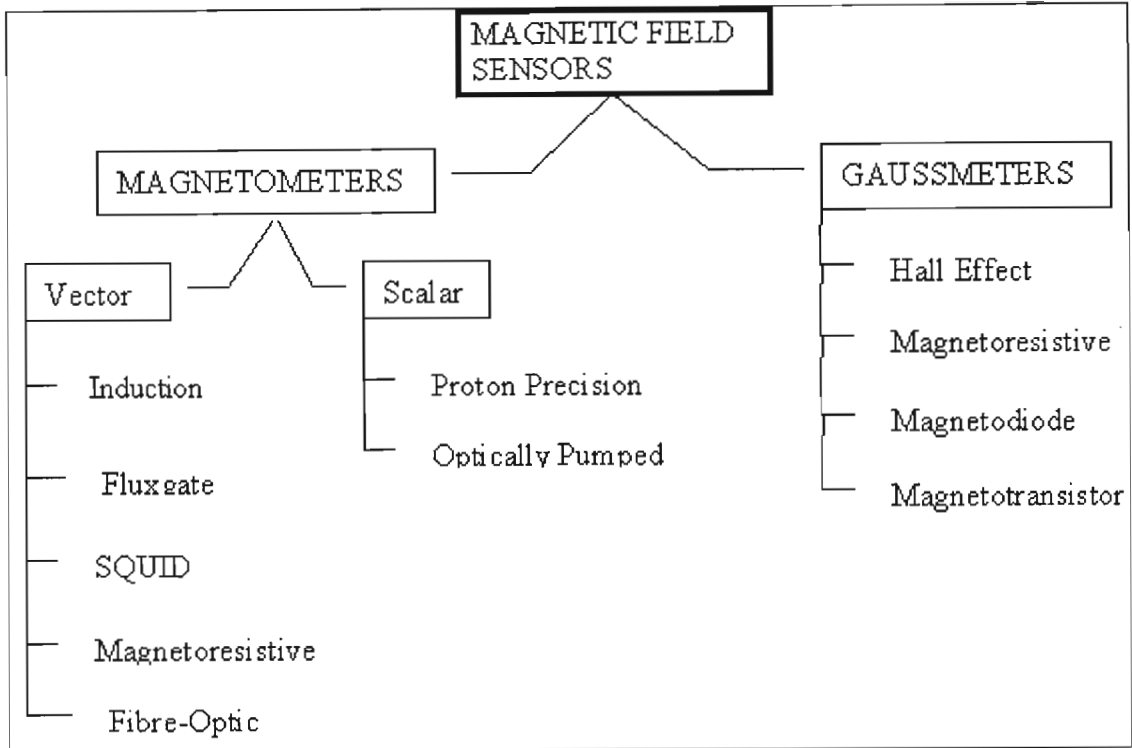
Figure 3. 3: Magnetic field sensors

The above are merely some of the methods of measuring magnetism. Not all of these are however practical from a physical, economic or sensitivity perspective. For this reason, focus was directed to only four methods identified to hold the most promise for smart components.

3.1.2 SQUID

A Superconducting QUantum Interference Device (SQUID) is an extremely sensitive device known to measure magnetic fields of the order of 10^{-14}T. The essential components of the device are two parallel Josephson junctions, formed by two superconductors separated by a thin insulating film. The current in the SQUID device oscillates with changes in phase at the two Josephson junctions, dependent on the change in magnetic flux. By counting the oscillations, the magnetic flux changes may be calculated. The result then is that the SQUID functions as a flux to voltage converter of extremely sensitive proportions. A schematic of a simple SQUID device is shown in Figure 3.4 below.

31
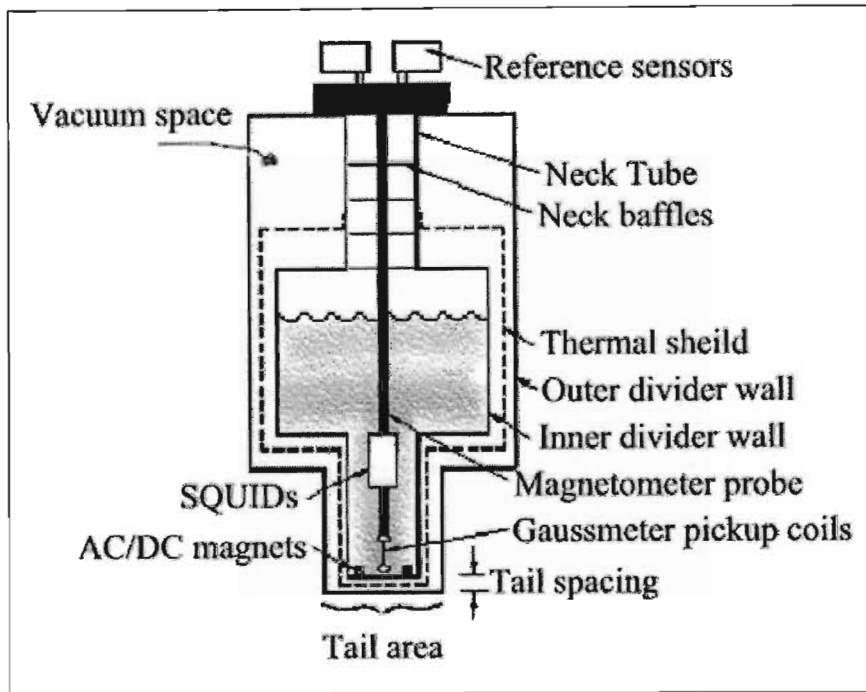
Figure 3. 4: Construction details of a typical SQUID device [236]

Typically, the squid device must be located inside a small cylindrical superconducting magnetic shield in the middle of a liquid helium jacket, as shown in the figure above. Located at the bottom of the liquid helium jacket are the superconducting pick-up coils, which detect the difference in one component of the field between two points. The subject of interest is then placed beneath the magnetometer underneath what is marked as the tail area in the figure above. Almost all of the rest of the construction is concerned with minimizing the helium boil-off, eliminating background radiation interference and any external ac field interference.

As a sensing device, the SQUID has very few competitors for sensitivity, but it does suffer a number of disadvantages. The first of these is the lack of ruggedness of the instrument – it will definitely not survive the mining environment, but may find application in other applications where conditions are more stable, sanitized and conducive to accommodating the rather bulky cooling system required for superconductive components. The last disadvantage lies in the cost (which is substantial when compared to other measuring techniques) associated with this instrument.

3.1.3 Inductive methods

The concept of inductance may be simply illustrated by considering a toroidal coil connected to an AC source. As the alternating current passes through the coil, an alternating magnetic field is

set up, in turn producing a voltage. The relationship between these quantities may be expressed as:

Voltage $v = -L\dfrac{di}{dt}$ (3.3)

Where i is current (Amps)

t is time (secs) and

L is inductance (Henry)

This therefore implies that $L = \dfrac{d\phi}{di}$, and if the coil has N windings $L = N\dfrac{d\phi}{di}$. (3.4)

One can then add a constant C_1 related to the dimensions of the core of the coil, and the field configuration, and the equation above becomes:

$L = \dfrac{N^2}{C_1} \times \dfrac{B}{H}$ where $\dfrac{B}{H}$ is the permeability of the core. (3.5)

Paramagnetic core materials have permeabilities higher or equal to a vacuum ($4\pi \times 10^{-7}$ H/m) while ferromagnetic materials have permeabilities far, far greater than this. Thus the above principle could be applied to structural health monitoring systems in the following manner:

1) A coil could be wrapped around a rod made of strain memory alloy and connected to an inductance meter. As the core material transforms from austenite (paramagnetic) to martensite (ferromagnetic), the permeability therefore changes, and the inductance therefore also changes according to eqn. (3.5), giving a readily available transformation indication.

2) If a probe is required, rather than an external coil, the same theory may be applied in the form of pancake coils. [238] The relevant circuitry is illustrated below in Figure 3.5, and consists of an oscillator, an LC circuit and a voltmeter. The LC circuit is characterised by an oscillating current/charge, with an angular frequency of $\omega_o = \sqrt{\dfrac{1}{LC}}$. The circuit is driven by an oscillator, which is set to oscillate at the natural frequency of the LC circuit. As the material is brought into contact with the pancake coil probe, the change in permeability results in a change in inductance (again according to eqn. 3.5), and therefore a change in the natural frequency of the LC circuit. This change is measured as a voltage V_s.
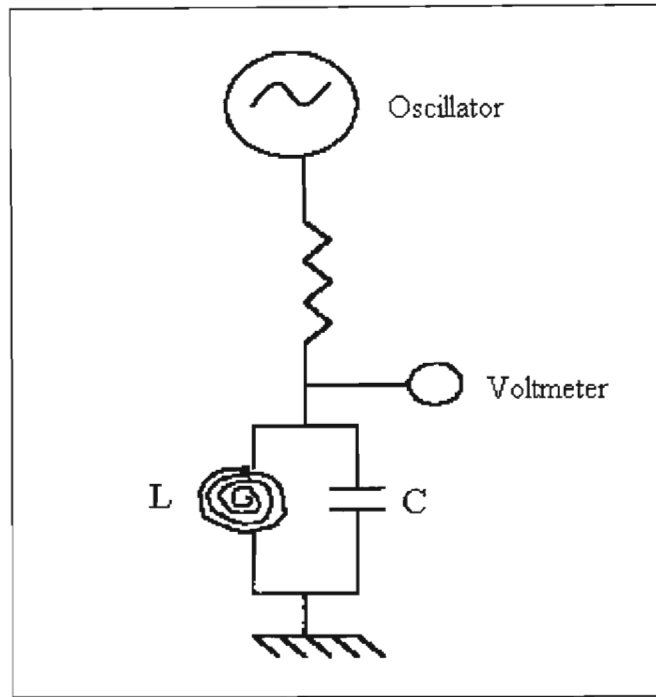
Figure 3. 5: The components of a pancake coil induction probe [109]

Thus as a prospective measurement technique, the use of a coil with changing inductance dependent on magnetic permeability changes, is a neat technique that may be easily adapted to a variety of geometries and situations. The low cost involved in producing electronic circuitry, which uses this technique, as well as the opportunity to produce a rugged system, are particularly attractive features.

3.1.4 Fluxgate Magnetometer

Physically small, the fluxgate magnetometer is capable of measuring magnetic fields in the order of the 0.1nT to 1mT range. Its rugged, reliable nature, as well as the fact that it requires little power to operate, makes it an attractive option as a measurement instrument. The actual operation of the fluxgate magnetometer relies on an alternating saturation of magnetic material. To further explain the functioning of the fluxgate, consider the very simplified diagram shown below.
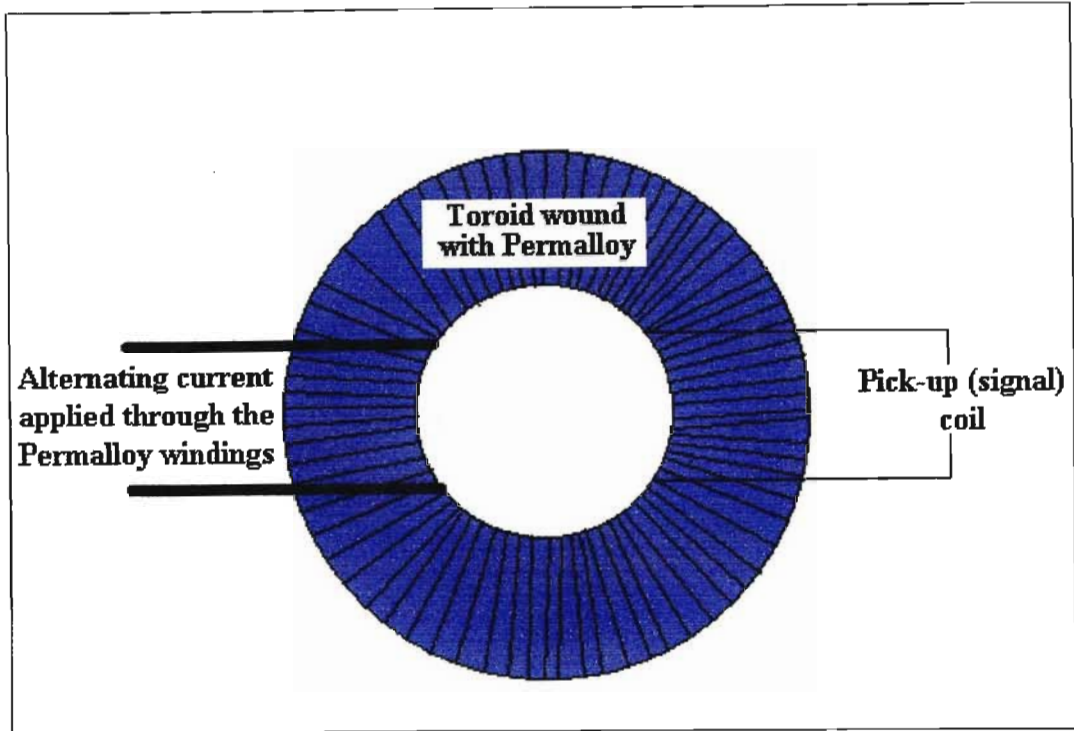
Figure 3. 6: The operation principle of a fluxgate magnetometer [84]

A ring core fluxgate (as shown above) is constructed from a bobbin, wound with easily saturable ferromagnetic material such as Permalloy to form a toroid. An alternating current is then applied through a coil, which is wound around the toroid, thereby creating a magnetic field that circulates around the magnetic core. This magnetic field causes the flux in the ferrous material to saturate periodically clockwise and then counterclockwise. Another winding is wrapped around the outside of the toroid to form a pick-up coil. While the ferrous material is between saturation extremes, it maintains an average permeability much greater than that of air, but when the core is in saturation, the core permeability becomes equal to that of air. If there is no component of magnetic field along the axis of the signal winding then the flux change seen by the winding is zero. However, if there is a magnetic field component present, then each time the ferrous material goes from one saturation extreme to another, the flux within the core will change from a low level to a high level. According to Faraday's law, a changing flux will produce a voltage at the terminals of the signal winding that is proportional to the rate of change of flux.

For dc and low-frequency magnetic fields, the signal winding voltage is:

$$e(t) = nA \frac{d(\mu_0 \mu_e H)}{dt} = nA\mu_0 H \frac{d\mu_0(t)}{dt} \qquad (3.6)$$

Where H   = Component of the magnetic field being measured

    n   = Number of turns on the signal winding

    A   = Cross-sectional area of the signal winding

    μ_e (t)   = Effective relative permeability of the core

    μ_o = Constant given by: H= μ_o B

As the core permeability alternates from a low value to a high value, it produces a voltage pulse at the signal winding output that has amplitude proportional to the magnitude of the external magnetic field and a phase indicating the direction of the field. The frequency of the signal is twice the excitation frequency since the saturation-to-saturation transition occurs twice each excitation period.

3.1.5 The Hall effect

The Hall Effect sensor is a useful device for measuring the flux density of a sample and can be used in a variety of applications. The beauty of the Hall effect sensor is that it is available in probe form, and presents a simple off-the-shelf solution. It is, however, direction sensitive, meaning that the orientation of the probe with respect to the magnetic field is a very important variable.

The Hall effect may be explained by considering a particle, with charge Q, velocity **V** and moving within a magnetic field **B**. The particle will experience a force called the *Lorentz force*, given by:

$$F = Q (\mathbf{V} \mathbf{x} \mathbf{B}).$$ (3.7)
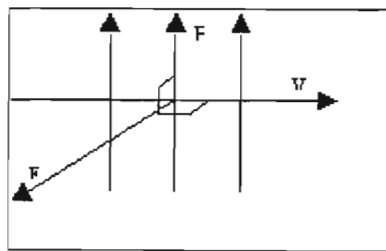
Figure 3. 7: Illustration of Lorentz force direction

The direction of the force F is mutually perpendicular to the directions of the particle velocity and the magnetic field (B) as shown in Figure 3.7 above. If a long, flat, current-carrying conductor is placed in a magnetic field; the moving charges will experience a net force mutually

perpendicular to the direction of the current flow and magnetic field. The electrons will accumulate on one edge of the plate, due to the Lorentz force, with positive charges gathering on the opposite edge. This uneven lateral charge distribution results in an electric field, **E**, which exerts a force, given by:

$$\mathbf{F} = \mathbf{QE} \tag{3.8}$$

This force is opposite in direction to the Lorentz force. The field, superimposed on the electric field in the direction of the current flow, yields skewed equipotential lines and hence the Hall voltage.

The relation between the Hall voltage, current and the magnetic field can be given as:

$$V_H = K_{HOC}\, I_c\, B\, \sin(\acute{e}) \tag{3.9}$$

Where: V_H = Hall Output Voltage (mV)

K_{HOC} = Open Circuit Product Sensitivity Constant (mV/mA kG)

I_c = Control Current (mA)

B = Magnetic Flux Density (kG)

$\acute{e}$ = angle of magnetic flux
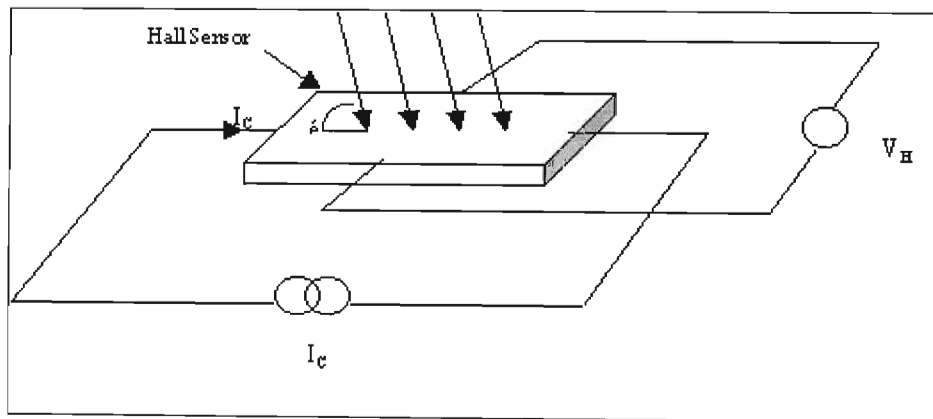
Figure 3. 8: Illustration of a Hall sensor

It is obvious from eqn. 3.9 that the angle of flux is vitally important: as the angle decreases, the reading decreases until it reaches zero when the angle is zero.
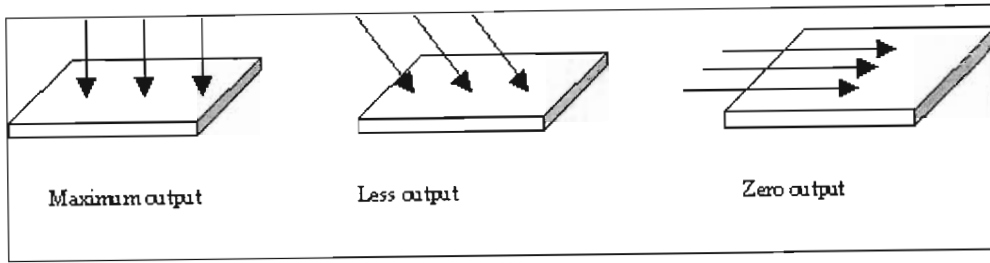
Figure 3. 9: Illustration of the angle of field versus Hall output

The two basic types of Hall sensor are transverse and axial, as can be seen in Figure 3.10. The transverse type is useful where the field must be measured in thin gaps. The axial type must be used where the field is parallel to the axis of a hole, such as in solenoids.
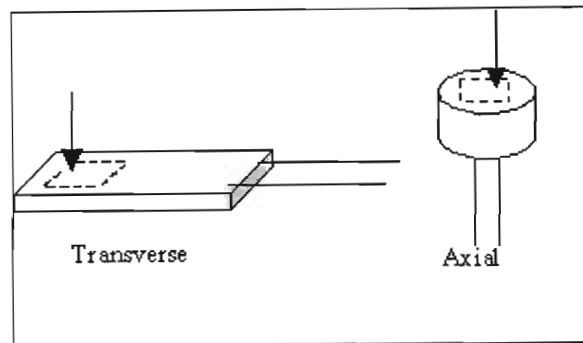
Figure 3. 10: Basic types of Hall sensor

Hall sensors can be used in various ways, depending on the application. By holding I_C constant, V_H becomes a direct function of B. If B and I_C are held constant, V_H becomes a function of the angle of B.

The Hall effect depends on the bulk-material properties of the semi-conductor material from which it is made. Some of the semi-conductor materials used are indium antimonide (InSb), indium arsenide (InAs) and gallium arsenide (GaAs). To obtain a high output voltage, the active element must have a high Hall coefficient K_{HOC}. Also, since the output is directly proportional to the current in the element, the resistance must be as low as possible to prevent excessive heating, since the error is largely a function of temperature. The sensor sensitivity is also inversely proportional to the thickness of the Hall plate i.e. the thinner the plate, the higher the sensitivity. The thickness is determined by the method of manufacture. Bulk devices are slices of ingot material that are lapped and polished. Thinner plates may be created using varying deposition methods.

Ideally, Hall sensors produce zero output voltage when not placed in a magnetic field but most produce a small voltage called the Hall Offset voltage, V_m, which can be cancelled using electronics. The Hall Offset voltage is also affected by temperature. The ideal Hall sensor is also linear but this usually not the case. Typical accuracy ranges from $\pm0.1\%$ to $\pm2\%$ of reading. The sensitivity is also temperature dependent. Hall devices are also irreversible, since the Hall sensor generates different voltages of opposite polarity for equal fields of opposite polarity. This is due to manufacturing error and can be as high as 1%.

Hall devices are generally considered as having a maximum resolution of 1 mG i.e. 1 flux line per 1000 cm^2. Below this, electrical noise and temperature effects destroy the usable signal.

3.1.6 Summary

The above techniques need to be weighed against one another, in terms of sensitivity, cost, ruggedness and general suitability to the mining environment, but most importantly, one needs to consider how the measurement technique can be integrated into a mining bolt so as to produce a fully functioning unit that does not require mining personnel to physically reach the bolt (which would usually be situated beyond their physical reach) in order to interrogate its structural health. In the table below, is a comparison between the methods described previously.

It becomes quite obvious that using some form of inductance measurement is the most likely solution for this application. This may be accomplished in one of two ways, either by the use of a pancake coil probe which must be brought into close enough proximity to the bolt to take a reading, or by winding a permanent coil around a section of the bolt or the whole bolt, from which will be taken an inductance reading. The final solution to this design problem is presented in a following section.

Table 3.1 Comparison of the various off-the-shelf methods available for measurement of magnetic field

Measurement technique	Sensitivity	Ruggedness	Cost	Suitability
Inductance	The sensitivity of this method can essentially be adjusted and tuned to suit a broad range of requirements	The inductance technique probably holds the greatest potential for adaptation to the mining environment	Probably one of the cheapest methods available	Certainly the most suitable
SQUID	Exceptionally sensitive	Not at all rugged	Too high for this application	Not suitable at all
Fluxgate	Very good	Acceptable	Not as cheap as the inductance technique, but possibly acceptable	OK
Hall Effect	Acceptable but the directional sensitivity issue introduces design complications	Acceptable	Acceptable	Not as suitable as the inductance technique

3.2 Loading conditions generally experienced by rock anchors.

Before it is possible to even begin to integrate sensing capability into a bolt, it is necessary to understand the loading to which the bolt will be subjected. As most mines will standardise their mining bolt buying and installation requirements by choosing one or two types of bolts, it seemed most logical to begin smart bolt development with one of the most common types of bolts. For this reason a continuously grouted tendon was chosen.

Primarily, one can divide the continuously grouted or CMC tendons into two categories, those that are pre-tensioned, and those that are not. Shepherd's Crook tendons are for example not pre-tensioned; and therefore often experience problems with bad installation, as a lack of proper grouting will not necessarily be noticed. Pre-tensioned tendons, however, require that the grouting hold properly in order for pre-tensioning to take place, thereby reducing this hazard substantially. The decision to produce a pre-tensionable bolt was simple since this presented a very convenient method of eliminating the incubation strain (refer to Figure 1.6).

A CMC tendon experiences predominately two modes of loading: the first of which is a simple axial tensile loading caused by rock dilation, and is applied directly to the shank of the grouted bolt. The second, is more difficult to quantify, and consists of a combination of shear and axial loading which is transferred via the grouting to the tendon, from the rock mass. This may be caused either by rock fragments sliding relative to one another, or by a crack opening between two rock fragments. The figure shown below (Figure 3.11) depicts how the load may be transferred from the rock mass to the grouting, to the rock tendon. The fact that the discontinuity is not perpendicular to the bolt aids the transfer of load to the bolt, using the axial strength of the bolt rather than just the pure shear strength. It is for this reason that mining bolts are not installed perpendicular to the known direction of slabbing.
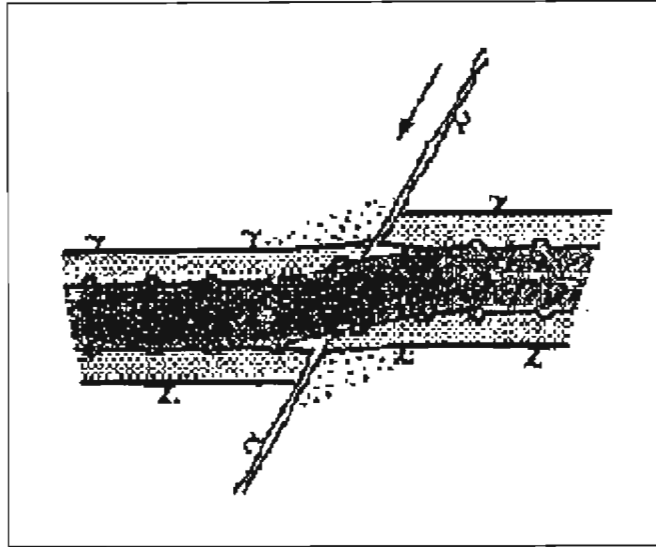
Figure 3. 11: Mechanics of load transfer from rock to bolt via grout

Figure 3.12 shows the test results from a test wherein the bolt was instrumented at various points along its axial length, and the load created by a major discontinuity subjected to shearing action, measured.
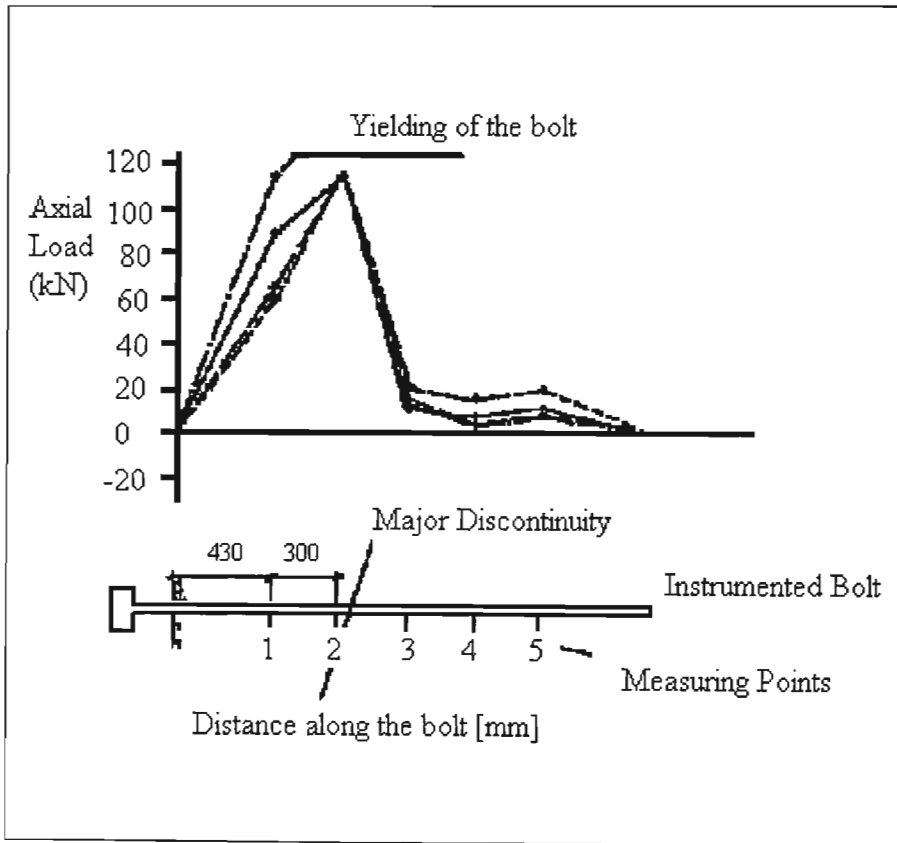
Figure 3. 12: Variation of axial load along bolt length as created by a major discontinuity

It is noticeable that the axial stress increases sharply from the nut/exposed end, peaks just before the discontinuity and then subsides rapidly to nothing at the concealed end, suggesting that the section of the bolt closest to the bearing plate does most of the work in restraining rock movement. Unfortunately the shear stresses were not measured in the test detailed above because they are more difficult to quantify [79].

The load/deformation characteristics of grouted tendons have been the subject of much research within the mining community. Factors found to influence these load-deformation characteristics are:

> Bolt diameter

> Borehole diameter

> Material properties such as ultimate and yield strengths, and stiffness.

> The nature and strength of the bar to grout bond

> Bolt inclination (with respect to discontinuity – inclined bolted joints are stiffer than perpendicular ones)

There are various cross-sectional profiles of fully groutable bar available. The most common of which are shown below in Table 3.2.

Table 3.2: Various bolt profiles available for CMC anchors

Smooth Bar	V-bar
Re-bar	Twisted or Spiral Bar

Of these, re-bar has been shown to have superior characteristics in terms of tensile, static and dynamic shear strength [80]. Their stiff nature would suggest that they are best suited to conditions where moderate rock movement is anticipated. As tendons they have been shown to sustain joint opening of between 20 and 30mm before failure. The shear loading characteristics

of such tendons are particularly impressive ranging from 0.8 to 1.0 times their tensile strength. This figure is dependent on rock strength as well though.

3.3 Mining bolt standards

The relevant SABS (South African Bureau of Standards) standard for mining bolt is SABS 1408. The rock bolts may be smooth or nibbed but are required to meet the criteria presented in Table 3.3 below:

Table 3.3: Properties of bolts required by SABS standard

Properties	Values
Minimum ultimate tensile strength	570 MPa
0,2% proof yield strength	360 MPa
Minimum elongation after fracture	22 %

Noting that the elongation after fracture shall be determined on a gauge length L_0 of the equivalent cross-sectional area, which may be calculated as follows:

$$\frac{K}{0,00785L} = \text{Equivalent cross-sectional area (m}^2)$$ where K is the mass of the bar (kg) and L is the length of the bar (>0,5m) in metres, and a density of 7850kg/m^3 for steel is used. L_0 may then be calculated as follows:

$$L_o = 5.65\sqrt{A}$$ where A is the equivalent cross-sectional area.

In addition a Charpy V-notch (impact resistance) of at least 30J is required at temperatures of 20°C and 0°C [110] a formal testing procedure for strength and ductility testing is also given in this standard.

Additional requirements are given for bearing plates, nuts, washers, etc. but since these will be bought off the shelf (and are not under development) they are of little interest for the purposes of the report.

3.4 Prototype design

Based on the extensive testing that has already been performed on products and profiles currently available on the South African market, the design shown below was adopted. Figure 3.13 illustrates the basic principle of operation for the smart mining bolt. Detailed assembly drawings are however attached in Appendix A.
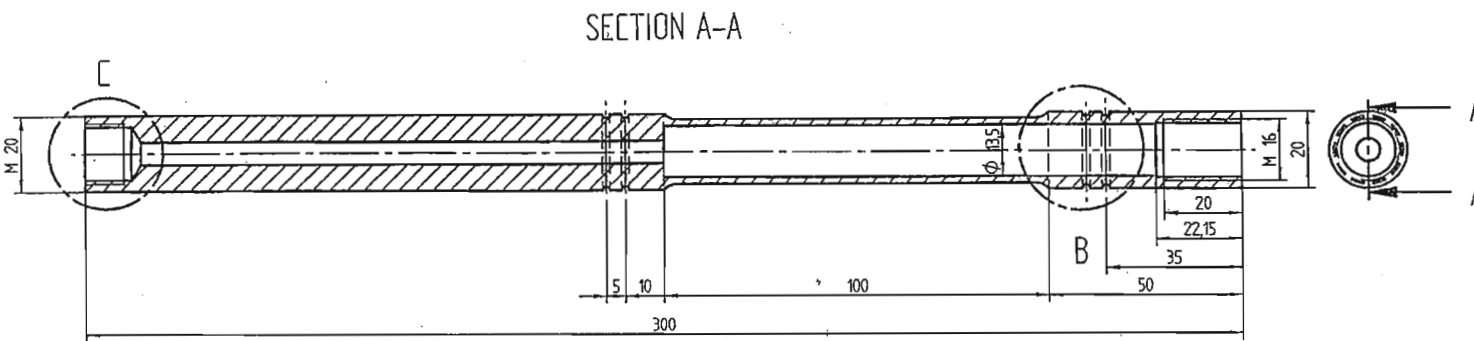
SECTION A-A

Figure 3. 13: Schematic diagram of the operating principle of the smart mining bolt

Fundamentally the bolt consists of two sections: an ordinary re-bar type section and a smooth sensor section, which is necked down to take a coil wound around this length, as well as to provide a section which will be the first to yield. In other words this forms a damage concentrator. This design was perpetuated based on the evidence presented in Figure 3.12, which shows that a discontinuity will cause far higher stresses in the base-plate end of the bolt than in the deeply buried end.

The coil, which is found from very fine copper wire, is protected by a coat of resin, then shrink-wrap and is then encased in a section of aluminium tubing that is crimped on. This effectively protects the delicate part of the bolt during transportation, handling within the mine, and subsequent installation operations. The ends of the coil wire are then fed back to a connector plug, which is seated inside the hollow cavity out of harm's way. It is onto this plug that the

45

electronics (which mimic an off-the-shelf inductance meter) will be plugged once installation is complete, and the mining bolt will see no further tampering. A check as to whether the coil is intact, will be the connection of the sensor read-out section, provided that there is no open circuit (caused by coil breakage) there should be a nominal reading displayed.

The re-bar and sensor sections were originally to be friction welded together, but in the interests of flexibility this idea was abandoned, and a threaded coupling adopted. This was because some sections of mines have limited access to the rock face, such as is the case in Platinum mines where the maximum stope-face is only 90cm, but the length of the required support tendon is longer than this. The re-bar section of the bolt will be grouted and the sensor section then attached. Effective pre-tensioning can then be checked on the digital read-out, because the tensioning effectively takes the bolt to the point of "transformation start". Any further tension or loading applied will cause a transformation in the sensor section and a change in the base reading will then be displayed on the instrument face. A conceptual schematic is shown below, along with a diagram of the visible instrument face of the bolt. The operating principle is as follows:

> The operator holds a single "box" containing a transmitter, which activates a one-way radio link with the receiver situated in the bolt's measuring instrument circuit.
> The sensor is then switched on, and takes a reading using the circuit that mimics an inductance meter, which operates at 1kHz and measures inductance.
> The LED display (marked status box in Figure 3.14) is then lit for approximately 10 seconds, after which the instrument switches off until reactivated by the operator.
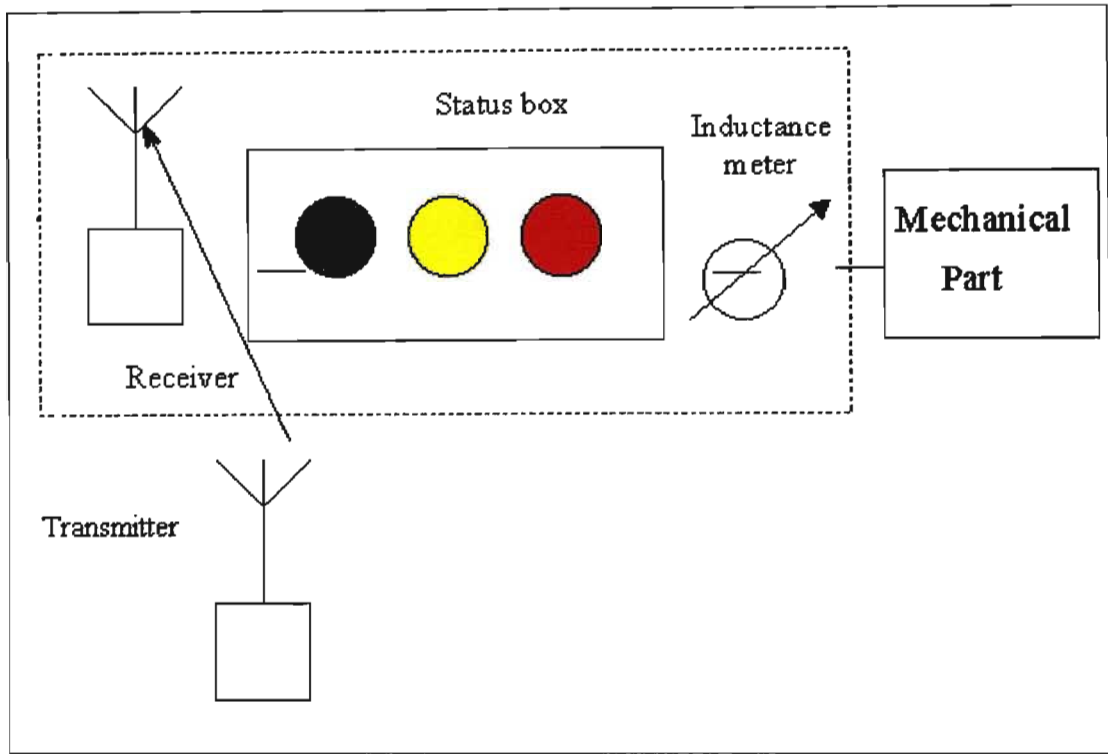
Figure 3. 14: The conceptual schematic of the sensor section of the smart mining bolt
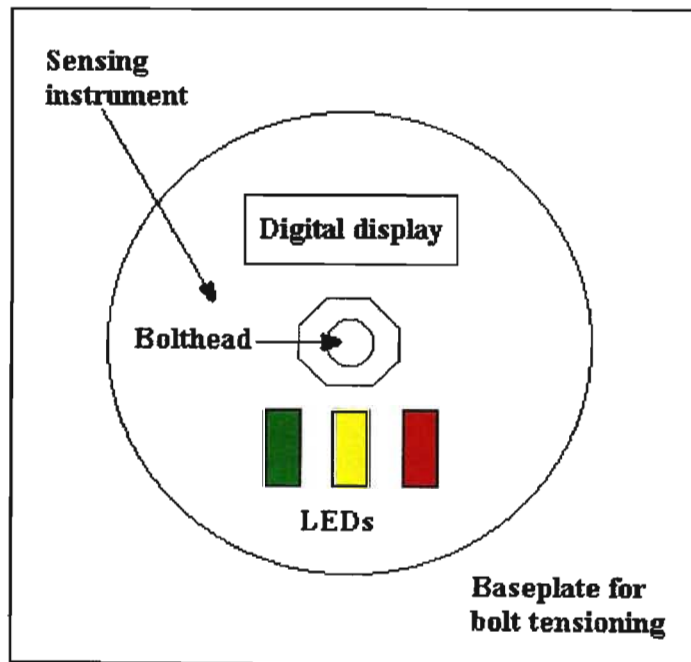
Figure 3. 15: The actual visible end of the bolt

There are two sections to the digital display shown above, the first is a digital read-out, which may be configured to give a numerical output, that is, a voltage directly proportional to the amount of strain registered in the sensor section. The second is an LED display section, which merely has three lights, green, yellow, and red, indicating safe, caution, and danger levels, obviously pre-determined by acceptable levels of rock movement correlated to levels of strain seen in the sensor section of the bolt.

It is envisaged that smart mining bolts be installed at regular intervals in a pre-determined pattern along the tunnel length, in such as way that a comprehensive picture of tunnel stresses and rock movements can be constructed from the data they produce. It has never been the proposed that smart mining bolts replace all other mining bolts (this would simply be too expensive) but a well-thought selective replacement has the potential to revolutionise tunnel health. One step further in this methodology, would be to employ a data logger that interrogates the bolts and recognises them on an individual signature. Stresses in bolts could then be used to create a tunnel map of stresses and possible rock movement, with appropriate software.

The last remaining task is then to produce a material that will satisfy the requirements of the prototype design, as well as the strength requirements of the mining standard.

CHAPTER 4

ALLOYING AND PROCESSING

The production of an accurate, sensitive smart mining bolt depends very heavily on the appropriate use of a strain memory alloy. As a material group, however, strain memory alloys vary tremendously in their chemistry and processing. The number of possible alloying elements is almost endless, and although much work has been done on TRIP steels and on metastable austenitic stainless steels [111-159], not much of this work has actually focused on the materials from a structural health monitoring perspective. Ideally, the least cost in alloy development would be incurred if an off-the-shelf material could be used or adapted to suit the purposes of the project at hand, but before even such a simple material solution can be implemented, an understanding of material behaviour, chemistry, processing and transformation influences, is necessary.

4.1 Material Requirements

The objective of a study in alloying effects is undoubtedly a material that fulfils the requirements of a smart mining bolt, and the material characteristics identified as important for the mining environment were therefore the following:

> Good transformation characteristics: the sensitivity of the mining bolt depends on the material beginning to transform as soon as the load on the bolt exceeds the pre-tension load – in other words the incubation strain must be eliminated. A material that exhibits a large amount of transformation for a small bolt deformation is also vital, since the strains experienced by grouted bolts are small compared to the overall length of the bolt.

> Acceptable strength levels for the SABS requirements (as outlined in chapter 3): these strength levels are influenced by alloying chemistry, as well as the subsequent processing of the material.

> Good corrosion resistance: the corrosive chemicals present in some rock types have caused many mines to experience problems with the rusting of mining bolts and subsequent "hidden" loss of the support in tunnel walls.

> Acceptable machinability: due to the fact that some machining of parts would be required for smart bolt manufacturing.

> Cost: Although the smart bolt is envisaged to cost more than an ordinary mining bolt, the material, processing, and manufacturing costs must be kept as low as possible.

Unfortunately, each of the above requirements cannot be met in isolation, many of these requirements influence one another, as seen in Figure 4.1 below, which shows that component sensitivity and accuracy are dependent on two main factors: the design of the inductive circuit used to measure transformation (see chapter 3), and the actual transformation characteristics of the material. The transformation is influenced by only two factors, the alloying chemistry and material processing. These two factors are however related to a myriad of other factors, including each other.
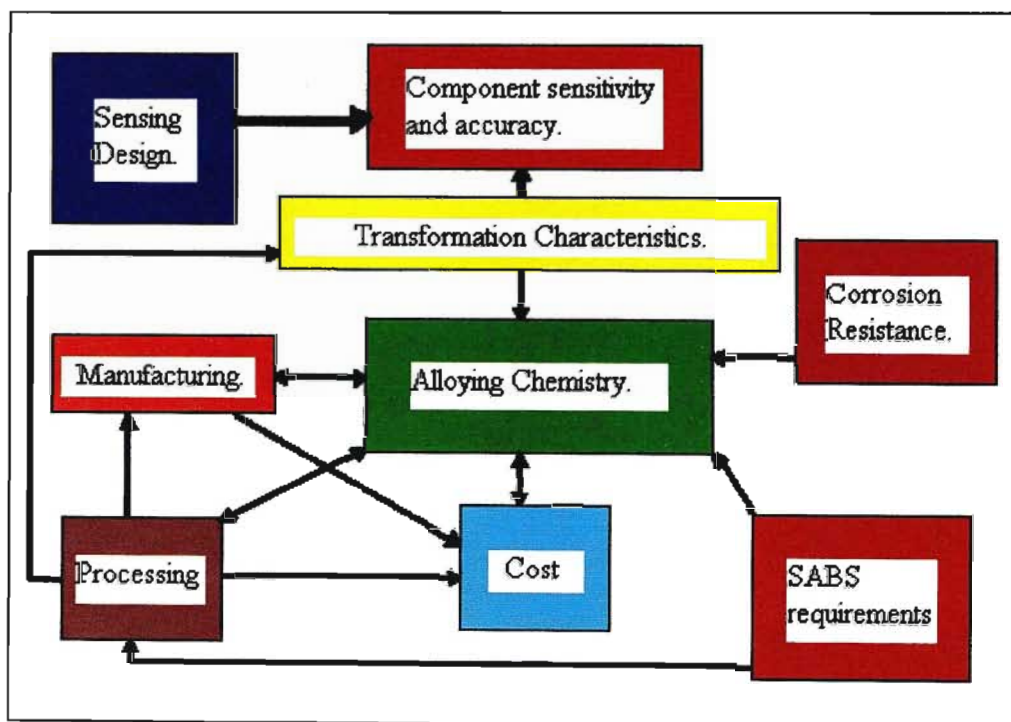
Figure 4. 1: The factors influencing alloy development for the smart mining bolt.

The rest of this chapter is then devoted to an in depth study of alloying chemistry and material processing.

4.2 Alloying Chemistry

The alloys making up the strain memory group are varied in their alloy chemistry and encompass such simple alloys as those of iron-nickel groups, through to complex chemistries incorporating iron (Fe), carbon (C), chromium (Cr), nickel (Ni), manganese (Mn), silicon (Si), nitrogen (N), molybdenum (Mo), and phosphorus (P).

The fundamental property governing whether or not strain memory is present within a particular alloy is the level of stability of the austenite present at room temperature. This in turn is governed by the alloying elements present themselves. The more prominent of these alloying elements will be discussed in detail, including their influences on strength characteristics, transformation mechanics, and corrosion properties. Relative costs and machining parameters will, however, be discussed in chapter 6 where practical alloy formulation and testing is discussed.

The strain memory alloys use iron as a base material, (important for the magnetic properties that make the materials smart) although there are other alloy groups that also display strain-induced transformation (e.g.: titanium [160]). In relation to iron, then, all other alloying elements may be said to have one of two basic actions, according to Wever classification [161]:

> ➤ Those that expand the γ field and therefore encourage austenitic formation over wider compositional limits, - a group known as austenitic stabilisers.
> ➤ Those that contract the γ field and therefore encourage ferritic formation over wider compositional limits - known as ferritic stabilisers.

Four main categories of iron binary diagrams may then be defined: open and closed γ-field systems, and expanded and contracted γ-field systems. A closer look at each of these four field scenarios follows, including a more detailed discussion of the elements having possible relevance to the smart mining bolt alloy development. A generalised example diagram of each scenario is given, but it should be noted that the precise form of the diagram depends on the electronic structure of the actual alloying elements.

4.2.1 Open γ field

An example of an open γ field is given in Figure 4.2 below. The alloying elements that could possibly create this effect include nickel (Ni), manganese (Mn), cobalt (Co), and the inert metals ruthenium, rhodium, palladium, osmium, iridium, and platinum. Both Ni and Mn completely

eliminate the BCC α-iron phase and replace it down to room temperature with the γ-phase, if they are added in sufficient quantity. This depression of the A_{e1} and A_{e3} temperatures makes Ni and Mn important austenitic stabilisers.
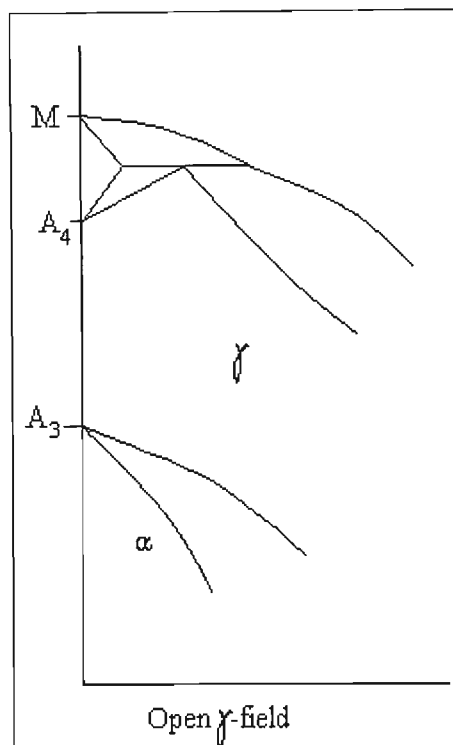
Figure 4. 2: An example of an open γ-field Iron binary phase diagram

Nickel is one of the best-known austenitic stabilisers, and is used extensively in austenitic stainless steels. It is also known to improve corrosion resistance in neutral and weak oxidising media. [162] When added in sufficient quantities, it improves ductility and formability because of the FCC structure it produces at room temperature. As an austenitic stabiliser, Ni depresses the M_s temperature, and it has been shown that a 2.5% change in Ni content can produce up to a 150 °C change in the M_s temperature [163].

Various researchers [including 164] have investigated the iron-nickel-chromium series of alloys, which can be used to produce alloys of very high strengths. Using a base alloy of Fe-0,3C-2Mn-9Cr- and varying the nickel content from 8 to 16% shows quantifies the stabilising effects of nickel. The alloy with the 8%Ni was unstable [164], while increasing the Ni content to 12% produced incredible elongations, implying that both these alloys were transformable. Further increase of Ni content to 16% produced a totally stable alloy.

Manganese is not as powerful an austenitic stabilizer as nickel, but has the added effect of lowering the stacking fault energy. When the stacking fault energy is lowered significantly

enough, stacking faults form which promote the formation of an intermediate (HCP) martensite ε, between the austenite and usual stable α' martensite phases.

To produce alloys of the Fe-Cr-Mn group in which the intermediate martensite is formed, Manganese contents of 10% or greater are required, while the presence of Cr in concentrations of 13 – 18% stabilizes the BCC or α phase field sufficiently to cause the transformation from ε to α martensite. This group of alloys is important from a structural health monitoring perspective because it is not only cheaper then the well known Fe-Cr-Ni stainless steel group, but can also be manipulated to improve the transformation temperature insensitivity of strain memory alloys. To elaborate on this point, consider the diagram shown in Figure 4.3. The amount of martensite formed on application of strain shows a dependence on ambient temperature. This is intuitively correct since martensite formation is usually a thermally induced process (to be further elaborated later) and hence will form in greater quantities as the temperature is depressed.
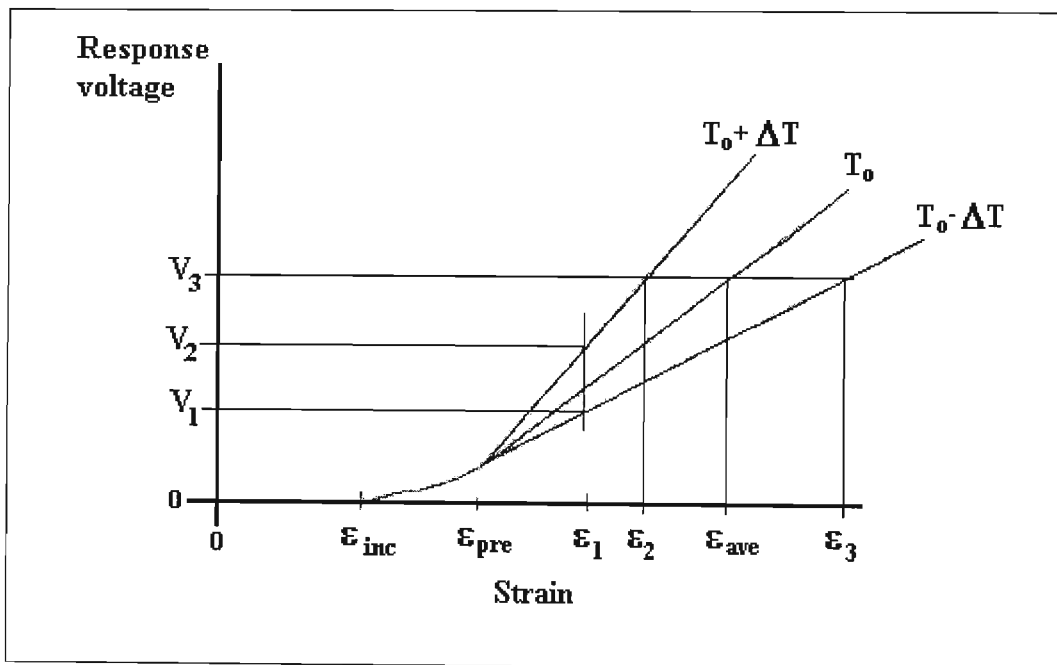
Figure 4. 3: Temperature dependence of martensite formed in normal strain memory alloy

This temperature dependence is in most structural health monitoring systems, not an advantageous characteristic, and if possible best eliminated. This can be achieved by creating ε martensite (which is also paramagnetic) at a temperature lower than the expected operating range, and then allowing the nucleation of α martensite (which nucleates from the ε martensite)

upon straining. The formation of α martensite in this way should be a product of the applied strain only.

4.2.2 Expanded γ field.

Common elements that create the expanded γ-field seen in Figure 4.4 below, are carbon (C), nitrogen (N), copper (Cu), zinc (Zn), and gold (Au). In this case, the austenitic field is expanded but its existence is cut short by the formation of compounds. This group obviously forms a very important set of alloys in the plain carbon steels, which owe their heat-treatability to the expansion of the gamma field by carbon.
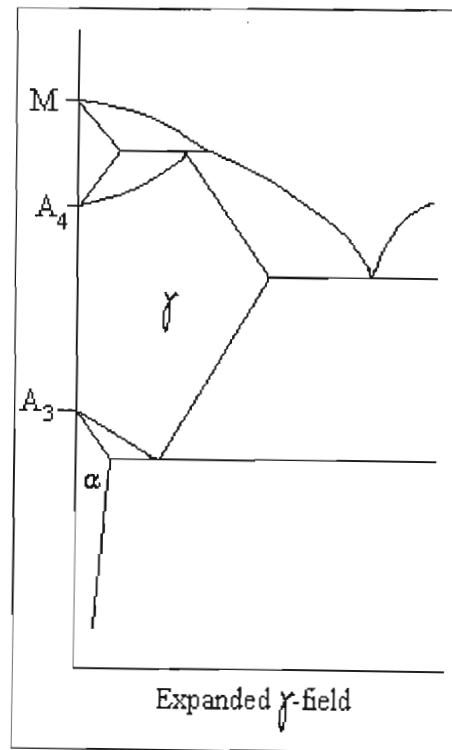
Figure 4. 4: Example of an expanded γ field Iron binary phase diagram

Nitrogen is an exceptionally cheap element to add as an austenitic stabiliser: it is not only much more potent than nickel, but is also a miniscule fraction of the cost. It has therefore been the subject of much research [78,165-167] as a replacement for part of the nickel content of such popular alloys as AISI 301 and 302. Researchers at the University of Cape Town, investigated this possibility using the experimental alloys shown in Table 4.1 below.

Table 4.1: Alloys used in nitrogen replacement

	Cr	Ni	N	C	Mn	Si	V	Cu	Co	Mo	Fe
301	17.7	7.48	0.074	0.029	1.5	0.5	0.07	0.08	0.02	0.03	Bal
A1	17.2	5.12	0.087	0.084							
A3	17.5	5.09	0.129	0.087							
A5	17.9	5.17	0.163	0.075							
A6	17.9	5.03	0.276	0.071							
D1	17.9	3.41	0.185	0.078							
D2	17.9	3.36	0.275	0.070							

The effectiveness of nitrogen as a nickel replacement can be seen in the amount of austenite retained down to room temperature, detailed in Table 4.2 below. Note that ferrite was absent in all cases, and the remainder of the microstructure is therefore composed of martensite.

Table 4.2: Percentage austenite retained at room temperature as nitrogen content is varied

Alloy	301	A1	A3	A5	A6	D1	D2
% retained austenite	98	70	83	89	91	43	67

A careful balance is needed if nitrogen is to be used to partially replace nickel [78]. In the case of alloy designated A6, the nitrogen replacement was most successful, approximately 2.5% of the nickel used in the base 301 alloy, was replaced by 0,2% nitrogen. The austenite was not quite as stabilised as in the case of 301, but comparable properties were attained in terms of work hardening rate. There are however indications that too high a nitrogen level might cause delayed cracking after deep drawing operations [166] - a prevalent use of the 301 type alloys. This cracking, which gets worse with time, is thought to occur because of the embrittling effect the nitrogen has on the martensite.

Although carbon can be used as an austenitic stabiliser, care needs to be taken to prevent the formation of free carbides, which arise as a result of elements such as Cr being leached out of solution by the carbon within certain temperature ranges. To counteract this effect, elements

such as titanium and niobium are sometimes added to prevent chromium carbides forming. Carbon can therefore have a negative effect on corrosion resistance, and as an interstitial can cause a reduction in ductility [162]. Carbon is also known to depress the M_S temperature by approximately 10°C for every 0.01%C present.

Not as commonly used for its austenitic stabilising properties, copper does, however, improve corrosion characteristics, [166] unfortunately usually at the slight expense of ductility [165].

4.2.3. Closed γ field.

Although there are many elements that stabilise the γ phase, there are also many that reduce this phase field and encourage the formation of BCC iron. In Figure 4.5 shown below, it can be seen that the γ area of the diagram has been forced to contract to what is known as the gamma loop. The result is that the δ and α phase fields become continuous. Alloys of which this is true, cannot be heat treated by using the usual cooling through γ/α-phase transformation. Elements that fall into this category include: silicon (Si), aluminium (Al), beryllium (Be), and phosphorus (P); together with the strong carbide formers: chromium (Cr), molybdenum (Mo), titanium (Ti), and vanadium (V).
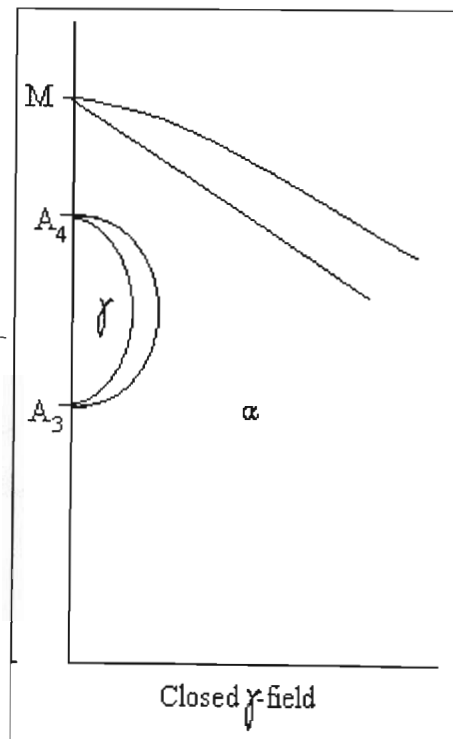
Figure 4. 5: An example of a closed γ-field iron binary phase diagram

Cr is primarily added for the corrosion resistance it imparts, by forming a passive oxide film to protect the underlying surface. As little as 5% improves the corrosion properties of the material, but a minimum of 12 % is required to produce stainless steel. For Cr contents of less than 12 or 13%, there is an austenite to ferrite transformation on cooling from within the γ loop. For Cr contents greater than 13%, a transformation does not occur, rather a solid solution of Cr in α Fe is formed. Cr like Mo and V is known as an effective carbide former. The formation of carbides in strain memory alloys is considered a positive phenomenon, since they enhance dislocation multiplication and pinning at elevated temperatures. This fact, when used in conjunction with a thermomechanical processing of 30% (or more) increases the yield strength at room temperature substantially. Molybdenum is the most effective of the above mentioned three, in enhancing strain hardening properties, and Cr is the least effective. Mo and V can both produce strain hardening that is independent of temperature and strain rate [168,169].

Mo and Si have been shown to improve corrosion resistance [111], and in the case of Mo, specifically the pitting resistance in chloride atmospheres [162]. Al can be added to improve high temperature scaling, and is commonly added, like Ti and Nb, to combine with interstitials and thus prevent sensitisation.

4.2.4 Contracted γ-field

The last group of the four, belongs to those elements that strongly contract the γ loop, but compound formation is present and produced the diagram shown in Figure 4.6 below. Elements belonging to this group are boron (B), and the carbide formers: tantalum, niobium, and zirconium.

Niobium is commonly added as a grain refiner [170], which may then improve strength. As little as 0.13 – 0.22% can result in marked γ grain refinement.
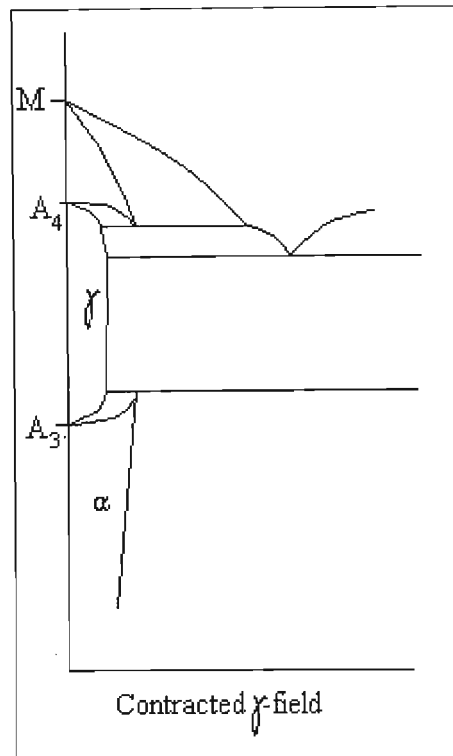
Figure 4. 6: An example of a contracted γ-field iron binary phase diagram

The effects of the elements discussed in the preceding sections can be summarised in the table below:

Table 4.3: The effects of various alloying elements on the stability of the austenitic phase

Alloying Element	Effect on Stacking Fault Energy	Austenising Index
Ni		1
Cr	Lowers the SFE [25]	-
Mn	Lowers the SFE	½
N	Raises the SFE [102]	25
C		30
Mo	Lowers the SFE [25]	-
Si		-
V	Lowers the SFE [25]	-

58

Although the effects of each of the most prominent alloying elements has been discussed in relation to Iron, most alloys are not binary in nature, as several elements are added for the different properties that they produce. For example, in the case of the smart mining bolt, it is necessary to add chromium for corrosion resistance, as well as some austenitic stabilisers to produce the metastable austenitic phase at room temperature. The interaction of these two elements is therefore the question at hand.

As an answer to this dilemma, one may scrutinise what is known as the Schaeffer-De Long diagram, which uses a calculation of chromium and nickel equivalence to predict the phases that will be present in material, for any given composition. Figure 4.7 shows this diagram, wherein the chromium equivalent is calculated as follows:

$$C.E. = \%Cr + \%Mo + 1.5\%Si \qquad (4.1)$$

and the nickel equivalent is calculated with the formula:

$$N.E. = \%Ni + 30\%C + 0.5\%Mn + \%Co + 25\%N \qquad (4.2)$$
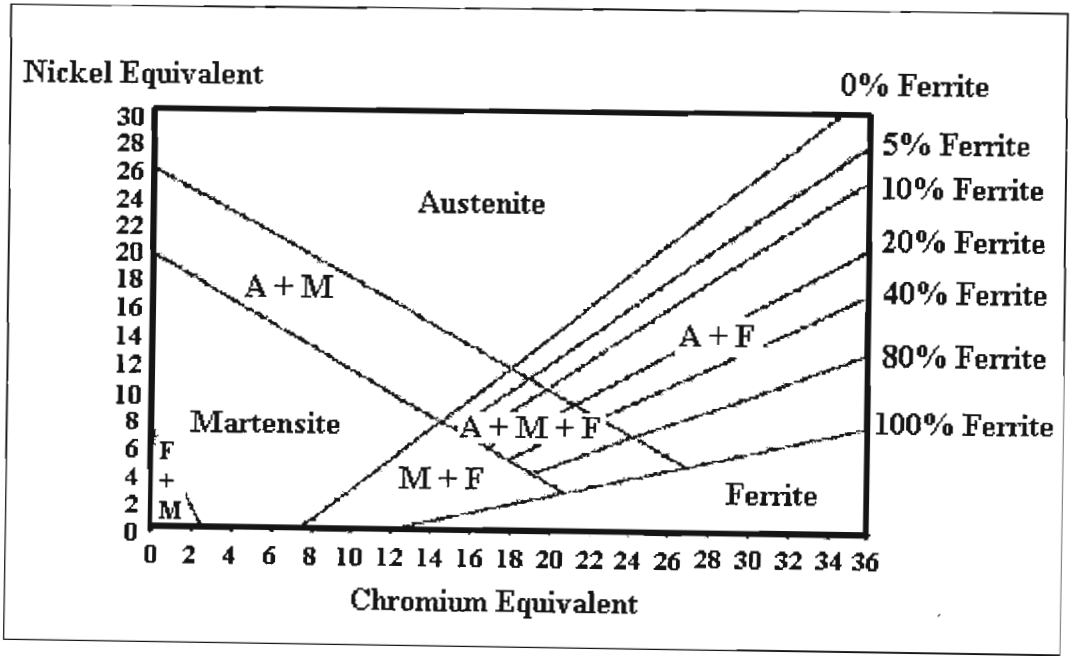
Figure 4. 7: The Schaeffler De Long diagram for prediction of phases present in complex alloying chemistries

Figure 4.8 shown below has regions, corresponding to the commercially available stainless steel grades, marked on it. Figure 4.9 has a region identified by researchers at Mintek, as the most likely region to produce the smart steels known as strain memory alloys.
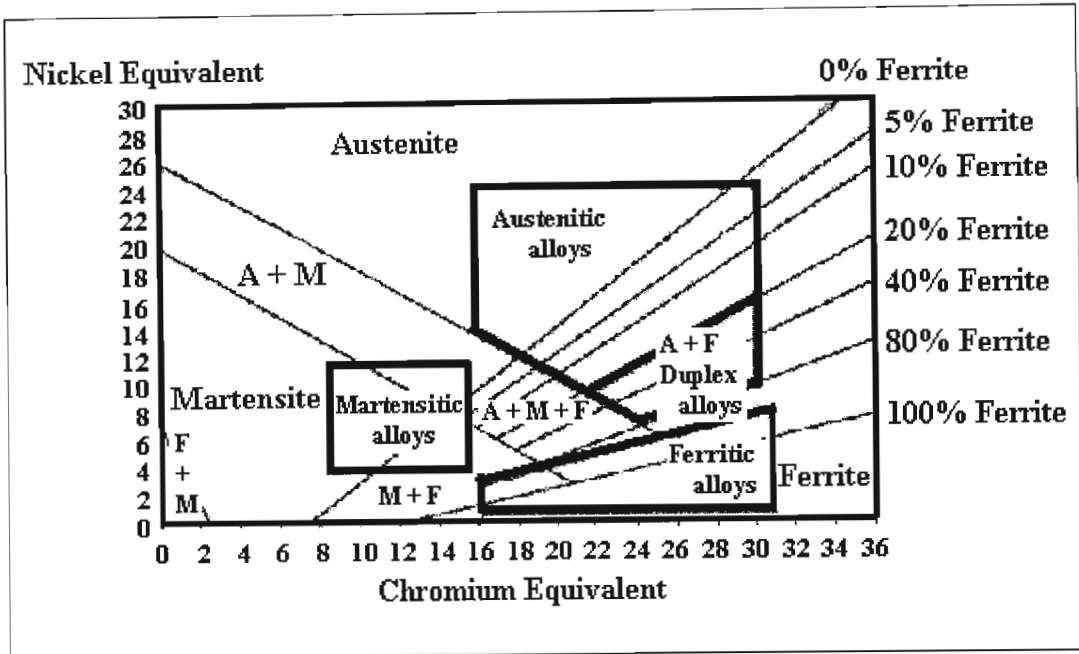
Figure 4. 8: The four groups of commercially available stainless steels depicted on the Schaeffler De Long diagram
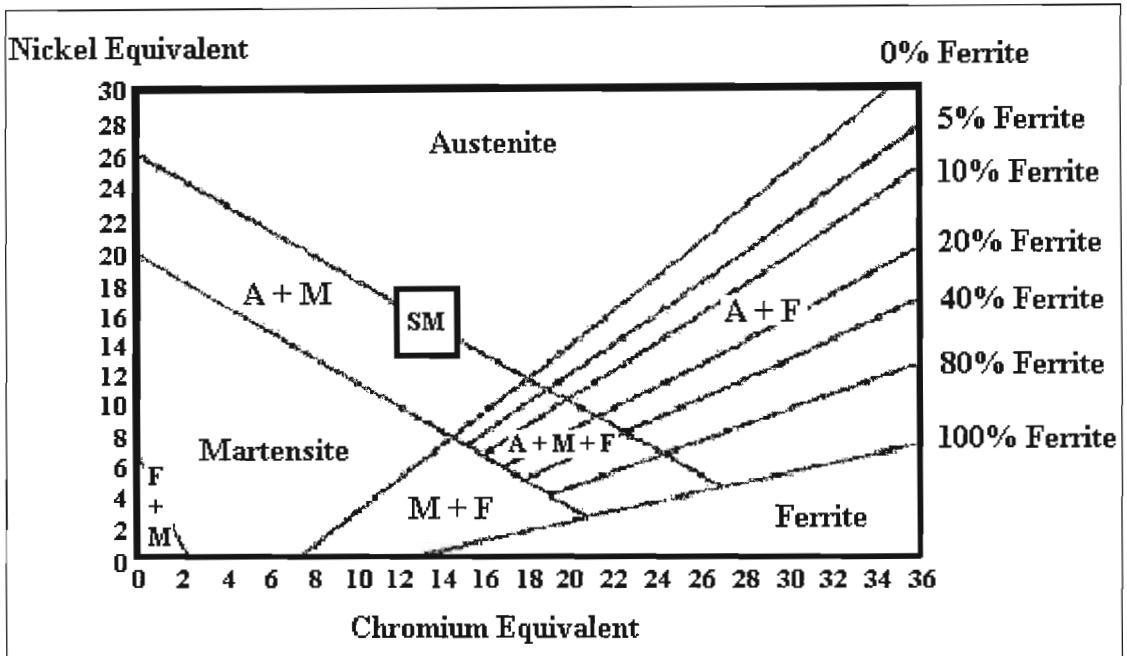
Figure 4. 9: The region of Chromium and Nickel equivalence on the Schaeffler De Long diagram most likely to produce strain memory alloys

4.3 Material Processing

After casting and rolling to produce a wrought material, alloys may be further processed to increase their yield strength, and/or destabilise their austenitic structure, thereby making them more sensitive to strain-induced transformation. Usually steels are strengthened (apart from the strength imparted by the alloying itself) by one of two means: either they are heat treated using the classical γ/α transformation which is not applicable in this case, since the alloys we are dealing with have been engineered to remain austenitic down to room temperature; or the material can be cold-worked, thereby increasing the dislocation density and increasing the yield strength. This approach is also not applicable in this class of materials, because cold working would entail deformation, which would immediately trigger the strain-induced martensitic transformation. This is highly undesirable if the material is to be used in a strain monitoring application. It therefore becomes necessary to look more closely at the transformation characteristics of this particular class of materials, in order to obtain a means of increasing yield strength without actually creating martensite.

4.3.1. Time Temperature Transformations

A common manner of representing the dependence of isothermal transformation with time and temperature, below the eutectoid temperature, is a set of curves known as TTT (time-temperature- transformation) curves. Figure 4.10, shown below, is the simple curve for a plain carbon eutectoid steel. In this case, the roughly C-shaped curve simply contains a pearlite reaction down to the nose of the curve, with bainite and martensite occurring at lower temperatures. For hypo- and hyper-eutectoid steels the diagram becomes more complex with the addition of additional lines for ferrite and cementite reactions.

61
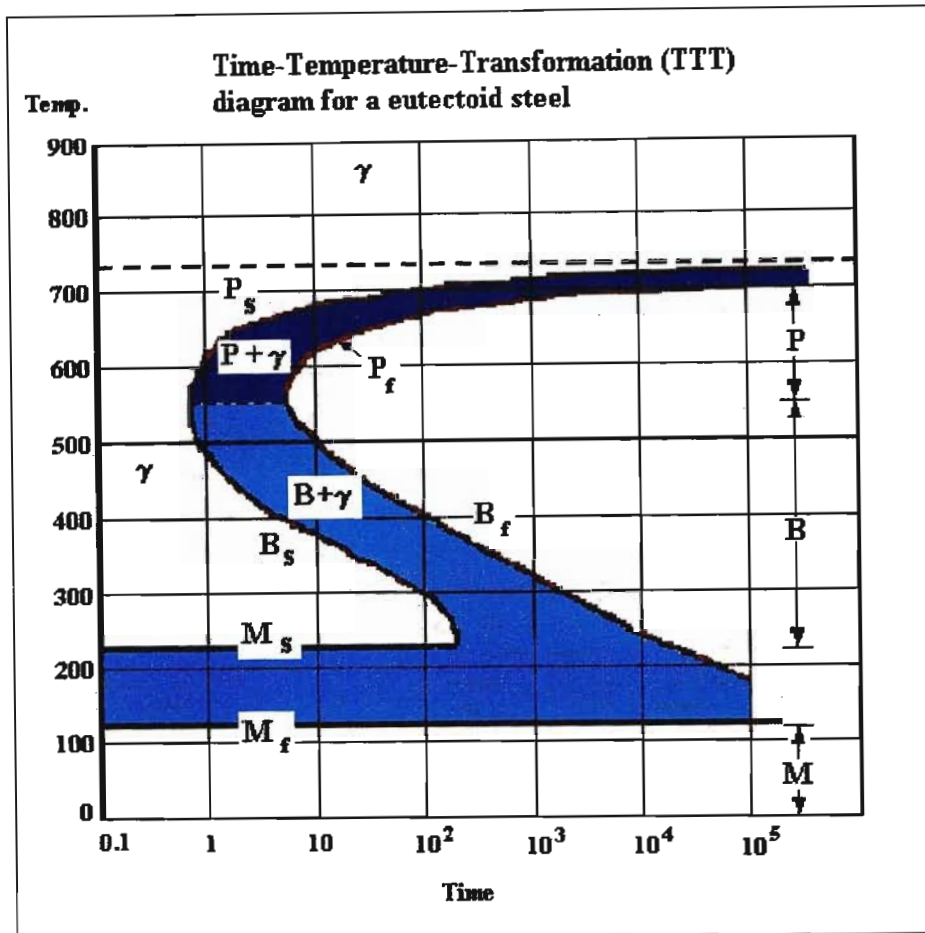
Figure 4. 10: An example of the TTT curve for a plain carbon eutectoid steel

Figure 4.10 clearly indicates both the martensite start and finish temperatures, termed the M_s and M_f temperatures respectively. Although these temperatures are considered important for the spontaneous thermal formation of martensite, which is usually achieved through heat treatment processes, their position relative to the operating temperature also influences strain-induced formation of martensite. A third quantity pertaining to martensitic formation is also commonly defined. The M_D temperature is the temperature above which the formation of martensite due to strain ceases to occur. This temperature is different for different types of loading, [169] that is for tensile and compressive loading conditions, the temperatures above which transformation will no longer occur, will be different. The quantity M_D does not however appear in Figure 4.10, since it is related neither to time, nor directly to temperature.

The effects of alloying elements on this diagram are two-fold: the nose of the C-shaped curve is moved usually to longer times by the vast majority of alloying elements, and secondly, those alloying elements (such as nickel and manganese) which expand the γ-field also depress the

position of the curve with respect to temperature. In contrast, those elements that favour the ferrite phase raise the curve higher with respect to temperature.

Additionally, some researchers [171] have found that it is possible to create a metastable bay in the TTT curve if certain alloying is present. Figure 4.11 shows as example of this bay, the creation of which the researchers attributed to additions of chromium.
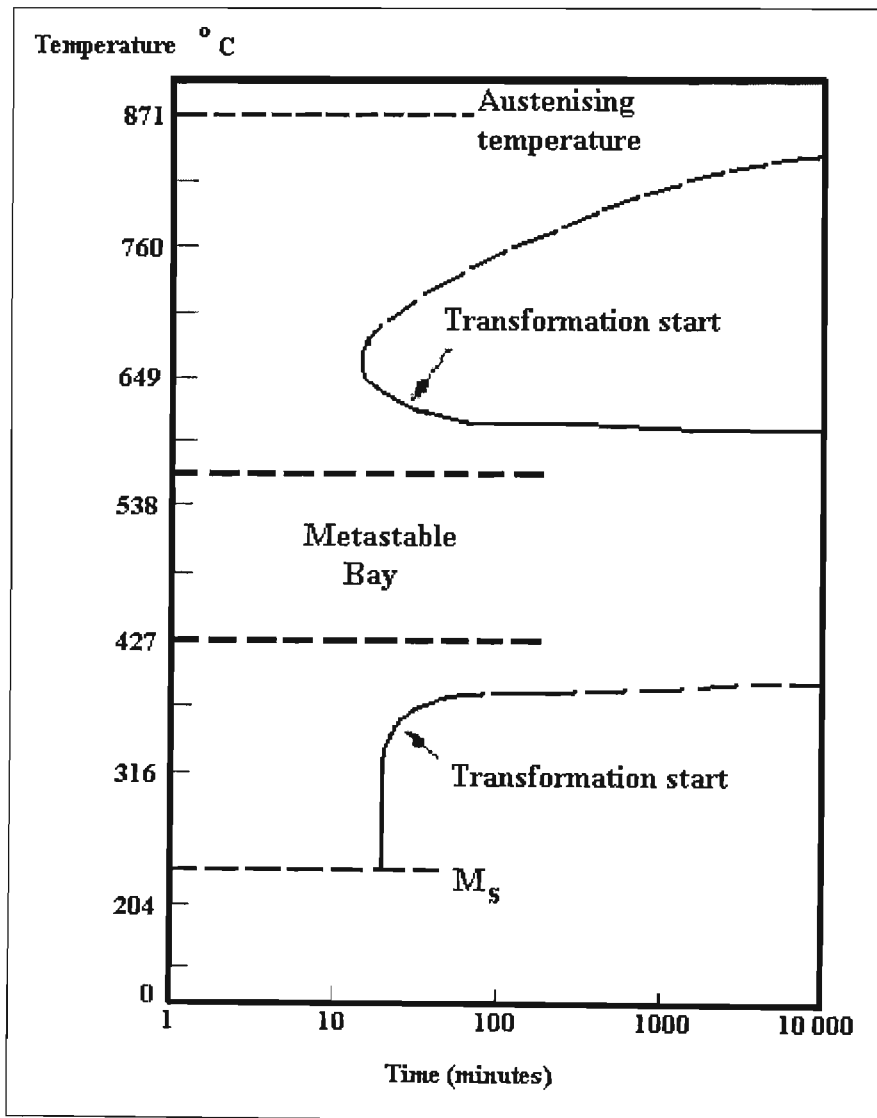
Figure 4. 11: An example of a metastable austenitic bay engineered into the TTT curve by alloying chemistry [171]

4.3.2. Processing

In the light of the opportunity created by the metastable bay of Figure 4.11, processing may therefore be developed around a warm working process. That is, it is neither strictly speaking a

63

hot working process nor a cold working process, but work may be put into the material by a suitable means at an elevated temperature, which falls within the metastable bay for the particular alloy concerned. Usually, this mechanical working is a rolling process, although extrusion has also been considered [171] and rejected because of the adiabatic heating associated with this process. Warm working, in this manner, would seem to shorten the time to decomposition of austenite into other phases. Although the time to decomposition seems infinite in the metastable bay area of Figure 4.11, this diagram is altered by warm working [171].

This classical method of increasing strength in metastable alloys, has been termed Prior Deformation of Austenite (PDA). Figure 4.12 illustrates the effects of 0, 20, 40, 60, 80% PDA (curves 0,1,2,3,4 respectively), on the stress-strain curve of a typical metastable alloy. The strength increment associated with increased amounts of PDA is clearly visible.
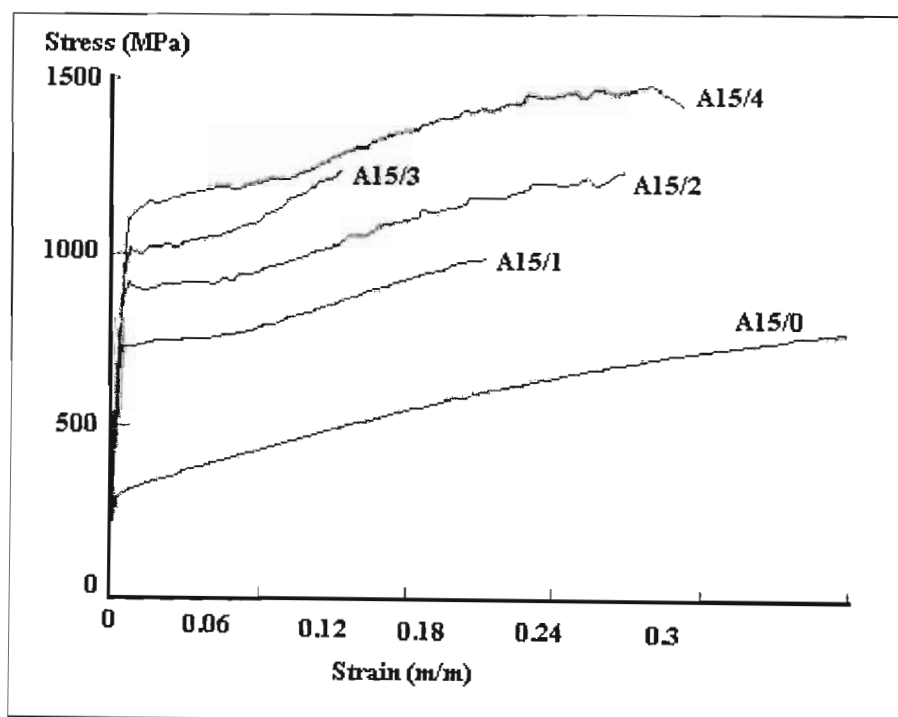
Figure 4. 12: The effects of %PDA on the stress strain curve of a typical metastable alloy

The effect of PDA is however, not limited to a higher strength increment, but also promotes the formation of carbides, where carbide-forming elements are included in the alloy chemistry [172]. These carbides have been shown to raise the M_D temperature, thereby broadening the temperature range within which martensite can be induced by strain [172]. The means by which the PDA is introduced is also shown to influence the M_D temperature [173] due to the fact that martensitic nucleation is highly influenced by the dislocation substructure imparted during PDA.

An alternative to warm rolling is a thermo-mechanical processing route involving deformation in the intercritical region and subsequent cooling through pearlite and bainite regions [174-177]. This route has seen development specifically because the industrial scale operations have deemed it more cost effective. The result is a multi-phase steel, which is TRIP-aided, i.e. some austenite has been retained for transformation to martensite, but bainite, pearlite, etc. make up the rest of the room temperature microstructure. Although this method produces structural steels with optimised properties, it is not particularly useful in producing strain memory alloys, of sensitive proportions.

The classical thermo-mechanical treatment has seen significant research and development. However, another method of increasing strength has also been proposed by Koppenaal et al [178] for the replacement of the costly thermomechanical treatment, with a thermal process said to achieve similar strength levels.

As the nominal composition for his experimental alloy, Koppenaal used one very similar to one used by Zackay et al in their research on TRIP steels (thermomechanical processing) [143]. The principle argument of Koppenaal rests on the strength that can be imparted to austenite through the reverse martensite shear transformation or reverted austenite. By cycling repetitively between a martensitic and reverted austenite structure, strengthening is said to occur. There are, however several requirements, in terms of alloy characteristics, that must be met in order for this process to have the desired effect:

> The amount of martensite that can be formed by cooling to liquid nitrogen temperature, must be large enough to be significant.
> The austenite recrystallisation temperature must be above the austenite reversion temperature.
> The M_D temperature must be raised by thermal processing, if it is below room temperature for the annealed material state, as is the case for the alloy used by Koppenaal.
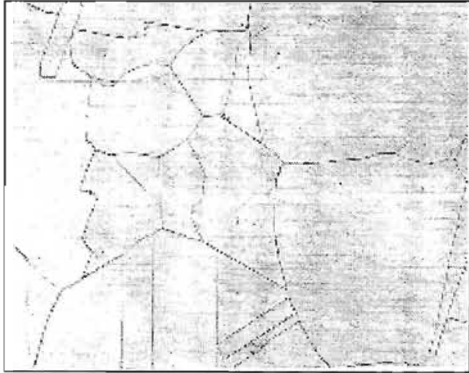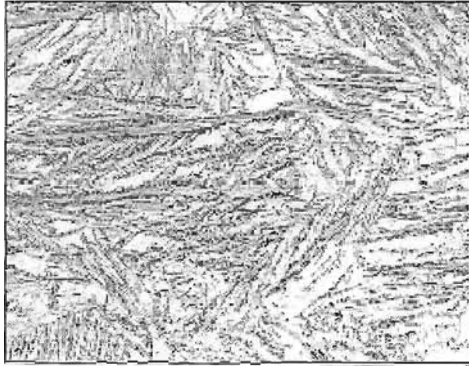
Very briefly, the method employed by Koppenaal proceeded as follows:
Austenised, water quenched samples of the alloy Fe – 24.5Ni – 4.1Mo – 0.29C had a hardness of 80 HR_B. These samples were then cooled to –175°C and returned to room temperature. The hardness of the $\gamma + \alpha^l$ structure then measured between 31.5 and 33 HR_C. Samples were then immersed in salt baths of varying temperatures (500 – 940 °C) and air cooled to room temperature. The microstructure could now be considered as reverted austenite, with a hardness

of approximately 27.5 HR$_C$, which is appreciably harder than the as quenched austenite. Several further cycles of this nature were performed with the result shown in the figure below. The final reversion to austenite (after 5 cycles) produced a hardness of approximately 44 HR$_C$.

The microstructures formed at each point of the above thermal process are shown below:

Table 4.4: Microstructures at various points in thermal processing method

Figure 4. 13: As quenched austenite structure

Figure 4. 14: Structure after cooling to liquid nitrogen and returning to room temperature

Figure 4. 15: Reverted austenite + virgin austenite after cooling to liquid nitrogen and reverting in a salt bath (>99% austenite)

Figure 4. 16: Martensite, reverted austenite and virgin austenite after a second cooling to liquid nitrogen temperatures

The properties attained within this material, with a thermal process can be favourably compared with the very similar alloy used by Zackay and his colleagues, which was subjected to a thermo-mechanical process. A comparison is tabulated below:

Table 4.5: Comparison of thermal and thermo-mechanical processing

Alloy	Treatment	σ_y (MPa)	UTS (MPa)
Fe – 24Ni – 4Mo – 0.3C	Thermo-mechanical reduction of 80% at 517°C	1130.78	1213.52
Fe – 24.2Ni – 4.1Mo – 0.29C	5 thermal cycles between –175°C and 722°C	1117	1330.74
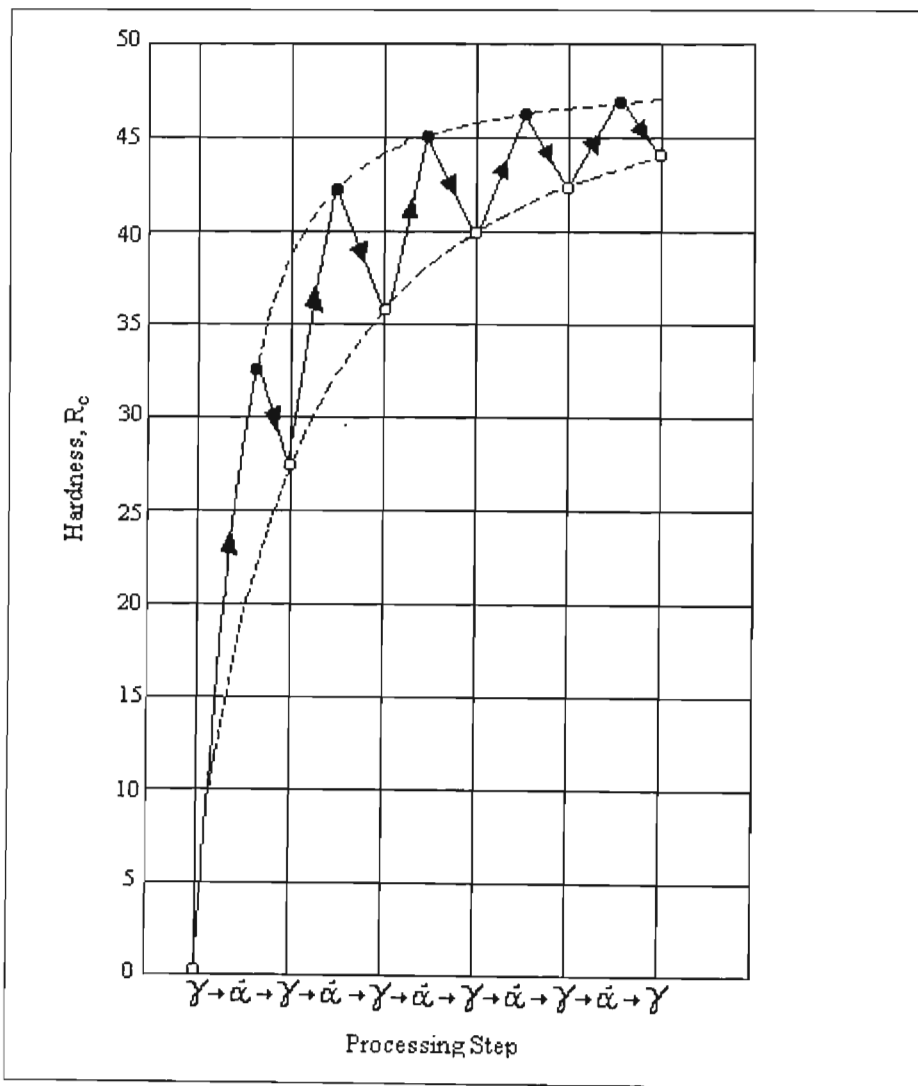
Figure 4. 17: Hardness variation with thermal processing technique

4.3.3. Effects of processing on stability and transformation

The most significant effect of processing is obviously to raise the strength of the material. This is, however, not the only effect. The figure shown below indicates how the stability of the austenite changes dependent on the level of thermo-mechanical processing.
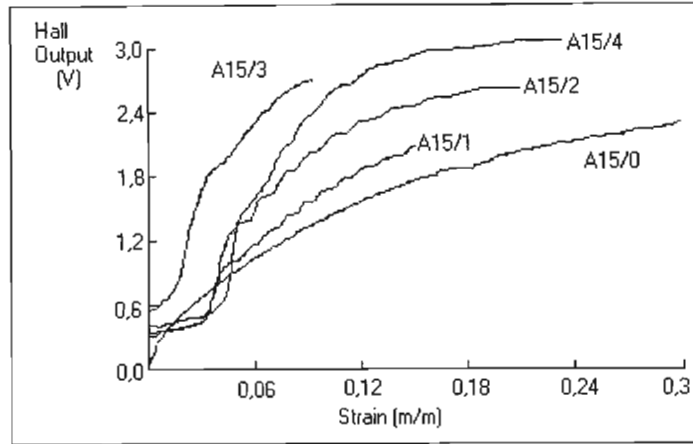
Figure 4. 18: The influence of %PDA on austenitic stability

In the figure above, the alloy has been given the designation A15, and the indices 0, 1, 2, 3, and 4, again (as in Figure 4.12) indicate percentages of mechanical working, for example, 1 indicates 20% work, and 4 indicates 80% work. The Hall effect/probe has been used to determine the amount of strain–induced martensite that presents. Thus, it is clear that the greater the amount of working, the steeper the transformation rate, and therefore the more destabilised the austenite.

Prior Deformation of Austenite (PDA) at some temperature above the M_D increases the dislocation density and thereby provides more sites for nucleation of martensite. Chemical changes such as the formation of carbides during PDA, mean that some of the austenitic stabilising elements are leached out of the austenitic matrix, thereby destabilising it chemically [179]. Thus, warm working the austenite produces microstructural as well as chemical changes that influence stability with respect to strain-induced transformation.

The temperature (θ_a) at which this prior deformation is introduced has some effect on the ease of transformation, as well as some effect on the M_D temperature. When θ_a is much higher than M_D a higher yield stress is produced than when θ_a is close to M_D, but the transformation is easier for the latter case [164,180]. The volume of martensite at a given strain varies with the

68

temperature of the PDA as well as with the amount of PDA. It is also interesting to note that θ_a and M_D are not unrelated: a higher θ_a produces a lower M_D.

Stability of austenite may therefore be said to be dependent on three parameters [164]:

- The chemistry
- The processing history, and
- The test environment

The first two of these factors have now been extensively dealt with, but the third will be discussed in more detail in the following chapter wherein the influences of external conditions on transformation mechanics are discussed.

The martensitic product phase itself is also influenced by prior deformation of austenite: it is found [171] that the martensite produced from austenite, which has been worked, is finer than that produced in material which has not undergone any prior working. And, that the degree of refinement is proportional to the amount of PDA. This martensitic refinement is postulated to be due to one or many of the following factors:

- More nucleation sites for the martensite, due to the increased grain boundary area.
- Bending the austenitic lattice may restrict the martensitic shear to shorter plate lengths.
- Heavily worked slip bands may block the progress of advancing martensitic plates [181].
- Distorted austenite grain boundaries may be more effective in limiting the size of martensite platelets.

4.4 Mechanical properties of strain memory alloys

The fact that austenite transforms to martensite with the application of strain means that various mechanical properties of these materials differ substantially from their ordinary stainless steel or structural steel counterparts.

4.4.1 Stress-strain curves

The unique flow curves observed in transforming metastable austenitic steels, have been the subject of much investigation [168, 182, 183]. Researchers Ludwigson and Berger [183] proposed a relationship predicting (with a good degree of accuracy) the variation of stress with strain, as follows:

$$VFM = \left(1 + \frac{\varepsilon^{-B}}{A}\right)^{-1}$$ (4.3)

wherein   VFM is the Volume Fraction of Martensite,

        ε is strain,

        A is a measure of the propensity to transform, and

        B measures the autocatalytic nature of the martensitic transformation

The true stress σ may then be expressed as:

$$\sigma = K\left[\ln(1+\varepsilon)\right]^{n}(1 - VFM) + C(VFM)^{Q}$$ (4.4)

Wherein   K is termed the austenite strength factor,

        n is the austenite strain-hardening index,

        C is the martensite strength factor, and

        Q is the martensitic strengthening index.

For a given family of compositions, the indices n and B are found to be constant, but K, C, Q, and A are influenced by small compositional changes. [183] The interstitial elements carbon and nitrogen are found to strongly increase the value of K and C, as well as the yield strength. The substitutional elements manganese, nickel and chromium, however do not seem to really influence the value of K, and only slightly increase C, with nickel having no effect on C at all. The value of A, is decreased by manganese, nickel, and chromium, but a more marked decrease is again produced by carbon and nitrogen. The index Q, is reduced again by carbon and nitrogen, and to a lesser extent by nickel. Thus carbon and nitrogen, as interstitial elements have been found to strengthen both austenite and martensite phases far more than their substitutional counterparts manganese, nickel and chromium, making them more effective in strengthening the austenite-martensite composite. [183] Strain-hardening has also been enhanced by the carbide forming elements such as Mo and V, and to a lesser extent Cr, which progressively lower the stacking fault energy.

4.4.2 Fracture and crack propagation characteristics

The formation of martensite has proven both advantageous and deleterious for the fracture and fatigue properties of metastable alloys, depending on the composition of the alloy, the temperature of testing, as well as the exact conditions of testing.

Fracture toughness has been observed to incur a ductile to brittle transition [184] with respect to fracture of the strain-induced phase, dependent on the carbon content of the material. Alloys

having between 0.2 and 0.24% carbon show fracture of martensite first, then tearing in the adjacent austenite and finally local fracture in the austenitic regions perpendicular to macroscopic crack growth direction. Alloys having between 0.27 and 0.35% carbon show the same fracture process, but the martensite cleaves at lower temperatures instead of tearing.

Fatigue Crack Growth Properties are enhanced by the martensitic transformation. Although a purely martensitic has a fatigue crack growth rate one order of magnitude higher than pure annealed stable austenite, it is still a widely documented fact that as the amount of martensite formed during cycling increases, the fatigue crack growth rates (FCGR) decrease [163]. And, larger amounts of PDA are found to be more beneficial for fatigue crack propagation properties than smaller amounts [179]. Fatigue crack propagation is a result of cumulative damage caused by strain cycling ahead of the crack tip. High cyclic plastic strain causes martensite to form, which tends to increase the effective strain hardening rate, which should give rise to higher fatigue crack propagation rates. Also, the formation of martensite in the ductile austenite, decreases the amount of strain accumulation required to cause fracture ε_f. But, all these negative factors are offset by the large energy absorbing effect of strain-induced transformation [163,179]. On a more macroscopic level, crack initiation is positively affected by the transformation process, because the martensite that forms as a microscopic region undergoes plastic deformation, tends to reduce the stress concentration and or change the stress field in that area [78]. Crack propagation in a material that already consists of both austenitic and martensitic phases, also benefits from the dual phases, because crack propagation in the relatively brittle martensitic phase is arrested when it reaches the retained austenitic grains. Under increasing load, the crack then branches and grows around the retained austenite grain [170]. Crack branching is usually considered to produce long crack propagation times, or less steep da/dN curves.

In contrast to the advantageous effects experienced by the fatigue crack propagation properties, low cycle fatigue properties are adversely affected [172,185]. Martensitic transformation during cycling produces cyclic hardening, instead of cyclic softening. And, in this case, the less PDA applied to the material the better: 80% PDA may produce tire tracks on the fracture surface, while 20% PDA produces serpentine glide and considerable stretching.

4.4.3 Ductility

Figure 4.19 shows a comparison of strength and ductility ranges for TRIP and metastable alloys compared to other grades of steel, where metastable steels refers to alloys not having undergone any PDA, in contrast to TRIP steels which would have undergone varying degrees of PDA. The

extraordinary ductility experienced by both classes of material, has been directly attributed to the transformation induced by straining.

The greatest ductility has been found to occur in metastable alloys, when the martensitic formation occurs at an optimum rate. This rate is dependent on both the strain rate, as well as the temperature of martensitic formation. The maximum elongation is achieved when martensite is formed little by little, rather than 1) very rapidly during the early stages of deformation

OR 2) when the total amount of martensite formed during the late stages of straining, is very small.

The first of these situations tends to occur when the deformation temperature is just above the M_s temperature, and the second tends to occur just below the M_D temperature. The elongation therefore peaks somewhere between the M_s and the M_D temperatures [186,187,164,78].

4.4.4 Strength properties

As already discussed, the strength of TRIP steels in particular (those having undergone PDA) is attributable in large part to the thermo-mechanical processing they undergo, and although some credit must be given to the part played by alloying chemistry, the high strength produced particularly in TRIP steels is said to be attributed to work hardening, carbide precipitation, and dislocation pinning by segregated solutes, all of which are caused by thermo-mechanical processing [173].
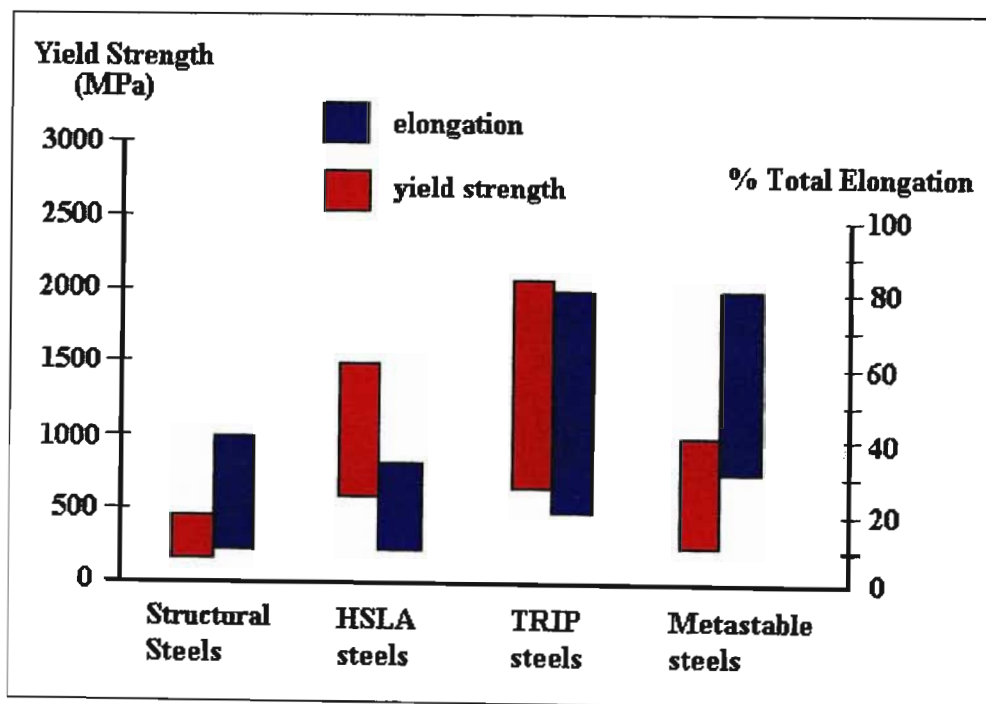
Figure 4. 19: Comparison of strength and ductility for various grades of steel

4.5 Conclusion

Considering the material strength requirements (identified in the SABS standard for mining bolt materials) as well as the cost restraints, an attempt will be made to avoid the costly step of thermo-mechanical processing, and if needed a thermal processing route may be investigated. Alloy groups holding the most promise for adaptation to this smart component could be those of the Fe-Cr-Ni and Fe-Cr-Mn families, and as such are likely to form the first target groups for development.

CHAPTER 5

TRANSFORMATION MECHANICS

The transformation from austenite, to martensite is most commonly a Face Centred Cubic to Body Centred Cubic or Body Centred Tetragonal transformation, as shown below in Figure 5.1.

$$FCC\gamma \to BCC\alpha^l$$

OR
$$FCC\gamma \to BCT\alpha^l$$
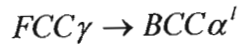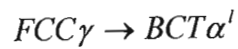
It is this transformation that is responsible for the smart properties of strain memory alloys, as well as the extraordinary strength and ductility combinations found in TRIP steels, and some metastable austenitic alloys.
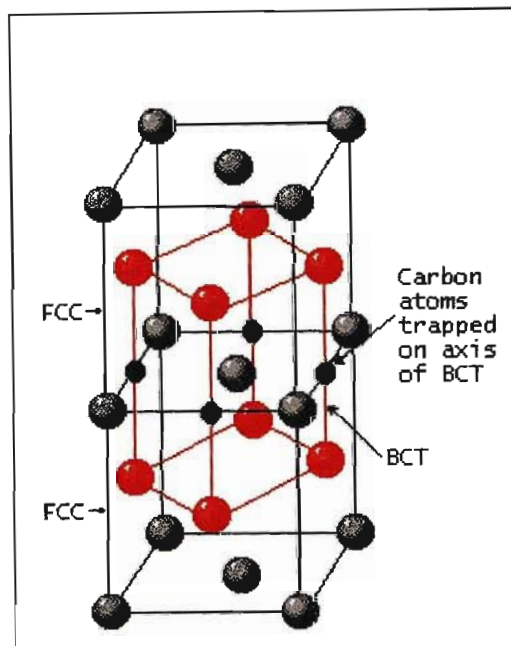
Figure 5. 1: FCC and BCT cells are related to one another.

If however, the stacking fault energy of the alloy is low enough, a further intermediate phase forms, which is of Hexagonal Close-Packed (HCP) crystal structure.

$$FCC\gamma \to HCP\varepsilon \to BCC\alpha^l$$

This ε martensite is not ferromagnetic and therefore does not contribute to the smart properties of strain memory alloys, it does however become important in the Fe-Cr-Mn alloys in which low stacking fault energies are prevalent. The micromechanisms involved in these

transformations are of some interest, if the transformation itself is to become a controllable variable in alloy production. The factors influencing micro-mechanics of transformation will therefore be examined in some detail in the sections that follow.

5.1 Energy involved in transformation

The transformation from austenite to martensite is more commonly a thermally induced process, which requires rapid cooling from austenite through the M_S and M_f temperatures as seen in figure 4.10 on the TTT diagram. A stress or strain induced martensite may, however, also be formed in thermal equilibrium up to the M_D temperature. Figure 5.2, shown below, indicates the Gibb's free energy change associated with thermal and strain induced transformations. In order for the transformation to occur, the free energy of the system must decrease and nuclei must be present. Possible nuclei include defect sites and concentrations of dislocations [169].
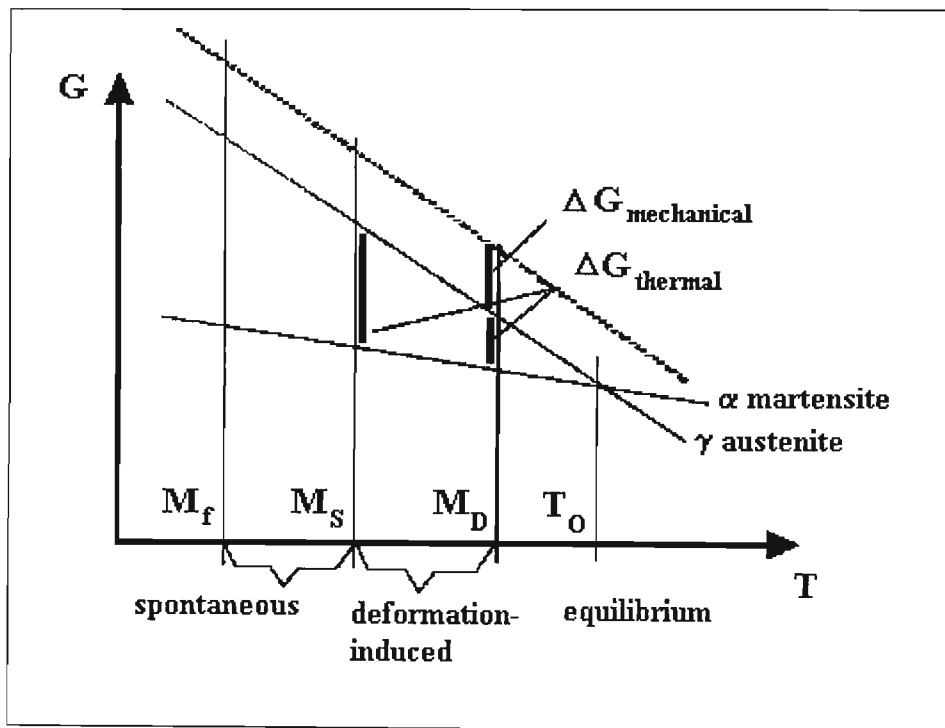
Figure 5. 2: Energy contributions to martensitic transformation [188]

The relative contributions of thermal, stress and strain energies to the production of martensite form a complex problem, which will receive in-depth attention in sections 5.3 and 5.4 dealing with a proposed model for martensitic nucleation. But the various energy contributions mentioned above are also important from a purely microstructural perspective, as different morphologies of martensite can be observed to emanate from different controlling parameters.

5.2 Stress-assisted and strain-induced martensite

Several researchers have shown [173,164,189,112] that martensitic morphology is dependent on the means of nucleation and growth distinct in thermal spontaneous martensite, stress-assisted martensite, and strain-induced martensite. Near the M_S temperature, stress-assisted martensite dominates but near the M_D temperature, strain-induced martensite forms [164].

Stress-assisted martensite can be said to form in some alloys in the presence of an applied stress, but it forms by the same nucleation and growth process as that found to be present in martensite formed spontaneously on cooling below the M_S temperature. The morphology of this type of martensite is essentially of plate form, although variations in exact morphology and amount present do vary depending on the temperature of its formation. Examples of plate martensite in Fe-Ni-C alloys are shown in the figures below [173]. The plate martensite is internally twinned and said to be lenticular, having a midrib as evidenced in the figures below, which show stress-assisted martensite that formed in Fe-Ni-C samples having an M_S temperature of -72°C, in tension.

Not alloys, however, produce stress-assisted martensite. It has been found to occur in certain Fe-Ni-C alloys as a result of the interaction between applied stress and transformation strain, giving an energetic contribution to the martensitic transformation driving force [173] As the temperature of formation moves from the M_S temperature, continuously higher, the morphology of stress-assisted martensite in these alloys is found to change from identical to that formed spontaneously by cooling, to much smaller plates formed in much smaller amounts, until approximately 70°C above the M_S it ceases to form altogether.

Figure 5.3(a): Stress-assisted martensite formed at –70°C

Figure 5.3(b): Stress-assisted martensite formed at –50°C

Figure 5.3(c): Stress-assisted martensite formed at –30°C

Figure 5.3(d): Stress-assisted martensite formed at 0°C
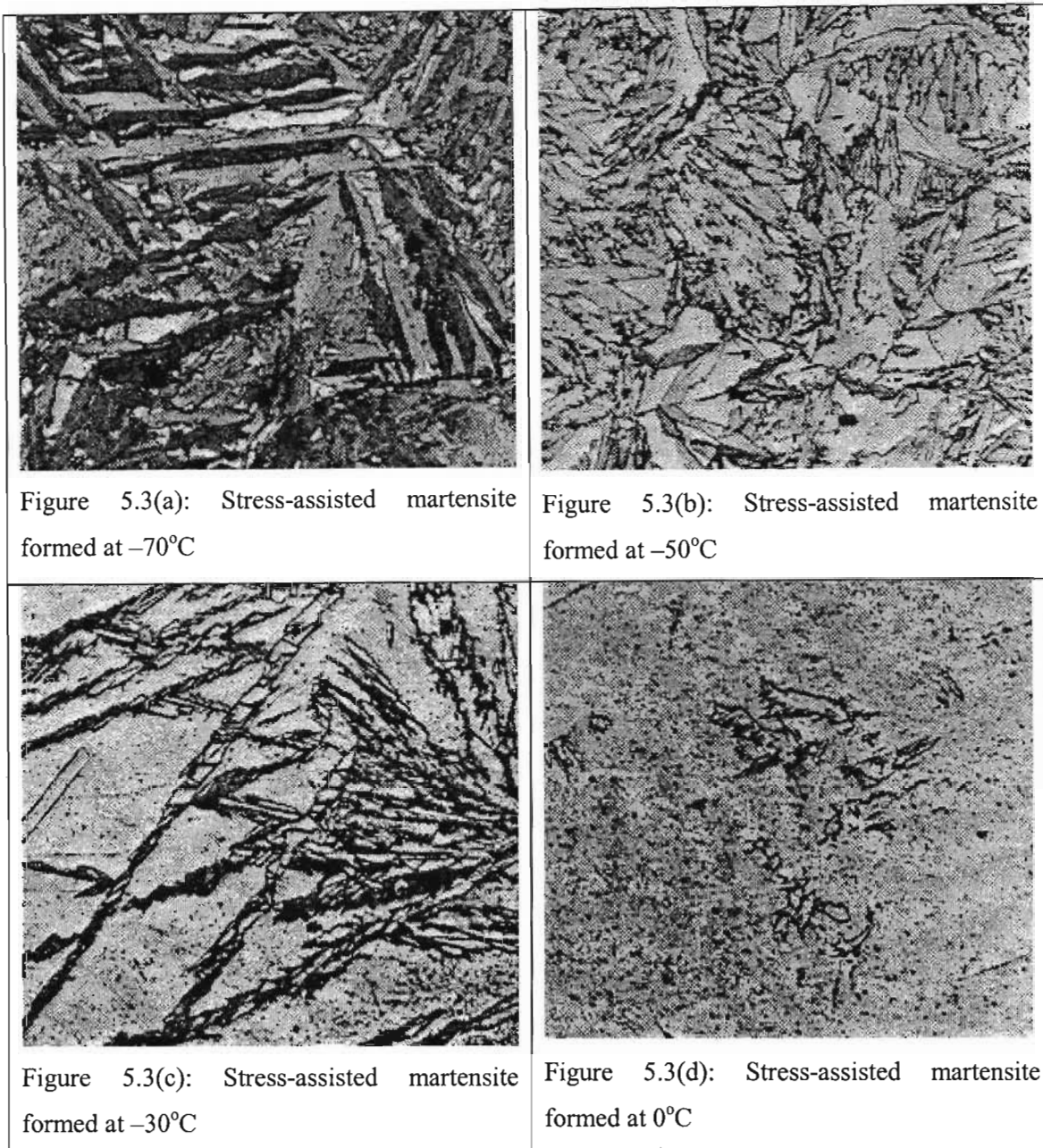
Figure 5.3: Micrographs of stress-assisted martensite formed at various temperatures.

Strain-induced martensite, in contrast, is the transformation product that forms as a direct result of plastic strain; and, although it has the same crystal structure as stress-assisted martensite, the morphology, distribution and temperature dependence are different to that produced by stress-assisted means or spontaneous means. The difference in this morphology can clearly be seen if the figures shown below are compared with those above. Strain-induced martensite is said to consist of laths that collect in elongated clusters along the slip bands. There is clear evidence that this particular type of martensite forms as a result of dislocation interactions and processes [189].
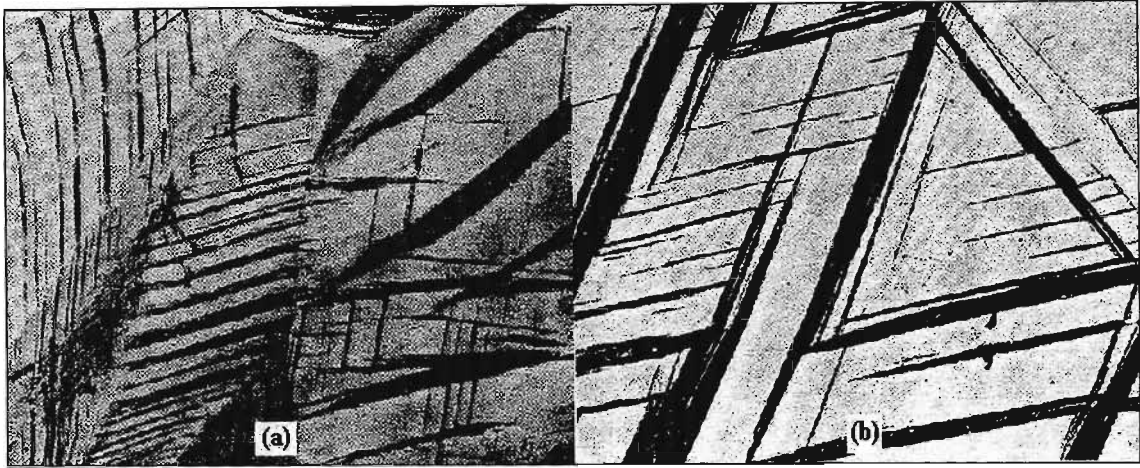
Figure 5. 4: (a) Strain induced martensite formed at 180°C in an alloy with M_S=-36°C
(b) Strain induced martensite formed at 106°C in an alloy with M_S=-36°C

Strain-induced martensite can be found to form up to 300°C above the M_S temperature, and is concentrated on the slip bands on the $\{111\}_\gamma$ planes in the parent austenite.

The more complex transformation that includes an intermediate ε martensite phase requires conditions of low stacking fault energy, and specific dislocation interaction - more specifically, the overlap of stacking faults on alternating close-packed planes [190]. Figure 5.5 below shows an example of regions of fault overlap and the initiation of the HCP transformation. Heavy faulting is evident in these HCP bands. Low strains and low temperatures favour the formation of ε martensite rather than twins [189].
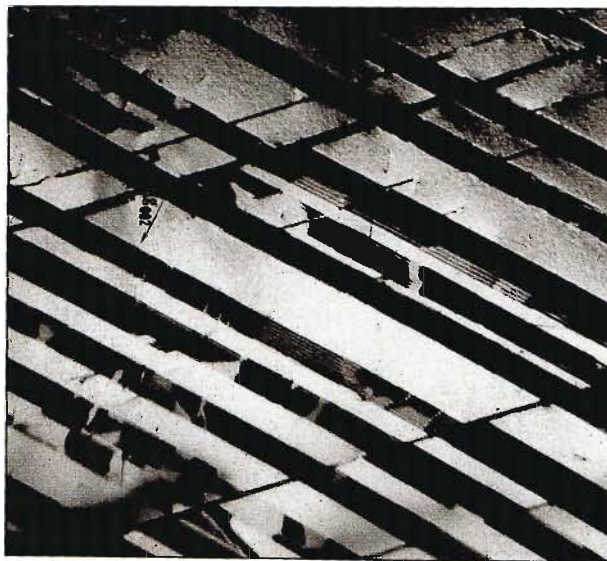
Figure 5. 5: Bands of stacking faults with HCP nucleation

Figure 5.6 shows the intersection of HCP bands, prior to the formation of the BCC α phase, which has been shown to consistently nucleate at intersections of HCP bands [180,190] (see Figure 5.7) and shows up as the white phase visible and the intersections of the dark HCP bands.

Figure 5. 6: The intersection of HCP bands.

Figure 5. 7: The nucleation of α martensite

The α phase has also been shown to nucleate at intersections of an HCP band and stacking faults in the FCC matrix, as seen in Figure 5.8 below.

Figure 5. 8: Intersection of HCP bands and FCC stacking faults

The growth of the α phase then proceeds in the locations of previous HCP bands as seen in Figure 5.9 below – note the big white cross formation of α martensite.

Figure 5. 9: BCC martensite growth

5.3 Modelling the transformation

Many researchers have produced models for the various transformation processes that have been identified at a microstructural level. The exceptionally rapid growth of martensitic particles, has suggested that the kinetics of isothermal martensitic transformation, is essentially nucleation controlled; that is, the initial growth of the embryo and the conditions causing its growth, are the key questions in the theory of martensitic transformation [191-193].

One of the classical works on the theory of nucleation was produced by Olsen and Cohen who proposed a dislocation model to describe the generation and development of the martensitic embryo [194-196]. From the considerable transmission electron microscope work that has been produced specifically to observe the strain-induced martensitic form and orientation relationships [169] Olsen and Cohen postulated that faulting on the planes of closest packing, formed the first step in the martensitic nucleation process. Further, that the faulting displacements are derived from an existing defect, while matrix constraints cause all the subsequent processes to occur, leaving the fault plane unrotated, as observed by many researchers.

Basic concepts of classical nucleation theory then suggested that the stacking fault energy consists of both volume energy and surface energy contributions as follows [194]:

$$W = n\rho(\Delta G + E) + 2\gamma, \tag{5.1}$$

where W is the fault energy, expressed per unit area of fault (in the fault plane),

n is the number of atomic planes (in thickness) composing the fault,

ρ is the density of atoms in a close-packed plane in moles per unit area,

ΔG is the chemical free energy difference between parent and product phases,

E is the strain energy, and

γ is the free energy per unit area of the particle/matrix interface.

The terms ΔG and E are defined in (eqn. 5.1) as molar quantities. When the volume energy contribution $(\Delta G + E)$ is negative, the fault energy decreases with increasing fault thickness (once the surface energy contribution, which is always positive, is overcome) such that the fault energy associated with the simultaneous dissociation of an appropriate group of dislocations can

be zero or negative. This condition leads to the spontaneous formation of a martensitic embryo at the observed M_s temperature.

The above-mentioned dislocation models produced by Olson and Cohen [194-196] produce a good description of the thermodynamics and the geometry of spontaneous martensitic nucleation, but do not take detailed cognisance of elastic stress fields associated with the martensitic embryo, nor its growth under external loading, as is vital for strain memory alloy applications. Their estimate for the strain energy term E was obtained using the Eshelby solution for an elastically isotropic inclusion, in an elastically isotropic matrix of the same elastic modulii, neglecting such considerations as the energies of elastic interactions of the transformation dislocations with remnant defect configuration, as well as between themselves.

Several revisions to the original theory by Olsen and Cohen have been proposed, but of greatest interest is the work pertaining to the transformation from FCC austenite to HCP martensite or ε martensite as it is known. A well-studied phenomenon [197-265] this is the simplest of the martensitic transformations, but one of great importance for low stacking fault energy strain memory alloys, such those of the Fe-Cr-Mn group discussed in chapter 4 to hold a great deal of promise for the smart mining bolt. In recent years computer simulations have been used extensively (and from a variety of perspectives) to study and predict martensitic transformation [266-268], but the original Olsen-Cohen model can be adapted to include elastic fields and energy of the martensitic embryo, by incorporating both dislocation and disclination terms.

5.3.1 A revised model for the γ (FCC) - ε (HCP) transformation

Common agreement [194,264,265,270] defines the most likely sites of FCC to HCP transformation to be those of higher dislocation density where the elements of dislocation structure have long-range elastic fields similar to those of a super-dislocation, in other words, it occurs preferentially at twin or grain boundaries and parallel to active slip planes [189]. Consider then a low-angle symmetric tilt grain boundary (GB) modelled as an infinite wall of straight edge dislocations (or intrinsic dislocations), which contains a number of extrinsic lattices dislocations stored from the prior deformation of austenite (PDA), as shown in Figure 5.10(a) below.
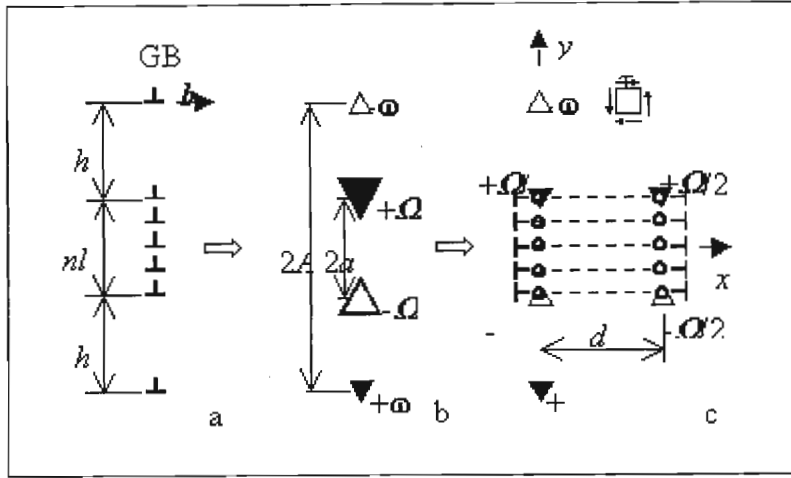
Figure 5. 10: Dislocation-disclination model of HCP-martensite embryo nucleation at a tilt grain boundary with extrinsic dislocations

The angle of misorientation across the grain boundary, and its period, are defined as ω and h, respectively, and the spacing between the extrinsic lattice dislocations is l, which is equal to double the interplanar distance between $\{111\}_\gamma$ (close-packed) planes in austenite. The group of extrinsic lattice dislocations together with the two closest intrinsic grain boundary dislocations (both the extrinsic and intrinsic dislocations have equal Burgers vectors b) may be geometrically described as a two-axes dipole of partial wedge disclinations [271] having the strength $\pm \Omega = \pm b / l$ (as seen in Figure 5.10 (b)). The dipole arm is equal to $2a$. In a similar way, one can consider two other semi-infinite parts of the initially infinite dislocation wall as another two-axes dipole of partial wedge disclinations, with the strength $\pm \omega = \pm b / h$ and arm $2A$ (see Figure 5.10 (b)). It follows from the theory of disclinations [271] that such a disclination configuration creates elastic stress fields whose long-range component decreases like that of a superdislocation.

Under the action of an external shear stress τ, each of the extrinsic lattice dislocations and the two closest intrinsic dislocations, will split into two Shockley partial dislocations. One of these Shockley partials will remain within the grain boundary while the other (whose Burgers vector is closest in alignment to the direction of the applied shear stress) will glide along the $\{111\}_\gamma$ plane and produce a stacking fault behind itself. As a result of the overlapping stacking fault, an embryo of ε martensite nucleates [194].

Thus, referring to Figure 5.10 (c) the dislocation-disclination model may be said to comprise:
  ➤ Two equivalent disclination dipoles having the strength $\pm \Omega / 2$ and modelling two walls of edge component Shockley dislocations with Burgers vector $\pm b_e = \pm \Omega l / 2$.

➢ Two walls of screw-component Shockley dislocations with Burgers vectors $\pm b_s$, and

➢ Two rows of continuously distributed virtual edge dislocations with infinitesimal Burgers vectors $\pm b_v$ and infinitesimal spacing s.

This gives the well-known transformation strain $\varepsilon_{yy} = -b_v / s$ inside the embryo of ε-martensite. And, the elastic fields of the martensitic embryo are then given by the simple superposition of elastic fields created by the above dislocation and disclination configurations.

5.3.2 The energy gain due to martensitic embryo nucleation

If W_1 is defined as the total free energy characteristics of the initial state of the system (Figures 5.10 (a) and (b)) and W_2 is that characteristic of the final state, (Figure 5.10 (c)) then the energy gain due to the ε-martensite embryo nucleation at a low angle grain boundary under the action of an external shear stress is given by

$$\Delta W = W_2 - W_1 \qquad (5.2)$$

which, according to [194], may be written as

$$\Delta W = n\rho\Delta G d + \Delta E + 2\gamma d, \qquad (5.3)$$

where ΔW and ΔE are determined per unit dislocation (disclination) length,

d is the embryo size along the $\{111\}_\gamma$ plane, and

the term $\Delta E = E_2 - E_1$ is calculated as follows:

The total energy E_1 of the defect configuration shown in Figure 5.10(b), may be given by

$$E_1 = E_\Omega^s + E_\omega^s + E_{\Omega-\omega}^{\text{int}} + E_\Omega^c + E_\omega^c, \qquad (5.4)$$

where E_Ω^s is the self elastic energy of the dipole of Ω-disclinations,

E_ω^s is the self elastic energy of the dipole of ω-disclinations,

$E_{\Omega-\omega}^{int}$ is the energy of elastic interaction between the dipoles of Ω- and ω-disclinations,

E_Ω^c is the sum core energy of dislocations modelled by the dipole of Ω-disclinations,

and E_ω^c is the sum core energy of dislocations modelled by the dipole of ω-disclinations.

The first two terms are calculated as work done to generate the appropriate dipoles in their proper elastic stress fields [344]. They read

$$E_\Omega^s = D\Omega^2 a^2 [2\ln R/(2a)+1], \tag{5.5}$$

$$E_\omega^s = D\omega^2 A^2 [2\ln R/(2A)+1], \tag{5.6}$$

where $D = \mu/[2\pi(1-\nu)]$,

μ is the shear modulus,

ν is the Poisson ratio, and

R a characteristic parameter of screening of the disclination long-range elastic fields (e.g., the size of a sample).

The term $E_{\Omega-\omega}^{int}$ is calculated as work done to generate the dipole of Ω-disclinations in the stress field of the dipole of ω-disclinations as follows

$$E_{\Omega-\omega}^{int} = \Omega \int_{-a}^{a} dy \int_{0}^{R} \sigma_{xy}^{\omega}(x,y,A)\,dx \tag{5.7}$$

According to [271]

$$\sigma_{xy}^{\omega}(x,y,A) = D\omega x \left\{ \frac{y-A}{x^2+(y-A)^2} - \frac{y+A}{x^2+(y+A)^2} \right\}. \tag{5.8}$$

As a result, we find

$$E_{\Omega-\omega}^{int} = D\Omega\omega \left\{ -2aA + (A-a)^2 \ln\frac{R}{A-a} - (A+a)^2 \ln\frac{R}{A+a} \right\}. \tag{5.9}$$

The sum core energy E_Ω^c is given as a well-known approximation [278] by

$$E_\Omega^c = D\Omega ab.$$ (5.10)

The sum core energy E_ω^c is determined by the similar expression

$$E_\omega^c = D\omega(R-a)b.$$ (5.11)

The total energy E_1 has now been found in terms of all its constituents, but the same process must now be followed for the energy E_2 for the defect configuration of Figure 5.10 (c). This may be written as:

$$E_2 = 2E_{\Omega/2}^s + E_\omega^s + E_{\Omega/2-\Omega/2}^{int} + E_{\Omega/2-\omega}^{int} + 2E_{\Omega/2}^c + E_\omega^c + E_v + E_{scr}^{el} + 2E_{v-\Omega/2}^{int} + E_{v-\omega}^{int} + E_{scr}^c - E^{ext}$$
(5.12)

where $E_{\Omega/2}^s$ is the self elastic energy of a dipole of $\Omega/2$-disclinations,

$E_{\Omega/2-\Omega/2}^{int}$ is the energy of elastic interaction between the dipoles of $\Omega/2$-disclinations,

$E_{\Omega/2-\omega}^{int}$ is the energy of elastic interaction between both the dipoles of $\Omega/2$-disclinations and the dipole of ω-disclinations,

$E_{\Omega/2}^c$ is the sum core energy of dislocations modelled by the dipole of $\Omega/2$-disclinations,

E_v is the total elastic energy of virtual dislocations,

E_{scr}^{el} is the total elastic energy of screw-component Shockley dislocations,

$E_{v-\Omega/2}^{int}$ is the energy of interaction between the ensemble of virtual dislocations and a dipole of $\Omega/2$-disclinations,

$E_{v-\omega}^{int}$ is the energy of interaction between the ensemble of virtual dislocations and the dipole of ω-disclinations,

E_{scr}^c is the sum core energy of screw-component Shockley dislocations, and

E^{ext} is the work done by the external shear stress to move a dipole of $\Omega/2$-disclinations to a distance d.

Analogous to eqn. 5.5, the first term $2E^s_{\Omega/2}$ reads

$$2E^s_{\Omega/2} = D\Omega^2 a^2 \left\{ \ln\frac{R}{2a} + \frac{1}{2} \right\}.$$
(5.13)

The second term is given by eqn. 5.6, as before.

The energy of elastic interaction between the dipoles of $\Omega/2$-disclinations, $E^{int}_{\Omega/2-\Omega/2}$, is calculated as work done to generate one dipole of $\Omega/2$-disclinations in the stress field of the other dipole of $\Omega/2$-disclinations as follows:

$$E^{int}_{\Omega/2-\Omega/2} = \frac{\Omega}{2} \int\limits_{-a}^{a} dy \int\limits_{d}^{R} \sigma^{\Omega/2}_{xy}(x,y,a)\,dx$$
(5.14)

Again according to [271]

$$\sigma^{\Omega/2}_{xy}(x,y,a) = \frac{D\Omega}{2} x \left\{ \frac{y+a}{x^2+(y+a)^2} - \frac{y-a}{x^2+(y-a)^2} \right\}.$$
(5.15)

As a result,

$$E^{int}_{\Omega/2-\Omega/2} = -\frac{D\Omega^2}{8} \left\{ 4a^2 \ln\frac{d^2+4a^2}{R^2} + d^2 \ln\frac{d^2+4a^2}{d^2} - 4a^2 \right\}.$$
(5.16)

The energy of elastic interaction between both the dipoles of $\Omega/2$-disclinations and the dipole of ω-disclinations, $E^{int}_{\Omega/2-\omega}$, is calculated in a similar way and finally reads

$$E^{int}_{\Omega/2-\omega} = \frac{D\Omega\omega}{4} \left\{ (A-a)^2 \ln\frac{R^4}{(A-a)^2[(A-a)^2+d^2]} \right.$$
$$\left. - (A+a)^2 \ln\frac{R^4}{(A+a)^2[(A+a)^2+d^2]} + d^2 \ln\frac{(A+a)^2+d^2}{(A-a)^2+d^2} - 8ad \right\}.$$
(5.17)

The sum core energy of dislocations modelled by the dipole of $\Omega/2$-disclinations, $E_{\Omega/2}^c$, is similar to eqn. 5.10 and is given by

$$E_{\Omega/2}^c = D\Omega ab / 4.$$

(5.18)

The total elastic energy of virtual dislocations, E_v, is found as the work done to generate them in their total elastic stress field:

$$E_v = -\frac{\varepsilon_{yy}}{2} \int_{-a}^{a} dy \int_{0}^{d} \sigma_{yy}^v (x, y, a, d)\, dx$$

(5.19)

with

$$\sigma_{yy}^v(x,y,a,d) = D\varepsilon_{yy} \left\{ \frac{x(y+a)}{x^2+(y+a)^2} - \frac{x(y-a)}{x^2+(y-a)^2} - \frac{(x-d)(y+a)}{(x-d)^2+(y+a)^2} + \frac{(x-d)(y-a)}{(x-d)^2+(y-a)^2} \right.$$
$$\left. - 2\arctan\frac{y+a}{x} + 2\arctan\frac{y-a}{x} + 2\arctan\frac{y+a}{x-d} - 2\arctan\frac{y-a}{x-d} \right\}.$$

(5.20)

After some algebra, eqn. 5.19 results in

$$E_v = \frac{D\varepsilon_{yy}^2}{2}\left\{ 3d^2\ln\frac{d^2}{d^2+4a^2} + 4a^2\ln\frac{d^2+4a^2}{4a^2} + 16ad\arctan\frac{2a}{d} \right\}.$$

(5.21)

The total elastic energy of screw-component Shockley dislocations, E_{scr}^{el}, is calculated in a similar way thus giving

$$E_{scr}^{el} = \frac{Db_s^2(1-\nu)}{2l^2}\left\{ d^2\ln\frac{d^2}{d^2+4a^2} + 4a^2\ln\frac{d^2+4a^2}{4a^2} + 8ad\arctan\frac{2a}{d} \right\}.$$

(5.22)

The energies of interaction between the ensemble of virtual dislocations and dipoles of $\Omega/2$-disclinations, $E_{v-\Omega/2}^{int}$, and ω-disclinations, $E_{v-\omega}^{int}$, are found to be equal to zero. This is also clear from the symmetry of the system with respect to the x-axis. In fact, the contribution of the positive disclinations to the interaction energy is compensated by that of the negative disclinations. Thus,

$$E_{v-\Omega/2}^{int} = E_{v-\omega}^{int} = 0.$$

(5.23)

The sum core energy of screw-component Shockley dislocations may be approximated [278] by

$$E_{scr}^c = 2D(1-v)b_s^2 \frac{a}{l}.$$

(5.24)

The work done by the external shear stress τ to move a dipole of $\Omega/2$-disclinations (this shear stress does not affect other defect configurations of the system) to the distance d may be written as

$$E^{ext} = \tau\Omega ad.$$

(5.25)

Thus, the total energy of the initial state defect configurations, E_1, is given by eqn. 5.4 with eqn. 5.5, eqn. 5.6, and eqns. 5.9-5.11. The final state E_2, is given by eqn. 5.12 with eqn. 5.6, eqn. 5.13, eqns. 5.16-5.18 and eqns. 5.21-5.25. The final expression for their difference $\Delta E = E_2 - E_1$ than reads (in units of D)

$$
\begin{aligned}
\Delta E &= -\frac{\Omega^2 a^2}{2}\left\{1 + 2\ln\frac{R}{2a} - \ln\frac{R^2}{d^2+4a^2} + \frac{d^2}{4a^2}\ln\frac{d^2+4a^2}{d^2}\right\} - \Omega a\left\{\frac{b}{2} + \frac{\tau d}{D}\right\} \\
&+ \frac{\Omega\omega}{4}\left\{(A+a)^2\ln\frac{(A+a)^2+d^2}{(A+a)^2} - (A-a)^2\ln\frac{(A-a)^2+d^2}{(A-a)^2} + d^2\ln\frac{(A+a)^2+d^2}{(A-a)^2+d^2}\right\} \\
&+ \frac{\varepsilon_{yy}^2}{2}\left\{3d^2\ln\frac{d^2}{d^2+4a^2} + 4a^2\ln\frac{d^2+4a^2}{4a^2} + 16ad\arctan\frac{2a}{d}\right\} \\
&+ \frac{b_s^2(1-v)}{2l^2}\left\{4al + d^2\ln\frac{d^2}{d^2+4a^2} + 4a^2\ln\frac{d^2+4a^2}{4a^2} + 8ad\arctan\frac{2a}{d}\right\}.
\end{aligned}
$$

(5.26)

Substitution of eqn. 5.26 into 5.3 gives the free energy gain, ΔW, due to ε-martensite embryo nucleation at a low angle grain boundary under the action of an external shear stress.

5.4 Results and Discussion of model verification

To numerically analyse the model presented above, it was convenient to use the same values for various parameters as those used by Olsen and Cohen in the material they studied. These values are summarised in the table below:

Table 5.1: Materials properties used in model verification.

Material parameter	Value [266]
No. of planes comprising fault n	8
Density ρ	3.9×10^{-5} mols.m^{-2}
Shear modulus μ	74 GPa
Poisson's ratio ν	1/3
Strength of disclination Ω	$1/\sqrt{6}$
p	3.6 Å
Transformation strain ε_{yy}	-0.01
Spacing between extrinsic lattice dislocations l	$p\sqrt{3}$
Burgers vector b	$(p\sqrt{2})/2$
Burgers vector of edge component of Shockley dislocation, b_e	b/2
Burgers vector of screw component of Shockley dislocations, b_s	$p/(2\sqrt{6})$
Half the dipole arm a	$p2\sqrt{3}$
Size of sample R	10^{-2} m

Two different cases are then considered: zero shear stress, and non-zero shear stress. The results and effects of various parameters are discussed in the sections that follow.

5.4.1 The case of $\tau = 0$

Consider Figures 5.11(a) and (b) shown below. This figure shows 4 different curves corresponding to the elastic energy gain ΔE given by eqn. 5.26 [curve 1], the total free energy gain ΔW [curve 2], the free interface energy $2\gamma d$ [curve 3], and the chemical free energy gain $n\rho\Delta Gd$ [curve 4], respectively, that is each curve represents a term in the equation 5.3. When the external shear stress is absent (as in the case under consideration) A=3a, and the normalised embryo size $\tilde{d} = d/2a$ increases. Again the same constant values have been used as those by Olsen and Cohen [194] shown in Table 5.2 below.

Table 5.2: Additional properties used in model verification

Parameter	Value
ΔG	-126J/mole
γ	0.01J/m^2
Temperature	200K

5.4.1.1 The contributions to the total free energy gain ΔW

When the embryo is small (see Figure 5.11(a)), the total free energy gain ΔW is negative and achieves its minimal value at $\tilde{d} = \tilde{d}_{eq}$ which may be considered as an equilibrium size of the martensitic embryo. This result is quite different from standard descriptions of the homogeneous nucleation of a new phase embryo where no equilibrium embryo sizes exist. However, in the case of heterogeneous martensitic nucleation, when the embryo appears near an initially existing defect, the equilibrium size of the embryo has already been found. [265,272] The phenomenon is thought to occur as a result of the elastic interaction between the shape strain of the embryo and the stress field of the initial defect. In the case under consideration, there is a strong elastic interaction between the mobile defects describing the front of the growing embryo and the immobile defects located at the grain boundary. In fact, when the distance d between the mobile disclination dipole and immobile grain boundary disclination configuration is of the same order as the dipole arm $2a$ (i.e., $\tilde{d} < 10$), the growth of the embryo is mainly determined by the elastic term ΔE (see Figure 5.11(a)), which will be further discussed below.
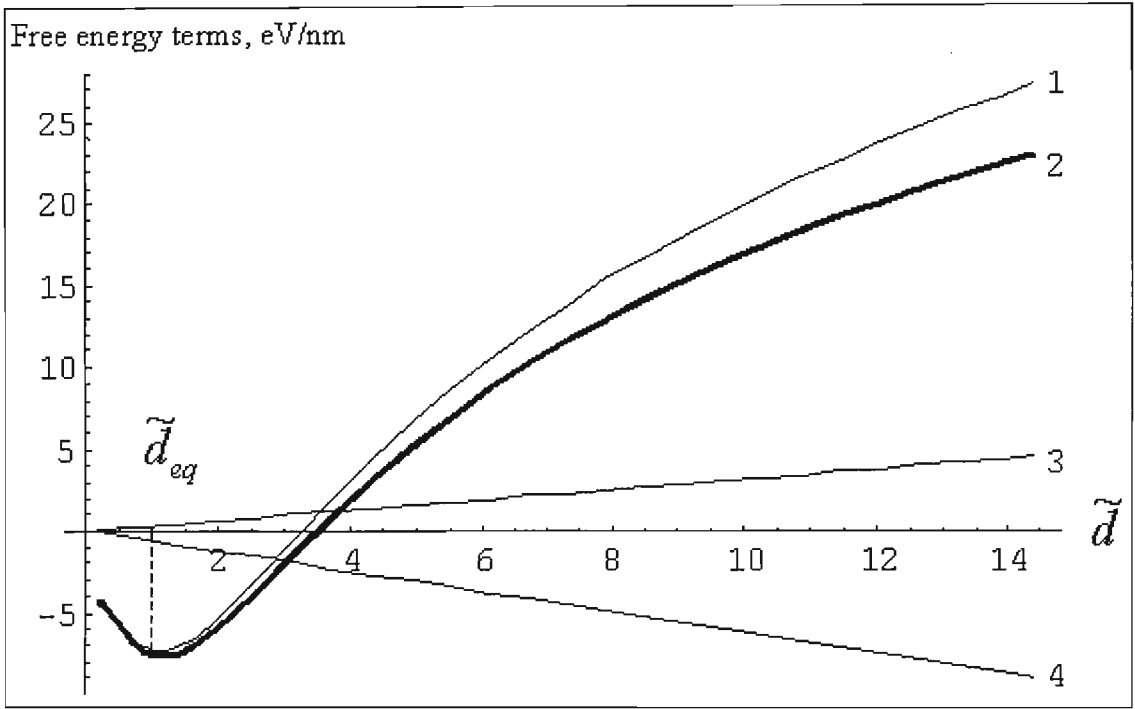
Figure 5. 11(a): Different terms of the total free energy gain ΔW vs. normalised embryo size for small values of $\tilde{d}$
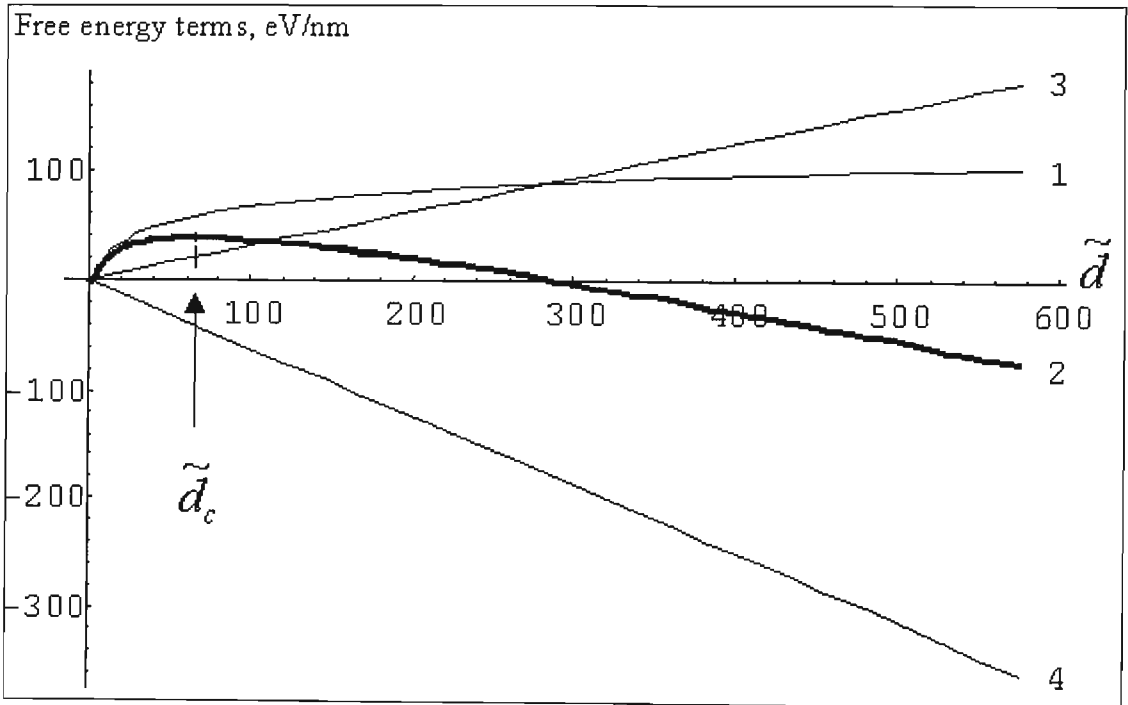
Figure 5. 11(b): Different terms of the total energy gain ΔW vs. the normalised embryo size, for large values of $\tilde{d}$

For larger embryo sizes (i.e., $\widetilde{d} > 10$), the total free energy gain ΔW increases, achieves its maximum value at $\widetilde{d} = \widetilde{d}_c$ which may be considered as a standard critical size of the martensitic embryo, and then decreases (Figure 5.11(b)). This part of the curve $\Delta W(\widetilde{d})$ is typical of standard thermodynamic theories of phase transformations. The elastic term ΔE remains practically constant here and the growth of the embryo is mainly determined by the other two terms, the free interface and chemical energies.

5.4.1.2 Contributions to the elastic energy gain ΔE

To better understand the behaviour of the elastic energy term ΔE, consider the dependence of its components on $\widetilde{d}$. They are represented in Figure 5.12, where:

> curve 1 corresponds to the difference $(E^{int}_{\Omega/2-\omega} - E^{int}_{\Omega-\omega})$ in energies of $\Omega/2$-dipoles-ω-dipole elastic interaction ($E^{int}_{\Omega/2-\omega}$ is given by eqn. 5.17) and Ω-dipole-ω-dipole elastic interaction ($E^{int}_{\Omega-\omega}$ is given by eqn. 5.9),

> curve 2 corresponds to the total elastic energy of screw-component Shockley dislocations E^{el}_{scr} which is given by (eqn. 5.22),

> curve 3 corresponds to the total elastic energy gain ΔE given by (eqn. 5.26),

> curve 4 corresponds to the total elastic energy of virtual dislocations E_v given by (eqn. 5.21),

> curve 5 corresponds to the difference $(E^c_{scr} + 2E^c_{\Omega/2} - E^c_\Omega)$ in sum core energies of all dislocations after and before embryo generation (E^c_{scr} is given by eqn. 5.24, $E^c_{\Omega/2}$ by eqn. 5.18, and E^c_Ω by eqn. 5.10), and

> curve 6 corresponds to the difference $(2E^s_{\Omega/2} + E^{int}_{\Omega/2-\Omega/2} - E^s_\Omega)$ in the total elastic energies of $\Omega/2$-disclinations and Ω-disclinations ($2E^s_{\Omega/2}$ is given by eqn. 5.13, $E^{int}_{\Omega/2-\Omega/2}$ by eqn. 5.16, and E^s_Ω by eqn. 5.5).

The behaviour of curve 1 is indicative of the fact that the dipole-dipole elastic interaction increases with the distance between the disclination dipoles when their strengths have opposite signs. The contribution of screw-component Shockley dislocations (curve 2) is obviously positive but a few times smaller than that of the previous term. The energy of virtual dislocations (curve 4) is also positive, but its value is much smaller than other contributions to ΔE. The change in sum core energy (curve 5) is definitely negative and does not depend on $\widetilde{d}$. It is also quite small in comparison with the terms shown by curves 1, 2 and 6. Curve 6

illustrates the energy gain due to the split of the initial dipole of Ω-disclinations into two dipoles of $\Omega/2$-disclinations. It is negative because such a split of higher-strength disclinations into some lower-strength disclinations is commonly an energetically favourable process (see e.g., [271, 273-277]). This energetic gain causes the negative values of ΔE at small $\tilde{d}$ as well as the existence of the equilibrium embryo size $\tilde{d}_{eq}$.
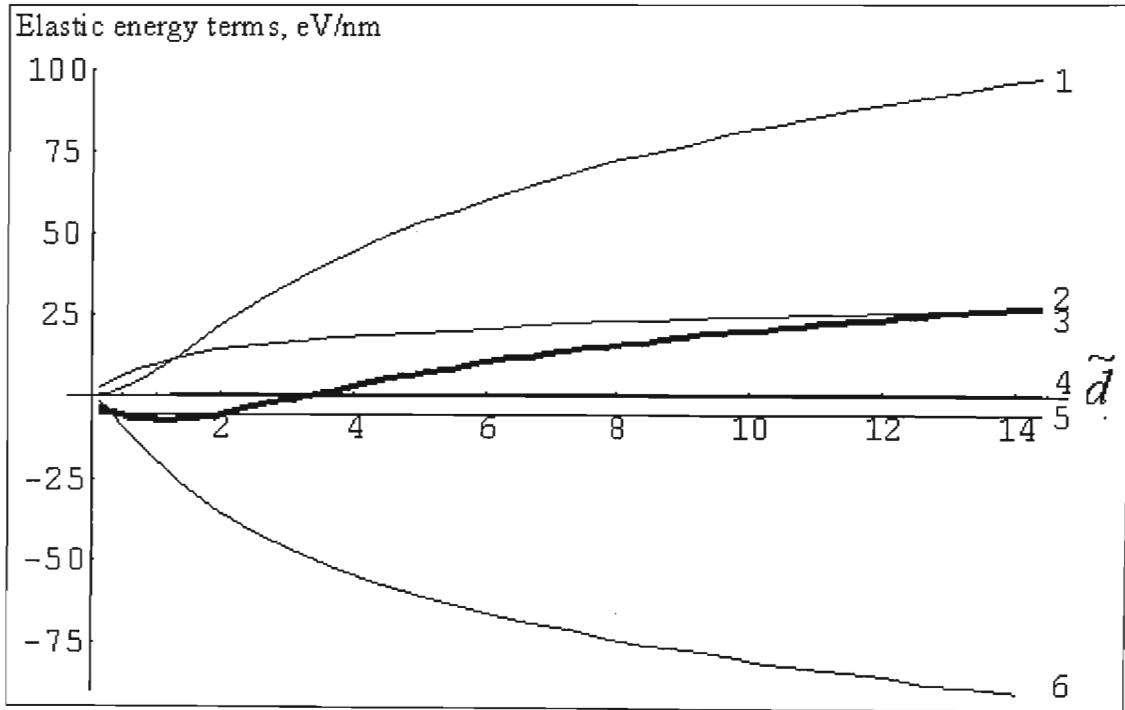
Figure 5.12(a): Different terms of the elastic energy gain ΔE vs. the normalised embryo size, for small values of $\tilde{d}$
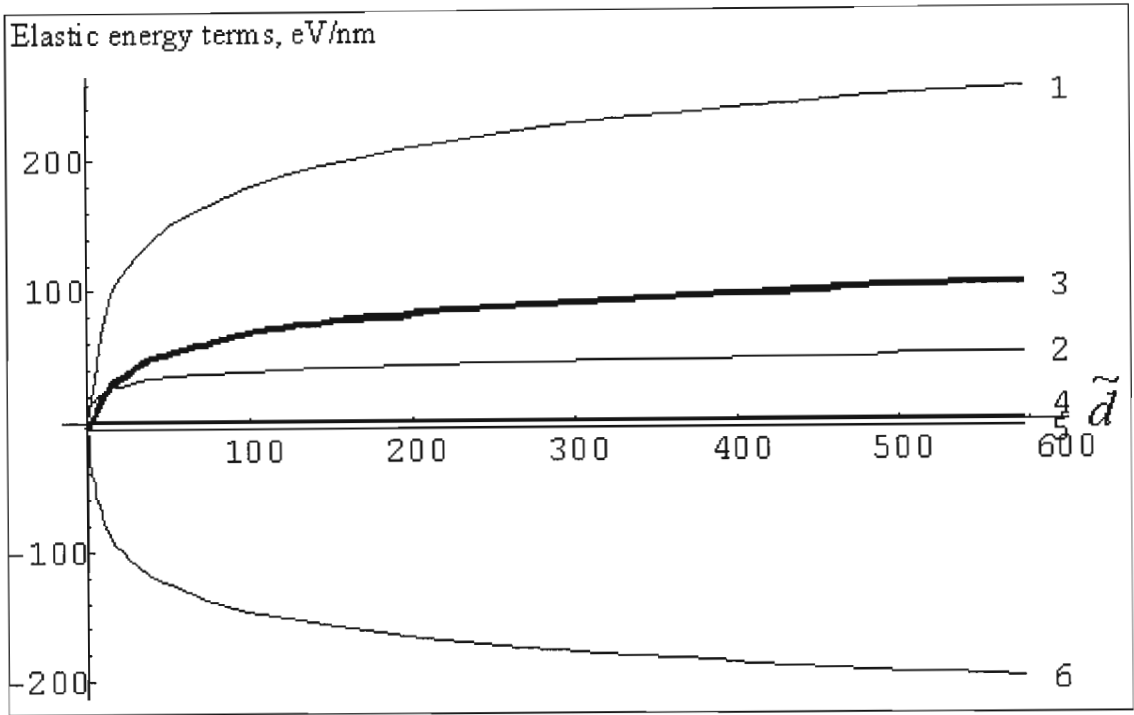
Figure 5. 12(b): Different terms of the elastic energy gain ΔE vs. the normalised embryo size, for large values of $\widetilde{d}$

5.4.1.3 Effect of grain-boundary misorientation ω on the elastic energy gain ΔE

Among the above contributions to the elastic energy gain ΔE, one can see that only the term $(E^{int}_{\Omega/2-\omega} - E^{int}_{\Omega-\omega})$ described by curve 1 depends on parameters of the initial defect structure where the martensitic embryo is generated. The most important parameter of the initial low-angle tilt boundary under consideration is the misorientation angle ω, which is introduced in the model as the strength of ω-disclinations (see Figure 5.10). In fact, the value of ω controls the interaction between the immobile ("large") dipole of ω-disclinations and mobile ("small") dipole of $\Omega/2$-disclinations. Thus, this interaction gives the most powerful contribution (curve 1 in Figure 5.12(b)) to ΔE at large $\widetilde{d}$. The influence of ω on the dependence $\Delta E(\widetilde{d})$ is illustrated in Figure 5.13, wherein for

➢ curve 1, ω =0
➢ curve 2, ω=0.02
➢ curve 3, ω=0.04
➢ curve 4, ω=0.06
➢ curve 5, ω=0.08
➢ curve 6, ω=0.1
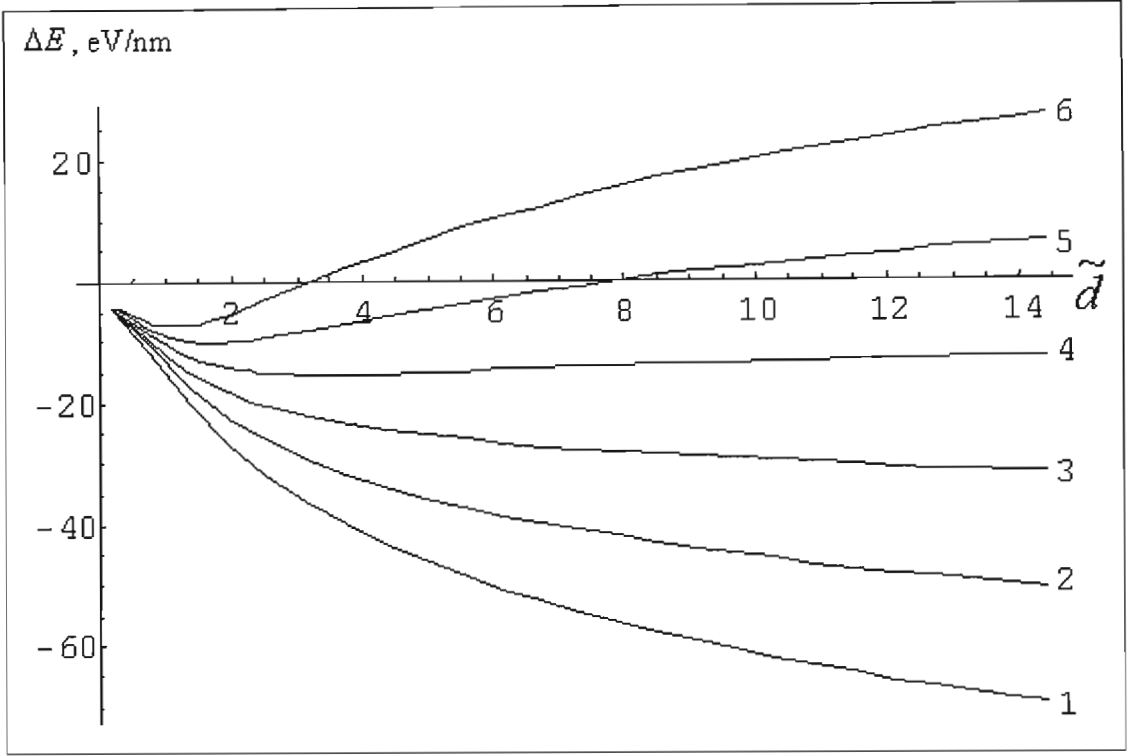
Figure 5. 13(a): The elastic energy gain ΔE vs. the normalised embryo size $\tilde{d}$ for τ=0 and different values of grain-boundary misorientation for small values of $\tilde{d}$

When ω is small ($\omega \leq 0.04$), ΔE is negative and decreases with increasing $\tilde{d}$. When ω is large ($\omega > 0.06$), ΔE is negative for small $\tilde{d}$, achieves its minimum value and increases after becoming positive as $\tilde{d}$ increases. Thus, there exists a critical misorientation (disclination strength) $\omega_c \approx 0.05$, which separates these two different behaviours of $\Delta E(\tilde{d})$.
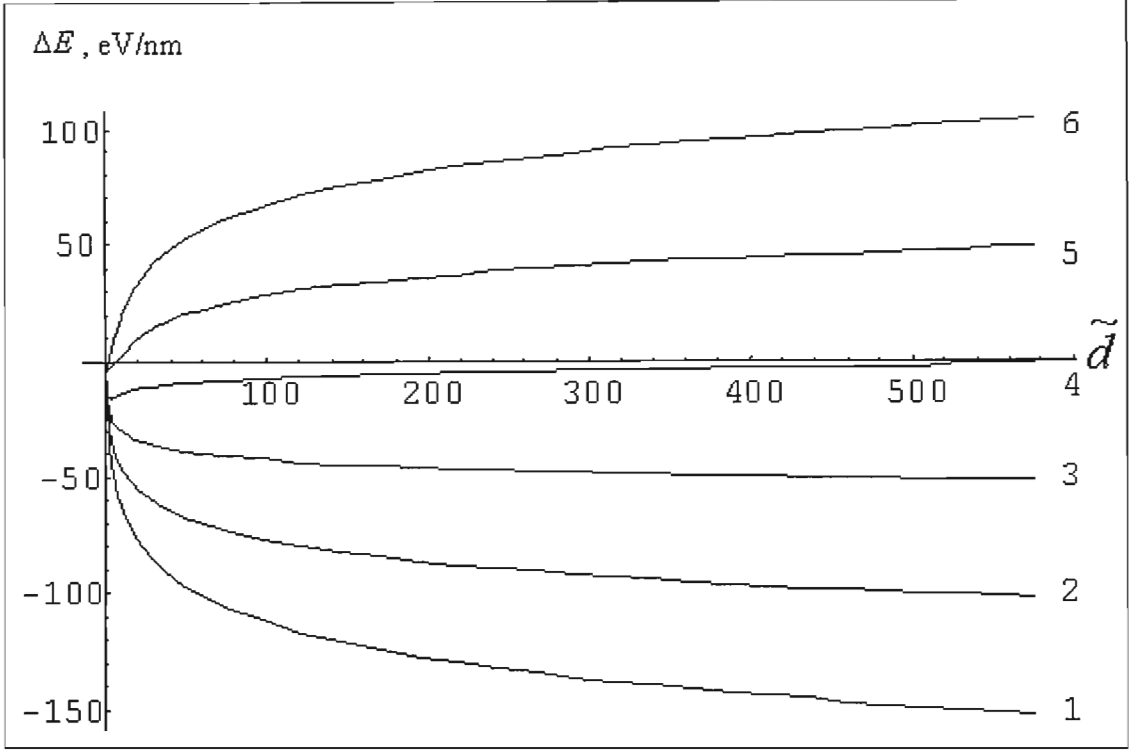
Figure 5. 13(b): The elastic energy gain ΔE vs. the normalised embryo size $\tilde{d}$ for τ=0 and different values of grain-boundary misorientation for large values of $\tilde{d}$

One can also estimate ω_c analytically. For this purpose, let us consider an asymptotic formula for $\Delta E(\tilde{d})$ when $\tilde{d} \gg 1$. In this limiting case, eqn. 5.26 is transformed as follows

$$\frac{\Delta E(\tilde{d} \gg 1)}{4Da^2} \approx -\frac{\Omega^2}{4} + \Omega\omega\left\{\tilde{A}\left[1 - \ln\left(\tilde{A}^2 - \frac{1}{4}\right)\right] - \left(\tilde{A}^2 + \frac{1}{4}\right)\ln\frac{2\tilde{A}+1}{2\tilde{A}-1}\right\} + 5\varepsilon_{yy}^2 + (1-\nu)\frac{b_s^2}{l^2}\left(3 + \frac{l}{a}\right)$$

$$+ \frac{\Omega}{2}\frac{b_e - b}{a} + 2\left\{-\frac{\Omega^2}{4} + \Omega\omega\tilde{A} + \varepsilon_{yy}^2 + (1-\nu)\frac{b_s^2}{l^2}\right\}\ln\tilde{d} - \frac{\Omega\tau}{D}\tilde{d},$$

$$(5.27)$$

where the denotation $\tilde{A} = A/2a$ is used.

When $\tau = 0$ and $\tilde{d} \to \infty$, eqn. 5.27 results in

$$\frac{\Delta E(\tilde{d} \to \infty)}{4Da^2} \approx 2\left\{-\frac{\Omega^2}{4} + \Omega\omega\tilde{A} + \varepsilon_{yy}^2 + (1-\nu)\frac{b_s^2}{l^2}\right\}\ln\tilde{d}. \qquad (5.28)$$

Then the equation $\Delta E(\tilde{d} \to \infty) = 0$ gives the following critical misorientation

$$\omega_c = \frac{1}{\tilde{A}\Omega}\left(\frac{\Omega^2}{4} - \varepsilon_{yy}^2 - (1-\nu)\frac{b_s^2}{l^2}\right). \qquad (5.29)$$

97

It has the sense of the maximum misorientation (or strength of the "large" disclination dipole) at which the "small" disclination dipole can split into two parts, where the distance $\tilde{d}$ between them may be infinite. When $\omega < \omega_c$, the split process is energetically favourable for any $\tilde{d}$; when $\omega > \omega_c$, it is energetically favourable for small $\tilde{d}$ only. In the first case, the grain boundary is not strong enough to prevent a spontaneous split of the "small" disclination dipole, while in the second case, it is. For the following values of parameters, $\tilde{A} = 3/2$, $\Omega = 1/\sqrt{6}$, $\varepsilon_{yy} = 0.01$, $\nu = 1/3$, $b_s = p/\left(2\sqrt{6}\right)$, and $l = p\sqrt{3}$, Eq.28 gives the estimate $\omega_c \approx 0.053$ which elucidates the previous conclusion from Figure 5.13.

5.4.2   The case of $\tau \neq 0$

We now consider the case where the external shear stress is non-zero, and again (where relevant) constant material data has been used from Olsen-Cohen work [194]

5.4.2.1 Effect of external shear stress in the total energy gain ΔW

Consider the effect of external shear stress τ on the total energy gain ΔW. In Figure 5.14, the curves $\Delta W(\tilde{d})$ are shown for the fixed temperature value $T = 200\,\text{K}$ and different values of τ. When $\tilde{d}$ is small enough ($\tilde{d} < 1$), the growth of the martensitic embryo is mainly controlled by elastic interaction of the ω - and $\Omega/2$ -disclination dipoles, and the effect of τ is not too strong (Figure 5.14 (a)). In the region of larger $\tilde{d}$, the influence of τ is very strong. In fact, the external stress τ controls the behaviour of the curve $\Delta W(\tilde{d})$ and greatly influences the characteristic sizes of the embryo, $\tilde{d}_{eq}$ and $\tilde{d}_c$. The latter effects will be discussed a little later.

Three different regimes of behaviour of $\Delta W(\tilde{d})$ can be separated out, depending on τ :

➤ Case (i): Small values of τ (here $\tau/\mu \approx 0...2\cdot10^{-3}$, curves 1 to 4). The function $\Delta W(\tilde{d})$ is negative for small and very large $\tilde{d}$, and positive for intermediate $\tilde{d}$; it achieves its minimal value at $\tilde{d} = \tilde{d}_{eq}$, and its maximal value at $\tilde{d} = \tilde{d}_c$. There exists an energy barrier $\Delta W(\tilde{d}_c)$ for the growing martensitic embryo. When τ increases, $\tilde{d}_{eq}$ increases while both $\tilde{d}_c$ and $\Delta W(\tilde{d}_c)$ decrease.

> Case (ii): Intermediate values of τ (here $\tau/\mu \approx 3 \cdot 10^{-3} \ldots 5 \cdot 10^{-3}$, curves 5 and 6). The function $\Delta W(\widetilde{d})$ is negative for any $\widetilde{d}$; other features are as in case (i).

> Case (iii): Large values of τ (here $\tau/\mu \geq 7 \cdot 10^{-3}$, curves 7 and 8). The function $\Delta W(\widetilde{d})$ is negative for any $\widetilde{d}$; no extreme values or energetic barriers exist for the growing embryo.

> From the physical point of view, the boundary between regimes (ii) and (iii) is of special interest because it separates the thermo-activated regimes (i) and (ii) of embryo development from the athermal one (iii). One can introduce the corresponding critical shear stress τ_c which is estimated from figure 5.14 as $\tau_c \approx 7 \cdot 10^{-3} \mu$, that for $\mu = 74$ GPa gives ≈ 518 MPa. τ_c will be discussed further in more detail below.
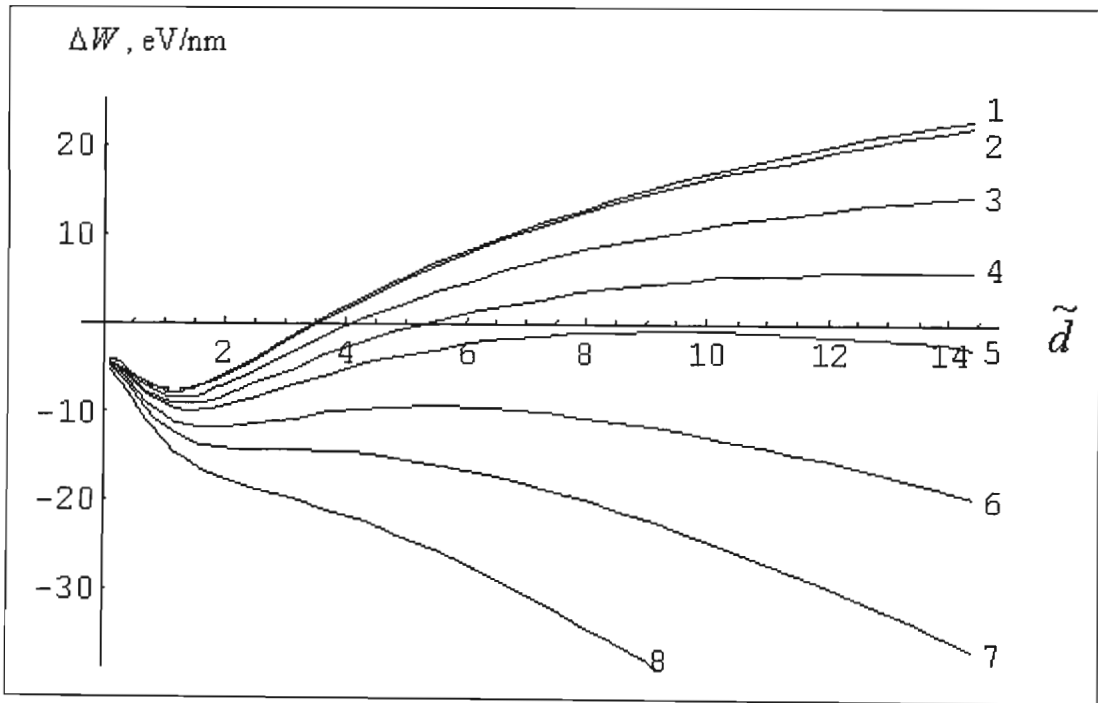
Figure 5. 14(a): The total free energy gain ΔW vs. the normalised embryo size $\widetilde{d}$ for the temperature T=200K and different values of external shear stress, for small values of $\widetilde{d}$

99
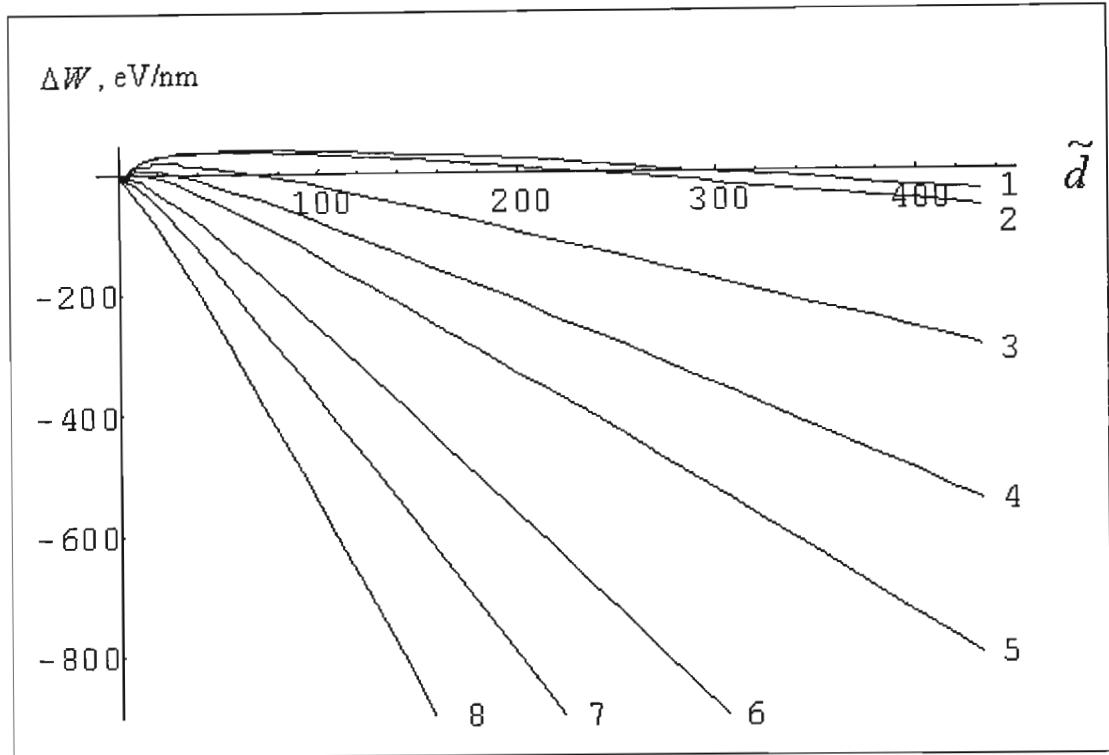
Figure 5. 14(b): The total free energy gain ΔW vs. the normalised embryo size $\tilde{d}$ for the temperature T=200K and different values of external shear stress, for large values of $\tilde{d}$

For Figures 5.14 (a) and (b) curves 1 to 8 have the following values of τ/μ:

- Curve 1, $\tau/\mu=0$
- Curve 2, $\tau/\mu=10^{-4}$
- Curve 3, $\tau/\mu=10^{-3}$
- Curve 4, $\tau/\mu=2 \times 10^{-3}$
- Curve 5, $\tau/\mu=3 \times 10^{-3}$
- Curve 6, $\tau/\mu=5 \times 10^{-3}$
- Curve 7, $\tau/\mu=7 \times 10^{-3}$
- Curve 8, $\tau/\mu=10^{-2}$

5.4.2.2 Effect of temperature on the total energy gain ΔW

Evidently, the model under consideration is highly sensitive to the temperature. To study the temperature effect, one can use data from [194] where the relations of the chemical free energy gain ΔG and free interface energy γ with temperature have been discussed in detail. In doing so, seven different values of temperature and their estimated corresponding values of ΔG and γ are shown in Table 5.4 below and used to plot curves 1 to 7.

Table 5.3: Values for free energy gain, and interface free energy, varying with temperature

Curve	Temperature (K)	ΔG (J/mole)	γ, (J/m^2)
1	100	-200	0.0110
2	200	-126	0.0100
3	250	-25	0.0095
4	275	0	0.0092
5	300	50	0.0090
6	350	200	0.0085
7	400	350	0.0080

Introducing the above values into (eqn. 5.3), the corresponding curves $\Delta W(\tilde{d})$ have been numerically constructed for different values of τ and T (Figure 5.15).

Figure 5. 15a(i): The total free energy gain ΔW vs. the normalised embryo size $\tilde{d}$ for external shear stress $= 10^{-4}$ and temperature varying as shown in table 5.4, for small values of $\tilde{d}$.

Figure 5. 15a(ii): The total free energy gain ΔW vs. the normalised embryo size $\widetilde{d}$ for external shear stress $= 10^{-4}$ and temperature varying as shown in table 5.4, for large values of $\widetilde{d}$.
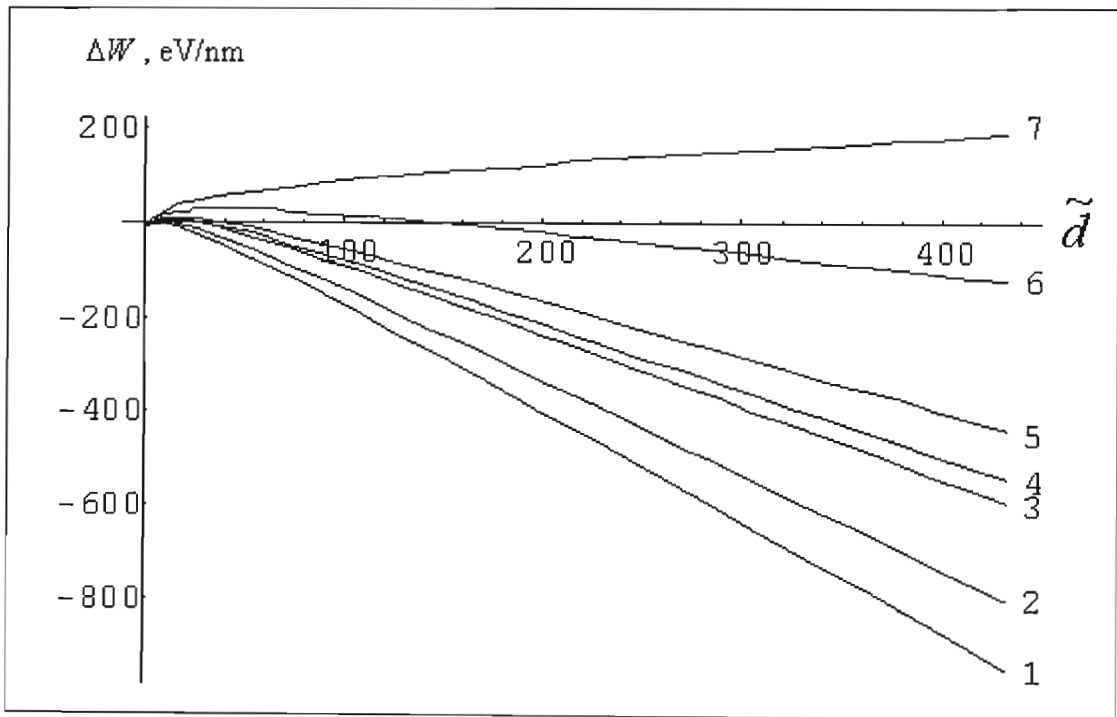
Figure 5. 15b(i): The total free energy gain ΔW vs. the normalised embryo size $\widetilde{d}$ for external shear stress $= 3 \times 10^{-3}$ and temperature varying as shown in table 5.4, for small values of $\widetilde{d}$.
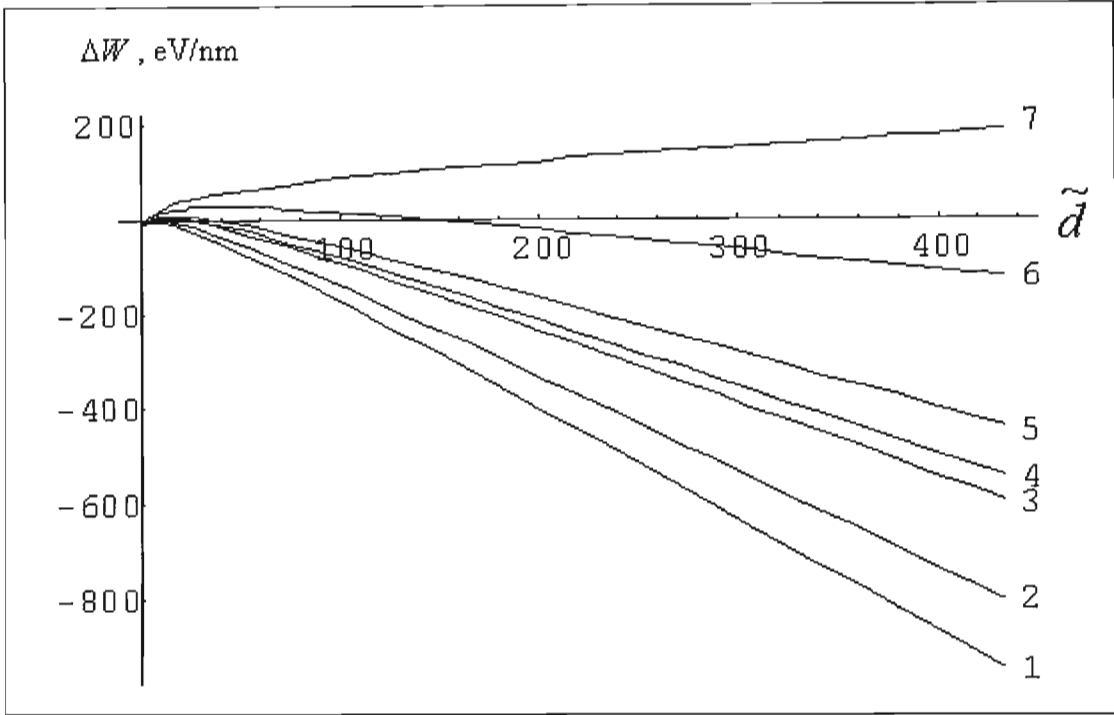
Figure 5. 15b(ii): The total free energy gain ΔW vs. the normalised embryo size $\tilde{d}$ for external shear stress $= 3 \times 10^{-3}$ and temperature varying as shown in table 5.4, for large values of $\tilde{d}$.
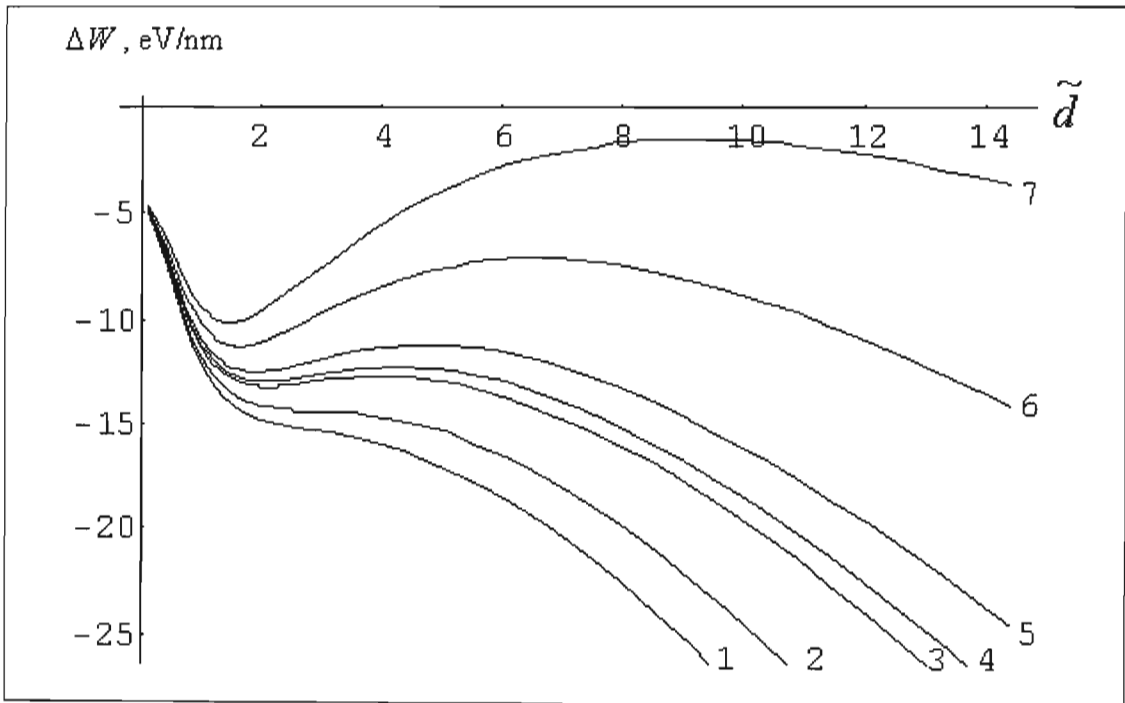
Figure 5. 15c(i): The total free energy gain ΔW vs. the normalised embryo size $\tilde{d}$ for external shear stress $= 7 \times 10^{-3}$ and temperature varying as shown in table 5.4, for small values of $\tilde{d}$.
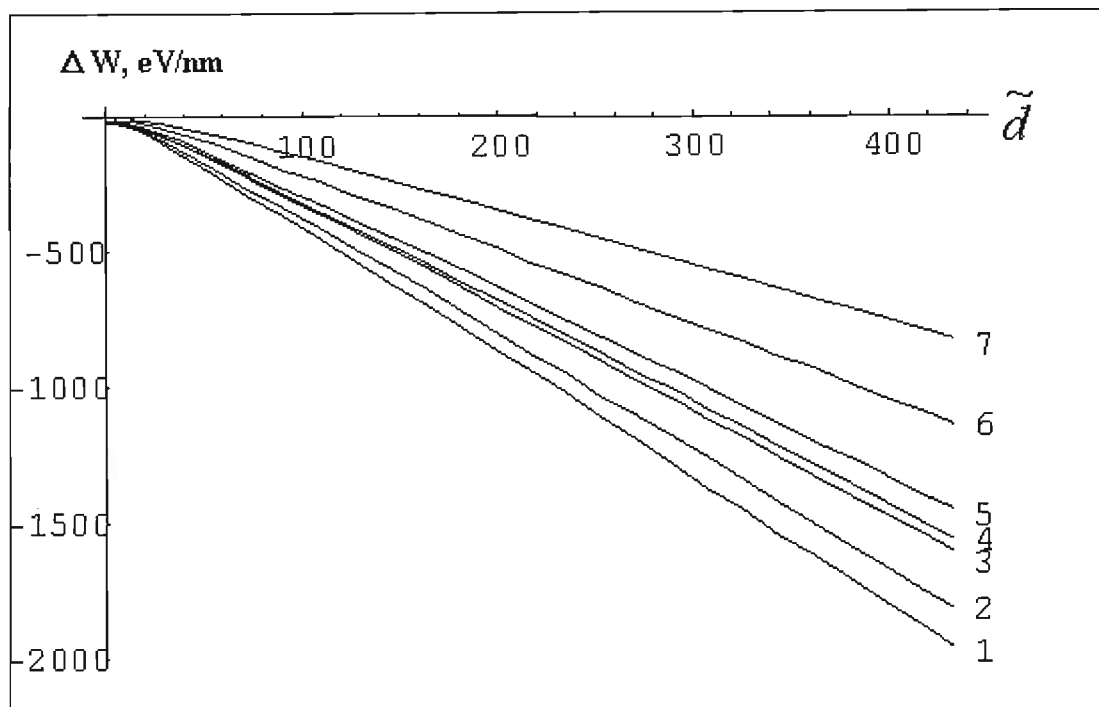
Figure 5.15c(ii): The total free energy gain ΔW vs. the normalised embryo size $\tilde{d}$ for external shear stress $= 7 \times 10^{-3}$ and temperature varying as shown in table 5.4, for large values of $\tilde{d}$.
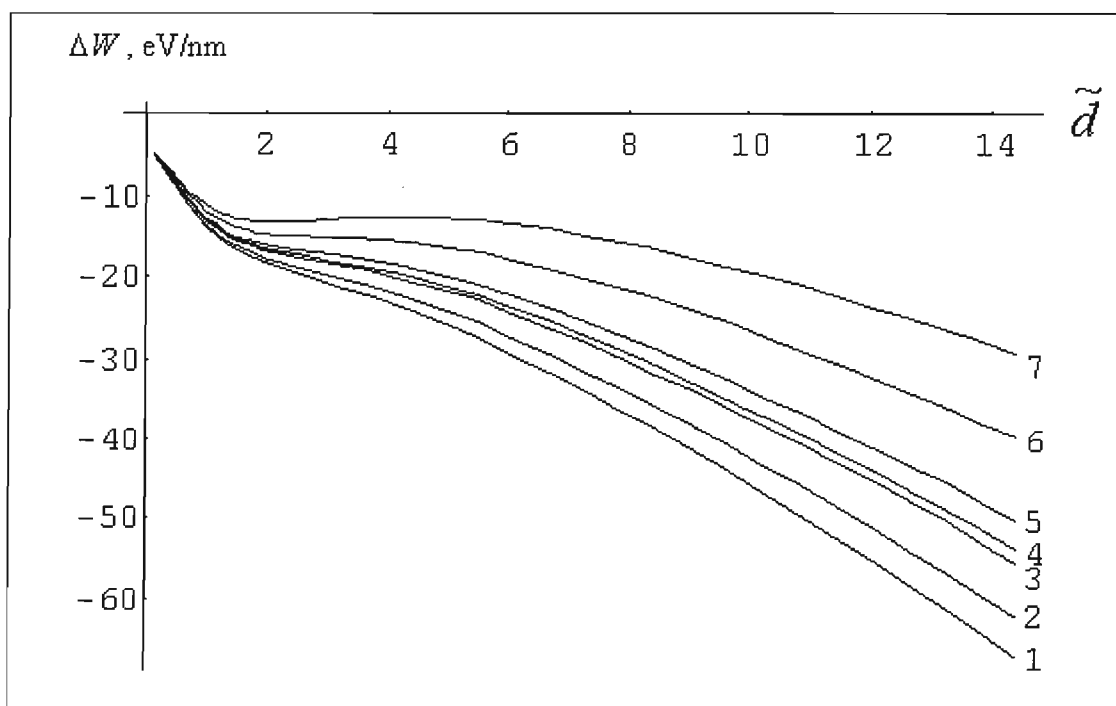
Figure 5. 15d(i): The total free energy gain ΔW vs. the normalised embryo size $\tilde{d}$ for external shear stress $= 10^{-2}$ and temperature varying as shown in table 5.4, for small values of $\tilde{d}$.
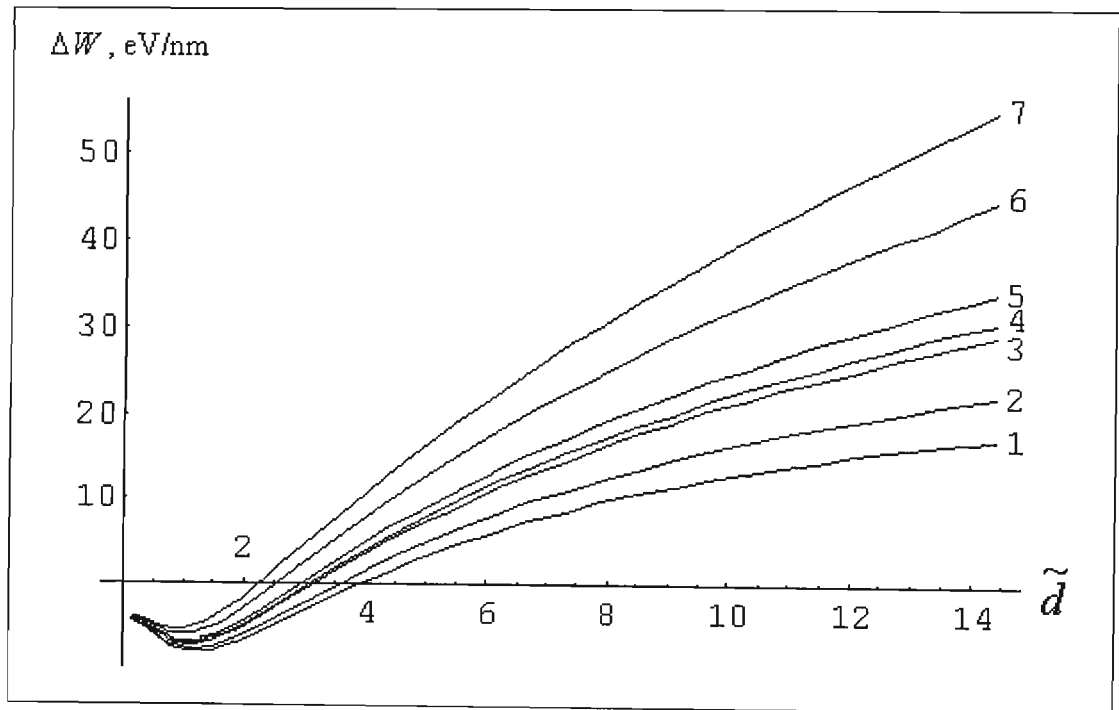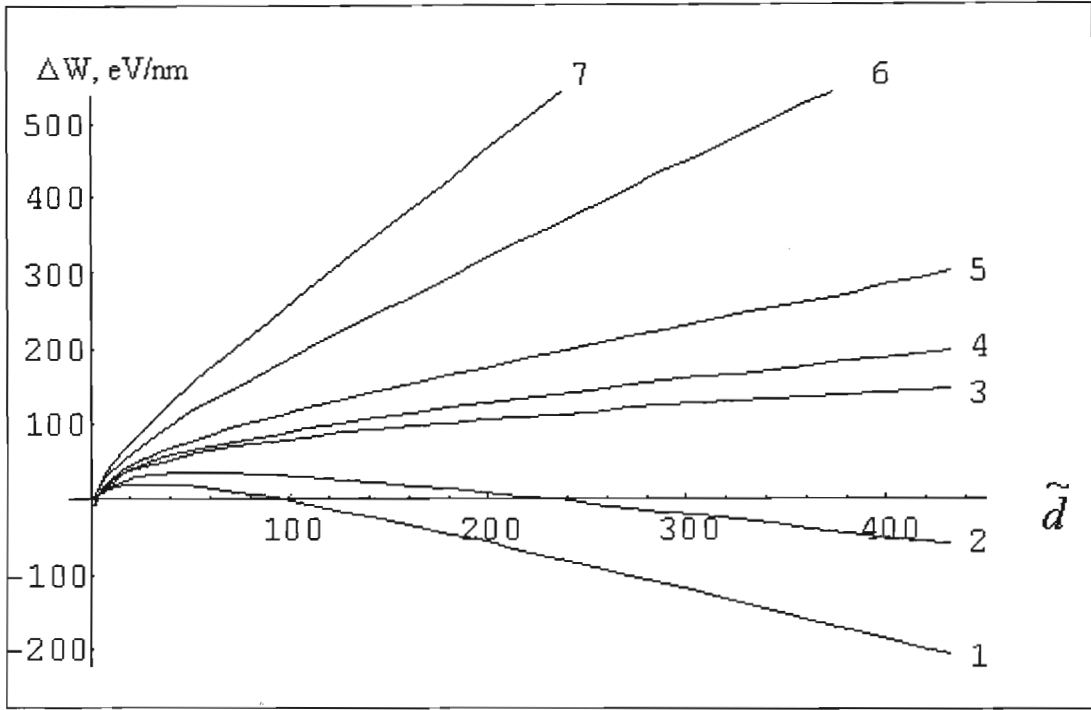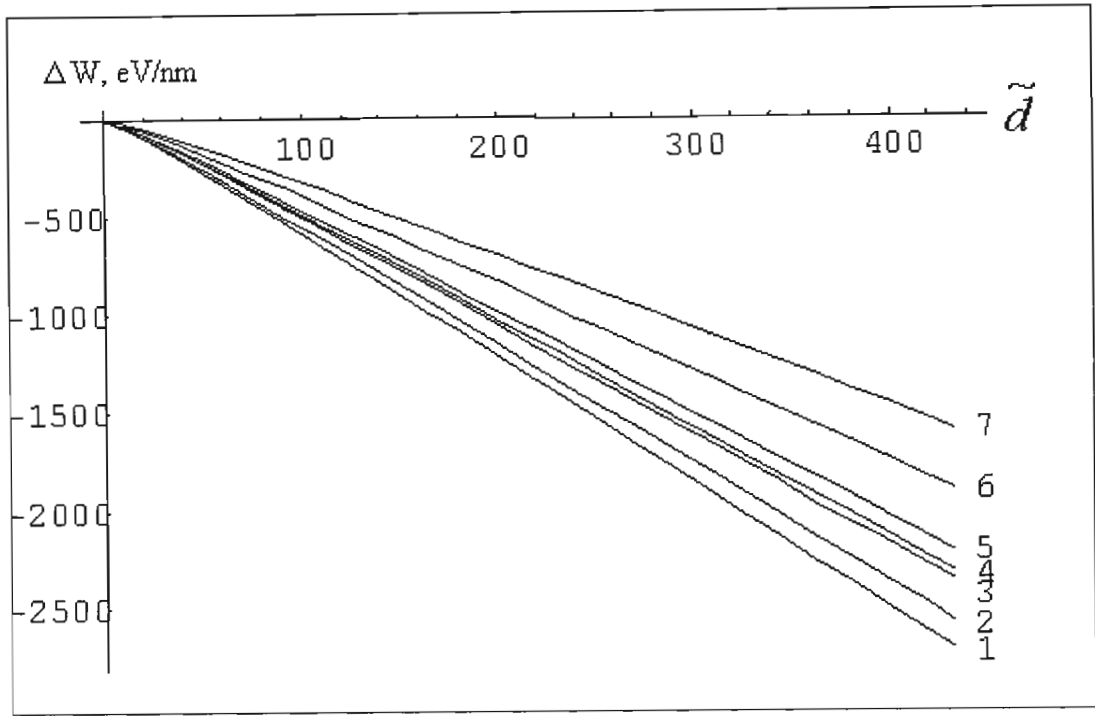
Figure 5. 15d(ii): The total free energy gain ΔW vs. the normalised embryo size $\widetilde{d}$ for external shear stress $= 10^{-2}$ and temperature varying as shown in table 5.4, for large values of $\widetilde{d}$.

It is seen from Figure 5.15 that the initial stages of the embryo growth, when $\widetilde{d} \leq 1$, are not too sensitive to either the effects of temperature T or external stress τ (see the top plots in Figure 5.15). In fact, these initial stages are totally controlled by the parameters of the initial defect structure of that grain boundary region where embryo generation takes place.

However, the further stages of embryo development, when $\widetilde{d} > 1$, are strongly affected by T and τ. For example, the increasing of T leads to a new behaviour of the function $\Delta W(\widetilde{d})$ shown by curves 3 to 7 in Figure 5.15(a) or by curve 7 in Figure 5.15(b), which is qualitatively different from the aforementioned ones. Here, ΔW becomes positive at some $\widetilde{d}$ and increases further as $\widetilde{d}$ increases. This means the martensitic embryo can only grow in size until $\widetilde{d} = \widetilde{d}_{eq}$, stopping thereafter. Such behaviour is typical for the case of relatively high T and low τ. In other cases, when T is lower and/or τ is higher, Figure 5.15 demonstrates all the other aforementioned behaviours (i), (ii), and (iii). It is worthy to note that for any temperature T from the Table 5.4, one can find an appropriate τ_c to make the embryo grow without any energy barriers (Figure 5.15 (d)).

5.4.2.3 The critical external shear stress τ_c

The critical external shear stress τ_c will be the minimum that provides the elimination of extreme points on the curve $\Delta W(\tilde{d})$, thus stimulating the athermal generation of a martensitic embryo. Mathematically, this means that the partial derivative $\partial \Delta W / \partial \tilde{d} = 0$ at the inflexion point $\tilde{d} = \tilde{d}_{in}$ (where $\tilde{d}_{eq} < \tilde{d}_{in} < \tilde{d}_c$) when $\tau = \tau_c$. Generally speaking, this partial derivative has the sense of a thermodynamic driving force

$$F(\tilde{d}) = -\frac{\partial \Delta W}{\partial \tilde{d}}. \tag{5.30}$$

The behaviour of the curve $F(\tilde{d})$ is illustrated in Figure 5.16 for $T = 200\,\mathrm{K}$ and $\tau = 3 \cdot 10^{-3} \mu$. When $F > 0$, the growth of a martensitic embryo is energetically favourable, and when $F < 0$, it is not. The point $\tilde{d} = \tilde{d}_{eq}$ where $F = 0$ and $\partial F / \partial \tilde{d} < 0$, is the stable equilibrium point. The point $\tilde{d} = \tilde{d}_c$ where $F = 0$ and $\partial F / \partial \tilde{d} > 0$, is the unstable equilibrium point. The point $\tilde{d} = \tilde{d}_{in}$ where $\partial F / \partial \tilde{d} = 0$ and $\partial^2 F / \partial \tilde{d}^2 > 0$, is the point of strongest negative driving force acting on the growing embryo. At $\tau = \tau_c$, it must be zero. A similar definition of τ_c was used in [265].
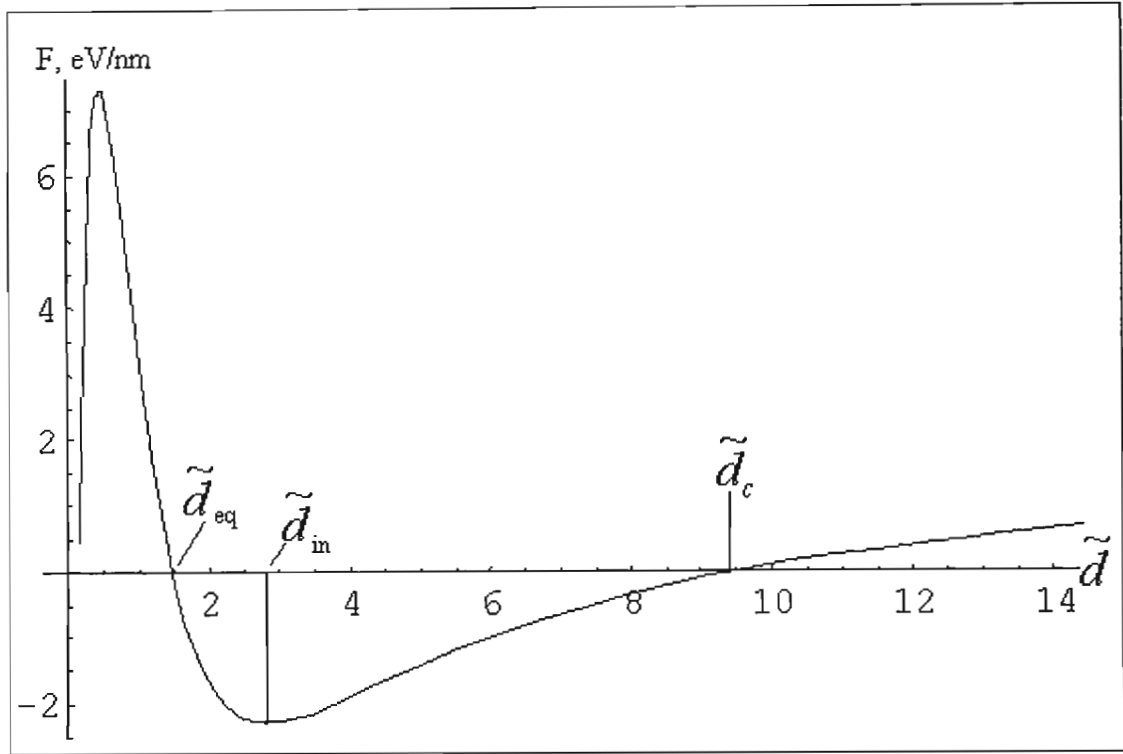
Figure 5. 16: Thermodynamic driving force F vs. normalised embryo size $\widetilde{d}$ for the external shear stress τ=3 x 10⁻³μ and temperature T = 200K. $\widetilde{d}_{eq}$, $\widetilde{d}_{in}$, $\widetilde{d}_{c}$ are the characteristic sizes of the martensitic embryo.

The τ dependencies of $F(\widetilde{d})$ are shown in Figure 5.17 for $T = 200\,\text{K}$ and different values of τ, and in Figure 5.18 for $\tau = 3\cdot10^{-3}\,\mu$ and different values of T. One can conclude from Figures 5.17 and 5.18 that the driving force F increases as τ increases and T decreases. It follows from Figure 5.17 that $\tau_c \approx 7\cdot10^{-3}\,\mu$ which is in agreement with the earlier estimate from Figure 5.14. The characteristic points $\widetilde{d} = \widetilde{d}_{eq}$ and $\widetilde{d} = \widetilde{d}_{c}$ are shifted with variation of τ and/or T. The embryo equilibrium size $\widetilde{d}_{eq}$ increases as τ increases and T decreases (Figure 5.19), in contrast to the embryo critical size $\widetilde{d}_{c}$ which decreases as τ increases and T decreases (Figure 5.20). Another useful observation from Figure 5.17 and 5.18 follows. For all values of τ and T, the characteristic point $\widetilde{d} = \widetilde{d}_{in}$ remains approximately the same, $\widetilde{d}_{in} \approx 2.81$. This observation can be used to estimate the values of τ_c analytically depending on other parameters of the model under consideration.
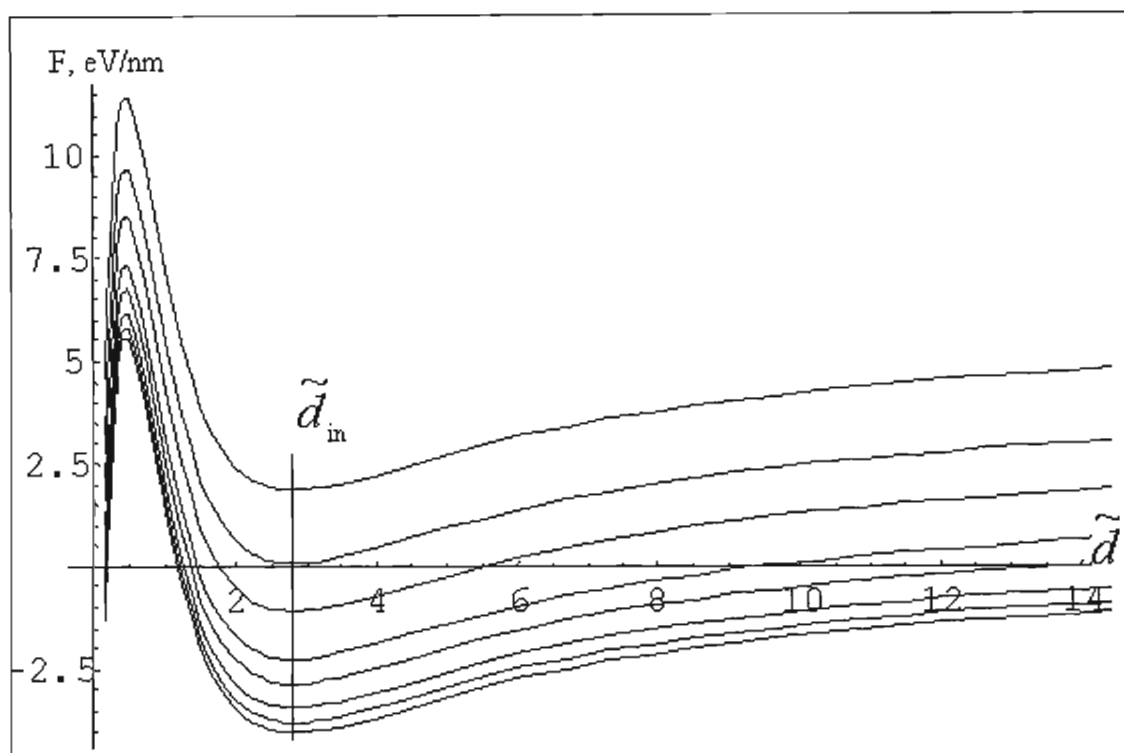
Figure 5. 17(a): Thermodynamic driving force vs. normalised embryo size $\tilde{d}$ for the temperature T = 200K and different values of external shear stress, for small values of $\tilde{d}$
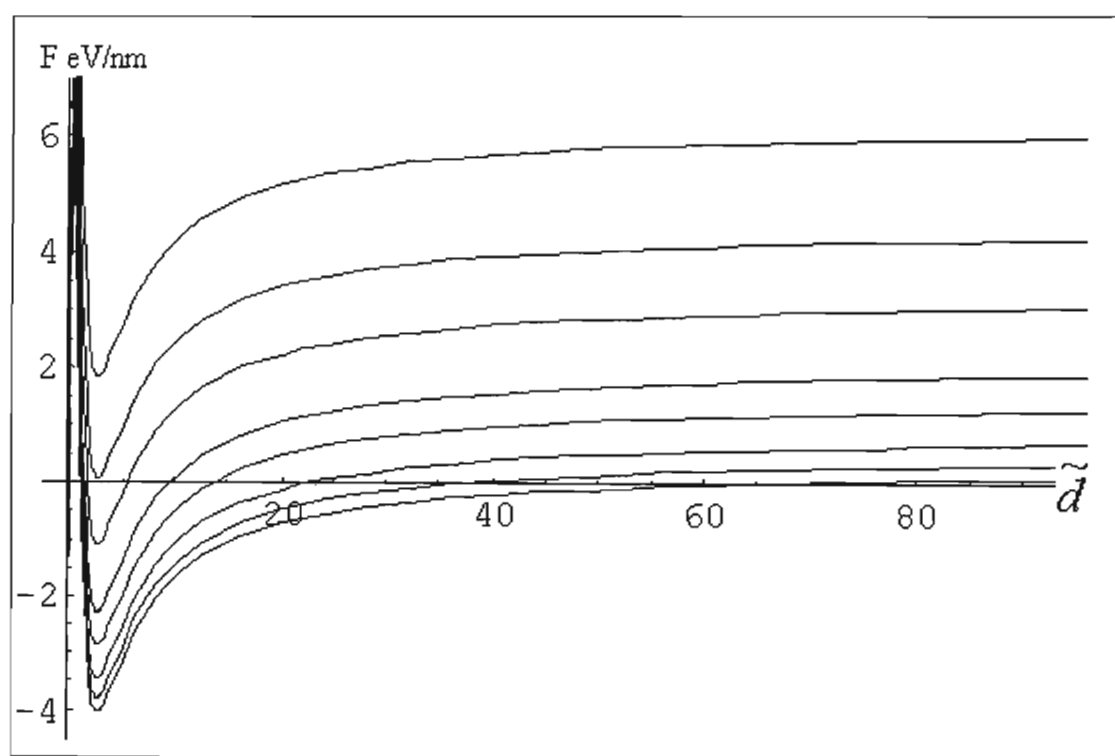
Figure 5. 17(b): Thermodynamic driving force vs. normalised embryo size $\tilde{d}$ for the temperature T = 200K and different values of external shear stress, for large values of $\tilde{d}$

The values of external shear stress τ/μ vary in Figures 5.17 (a) and (b) through 0, 10^{-4}, 10^{-3}, 2 x 10^{-3}, 3 x 10^{-3}, 5 x 10^{-3}, 7 x 10^{-3}, and 10^{-2}. The characteristic embryo size $\widetilde{d}_{in}$ is practically constant for any τ.
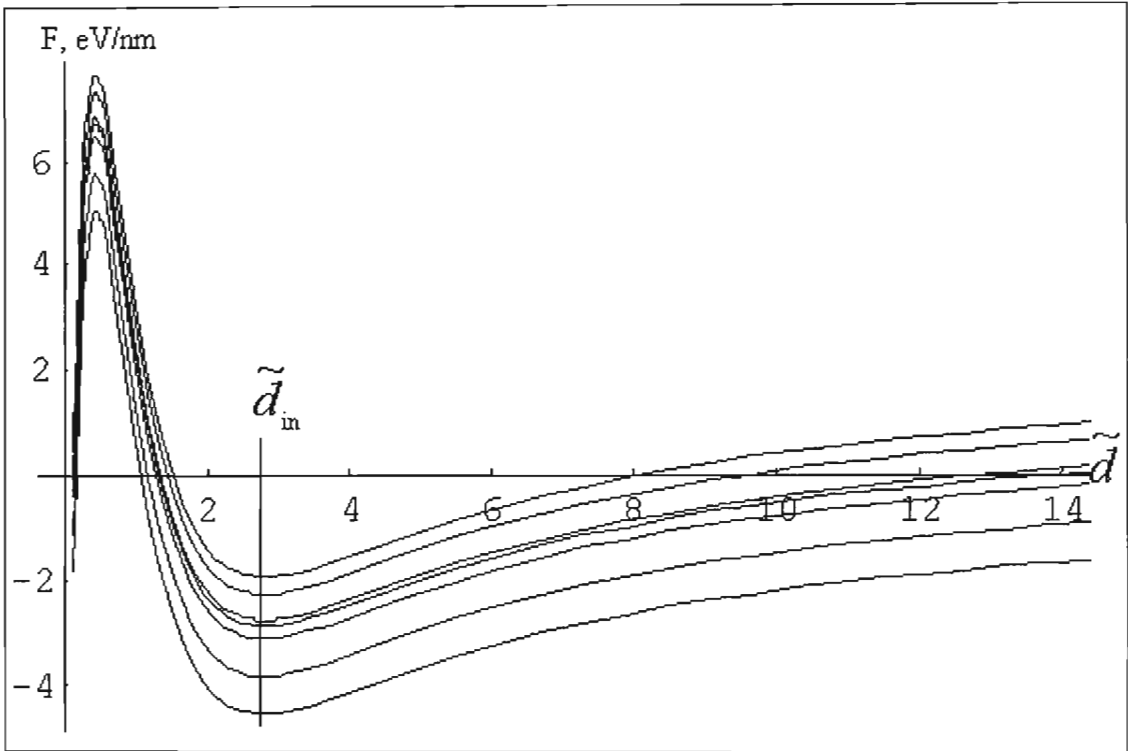
Figure 5. 18(a): Thermodynamic driving force F vs. the normalised embryo size $\widetilde{d}$ for the external shear stress τ=3 x $10^{-3}\mu$ and different values of temperature, for small values of $\widetilde{d}$

Temperature values vary from top to bottom through 100, 200, 250, 275, 300, 350, and 400K for the curves shown in Figure 5.18 (a) and (b).
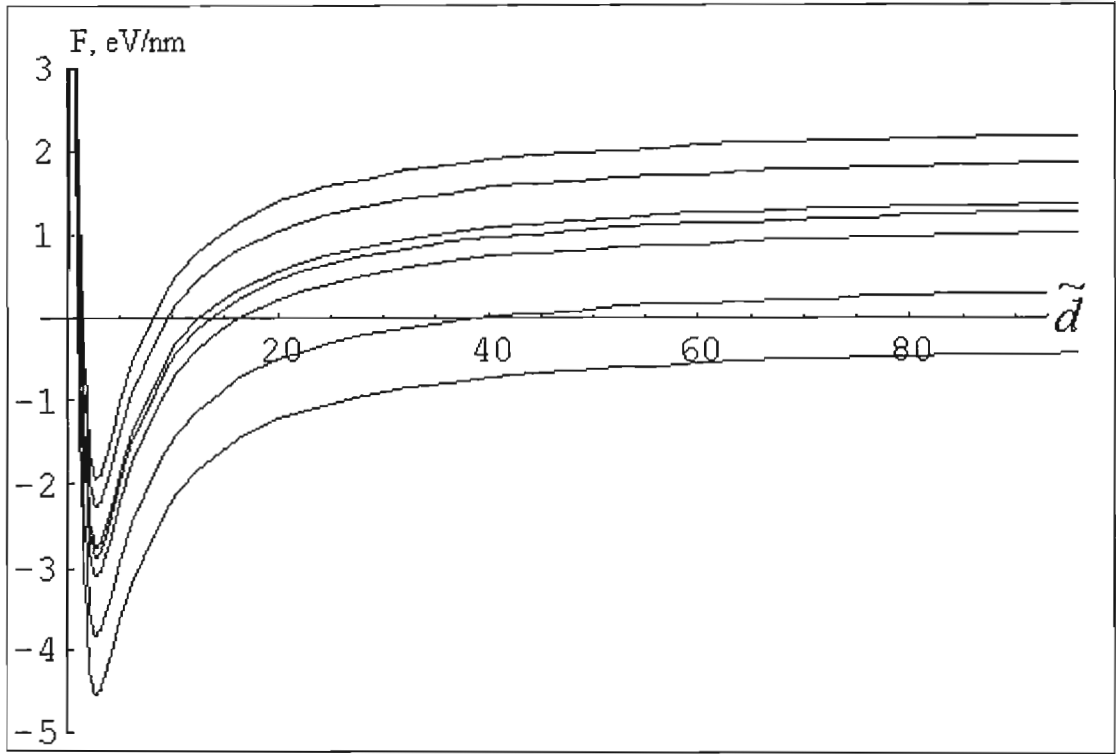
Figure 5. 18(b): Thermodynamic driving force F vs. the normalised embryo size $\tilde{d}$ for the external shear stress τ=3 x 10⁻³μ and different values of temperature, for small values of $\tilde{d}$
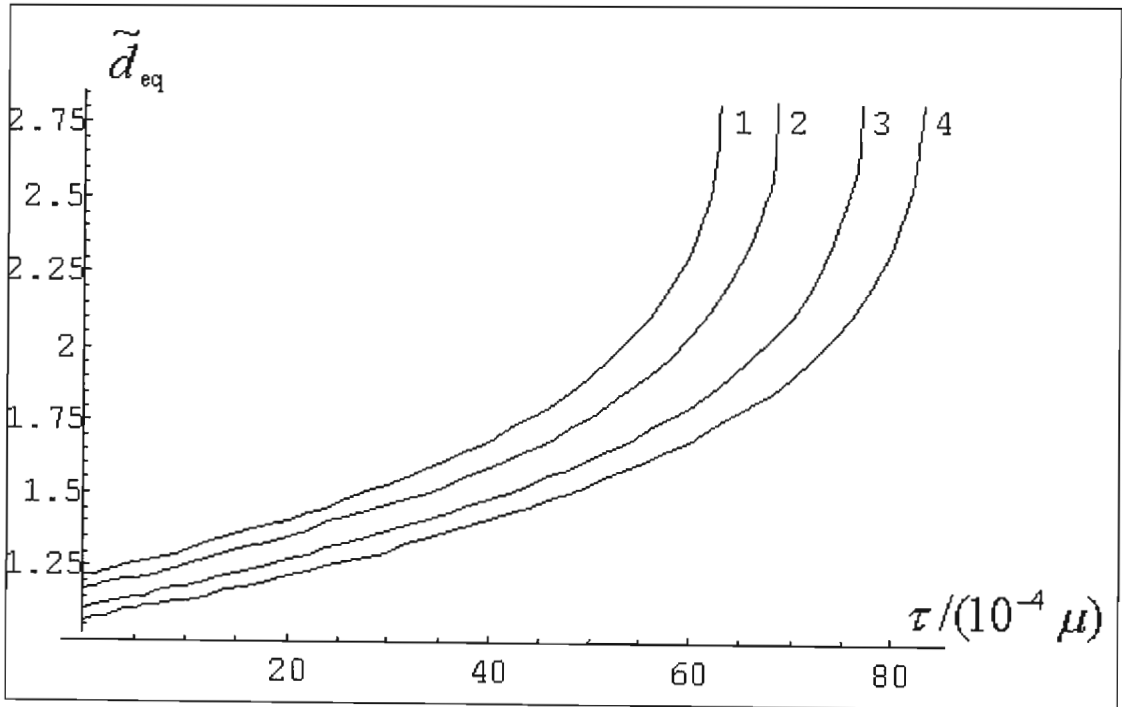
Figure 5. 19: The equilibrium embryo size $\tilde{d}_{eq}$ vs. the external shear stress τ for different values of temperature 100 (1), 200 (2), 250 (3), and 300K (4).
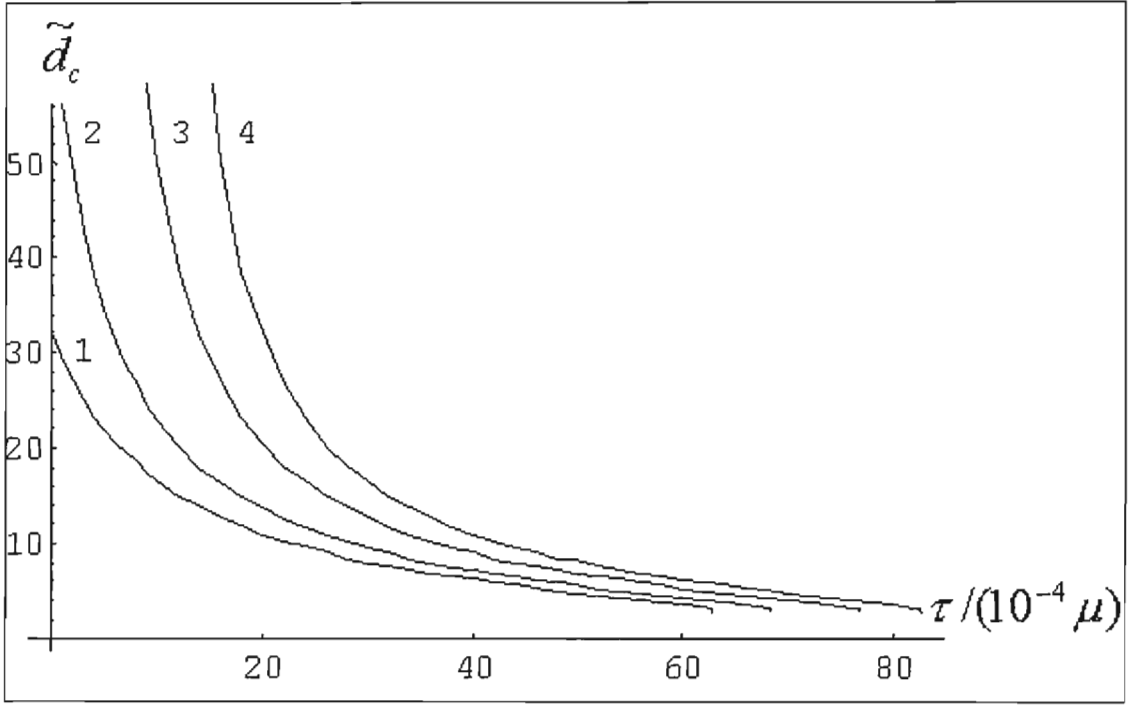
Figure 5. 20: The critical embryo size $\widetilde{d}_c$ vs. the external shear stress τ for different values of temperature T = 100 (1), 200 (2), 250 (3), and 300K (4)

The critical shear stress τ_c may be determined from the equation

$$F(\widetilde{d} = \widetilde{d}_{in}) = 0.$$

(5.31)

Substitution of eqn.5.3 with eqn. 5.26 into eqn. 5.30, and that latter into eqn. 5.31 leads to the following solution:

$$\tau_c \frac{\Omega}{2D} = \frac{\omega\Omega}{2}\widetilde{d}_{in} \ln\frac{4\widetilde{d}_{in}^2 + (2\widetilde{A}+1)^2}{4\widetilde{d}_{in}^2 + (2\widetilde{A}-1)^2} - \left(\frac{\Omega^2}{4} + 3\varepsilon_{yy}^2 + (1-v)\frac{b_s^2}{l^2}\right)\widetilde{d}_{in} \ln\frac{\widetilde{d}_{in}^2+1}{\widetilde{d}_{in}^2}$$
$$+ 2\left(2\varepsilon_{yy}^2 + (1-v)\frac{b_s^2}{l^2}\right)\cot^{-1}\widetilde{d}_{in} + \frac{n\rho\Delta G + 2\gamma}{2Da}.$$

(5.32)

It has been noted above that $\widetilde{d}_{in} \approx 2.81$ for any τ and T. Dependencies of τ_c on the characteristic parameters of the "large" disclination dipole, its normalised half-arm $\widetilde{A}$ ($= A/2a$) and strength ω, are shown in Figs.12 (for $\omega = 1/(4\sqrt{6})$) and 13 (for $\widetilde{A} = 3/2$), respectively, for different values of T listed in table 5.4.

111

Figure 5.21 demonstrates the non-linear dependence of τ_c on $\tilde{A}$. When $\tilde{A}$ is small enough ($\tilde{A} < 3$), the critical stress τ_c increases with $\tilde{A}$; when $\tilde{A}$ becomes larger, τ_c achieves its maximum value ($\tau_{c,\max}$ varies from $\approx 0.01\mu$ to $\approx 0.015\mu$ when T changes from 100 K to 400 K, respectively) and decreases with a further decrease in $\tilde{A}$. Moreover, τ_c is negative in the regions of small (< 1) and large ($> 10...15$) values of $\tilde{A}$ while it is positive in the intermediate region ($1 < \tilde{A} < 10...15$). The negative values of τ_c mean that the martensitic embryo can be generated even under the action of an external shear stress of opposite sign. Interestingly, there are two cases of $\tau_c < 0$. In the first case, when $\tilde{A} < 1$ (the arm $2A$ of the ω-disclination dipole is more than two times smaller than the arms $2a$ of the $\Omega/2$-disclination dipoles), the attracting influence of the ω-dipole to the mobile $\Omega/2$-dipole is very weak due to the strong self-screening effect of $+\omega$- and $-\omega$-disclinations. In the second case, when $\tilde{A} > 10...15$ (the arm $2A$ of the ω-disclination dipole is more than $20...30$ times larger than the arms $2a$ of the $\Omega/2$-disclination dipoles), the attracting influence of the ω-dipole to the mobile $\Omega/2$-dipole is very weak, because the distances between $\pm\omega$-disclinations and $\Omega/2$-disclination dipoles are much larger than the distances between the mobile and immobile $\Omega/2$-disclination dipoles. However, both these cases do not fit well to our model where $\tilde{A}$ is assumed to vary from ≈ 1 to ≈ 3. Within this interval, τ_c is positive and increases with $\tilde{A}$ achieving $\tau_{c,\max}$ at $\tilde{A} \approx 3$.
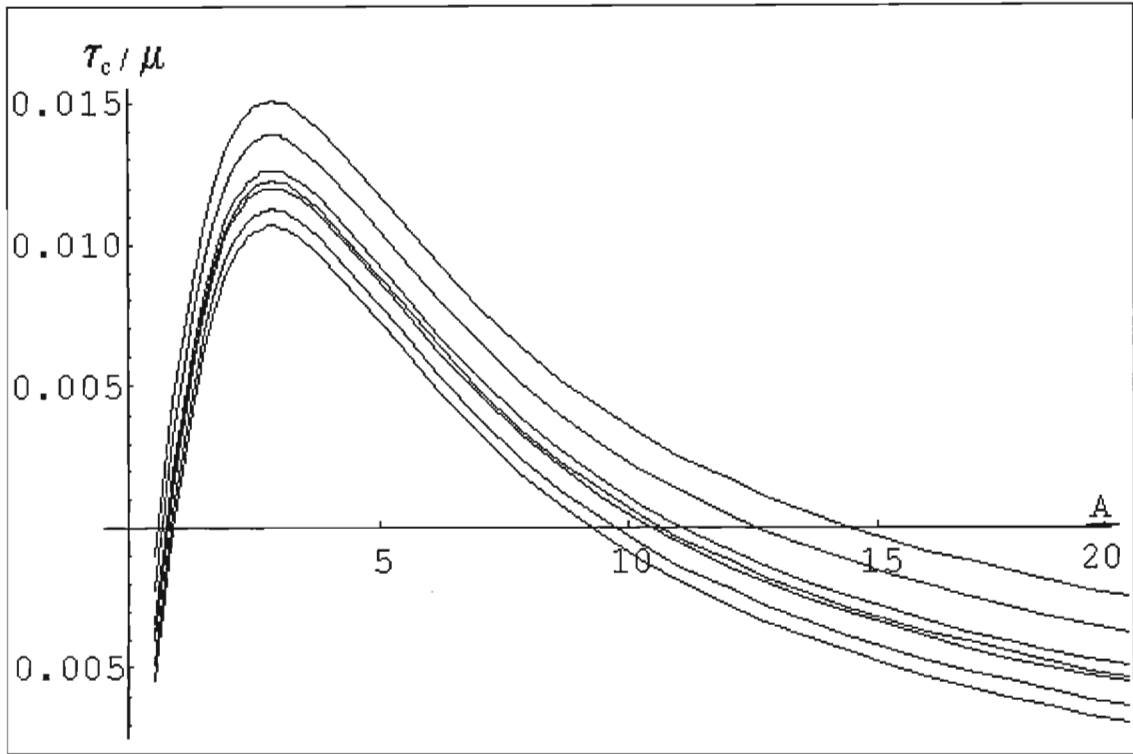
Figure 5. 21: The critical external shear stress τ_C vs. the normalised length $\widetilde{A}$ of half of the ωdisclination dipole arm for the temperature values T=100, 200, 250, 275, 300, 350 and 400K (from top to bottom)

The critical external shear stress τ_c varies in direct proportion with ω (Figure 5.22). It is negative for small values of ω and positive for large values. It is evident from Figure 5.21 and 5.22 that τ_c increases with the temperature T that is in accordance with intuition.
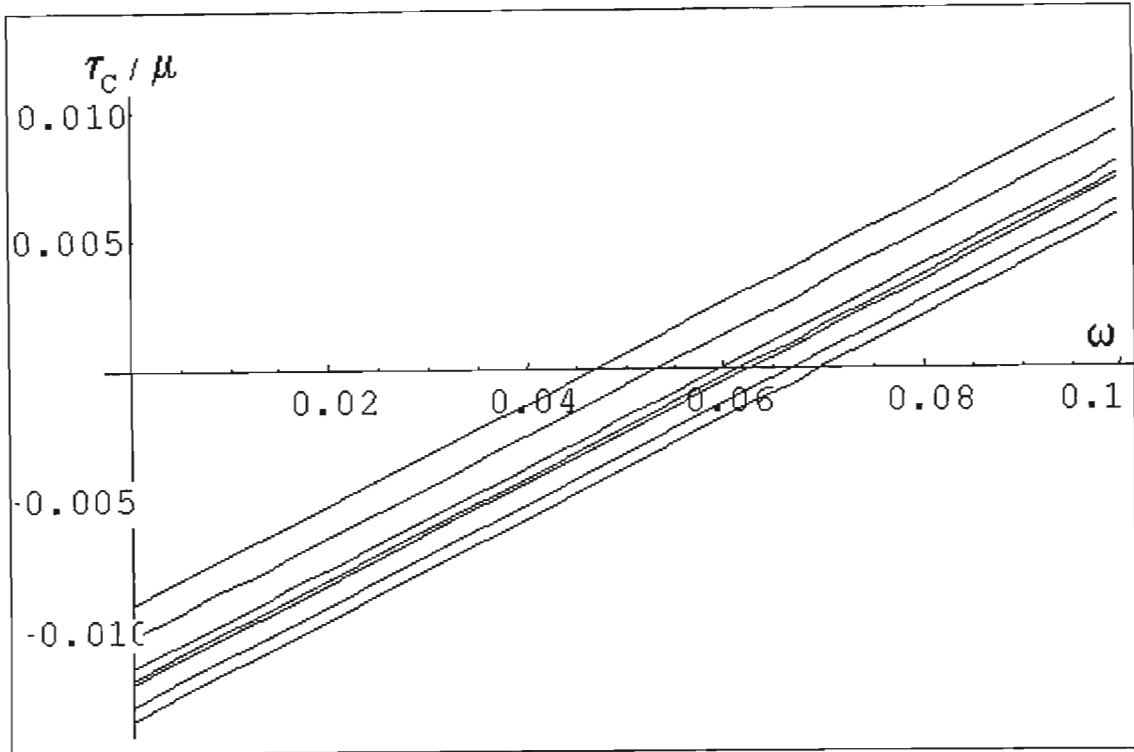
Figure 5. 22: The critical external shear stress τ_C vs. the strength ω of the "large" disclination dipole for the temperature values T = 100, 200, 250, 275, 300, 350 and 400K (from top to bottom)

Conclusion

A dislocation-disclination model is presented to describe heterogeneous nucleation of an embryo of hcp-martensite at a tilt grain boundary segment containing some extrinsic dislocations. The model is a further development of the well-known model by Olson and Cohen [194], with a more detailed account of elastic fields and the energies associated with the hcp-embryo. It incorporates both dislocation and disclination terms, leading therefore to more realistic results for the strain energy.

The total energy gain due to the hcp-embryo nucleation has been analyse in detail, and the existence of both the equilibrium and critical embryo sizes under some external conditions, temperature and shear stress, shown. Depending on the external conditions, these characteristic embryo sizes may vary in wide ranges: the equilibrium (critical) size increases (decreases) as the external shear stress increases and the temperature decreases. It has also been demonstrated that a critical external stress exists which provides athermal embryo nucleation when the nucleation energy barrier disappears and the terms of equilibrium and critical embryo sizes lose their significance. The critical external stress has been studied depending on the temperature and characteristic parameters of the grain boundary where the fcc-to-hcp martensite transformation

takes place. In particular, the critical external stress grows in direct proportion with the grain boundary misorientation angle. As might also be expected, it increases with temperature. In conclusion, the quantification of the various influences on martensitic nucleation provides the basis for accurately controlling the transformation as a design parameter.

CHAPTER 6

ALLOY FORMULATION AND TESTING

Strain memory alloys, as such, are not readily commercially available. And, although the metastability of many alloy systems has been thoroughly studied from the perspective of advantageous mechanical and forming properties, the notion of producing smart components is still too new to have produced a commercial group of materials known simply as strain memory alloys. Material specification for a smart mining bolt therefore involved a search of commercially available materials, as well as development of possible new candidate materials, with acceptable strain memory characteristics, and mechanical properties to satisfy the design criteria of the mining bolt.

The selection of a commercially available material would have produced the lowest prototype development cost, but not necessarily the lowest product cost. The unique range of manufacturing capabilities in the highly developed mining sector of the economy, make it possible to produce an entirely new alloy, and have it custom cast, forged, and rolled to final dimension in one material house that specialises in the production of mining material. This same manufacturing flexibility allows the production of relatively small (30kg – 300kg) batches of test material to be produced, for prototype testing, once initial material testing has been completed. Thus both commercially available material, as well as new custom alloys were tested and evaluated as possible candidates for the smart mining bolt. Their performance was rated in terms of cost, corrosion resistance, transformation characteristics, mechanical properties and machinability.

6.1 Test Procedures

6.1.1 Induction melting of specialised alloys

Some alloys were melted within the school of Mechanical Engineering at the University of Natal, and some were melted at Columbus Stainless steel. In the case of Columbus, the induction furnace used was a 25kg furnace, while the University's furnace melted only 6 kg. In both cases however, the same casting procedure was followed. Neither furnace was fitted with vacuum facilities, making precise raw material weights and careful casting procedures important. Care was also taken not to mix different alloy formulations in the same crucible, and a new crucible was therefore used for each different melt type.

Figure 6.1 shows the small induction furnace situated at the University of Natal. The furnace is mounted on a shaft attached to a large wheel, which turns easily through approximately 120° to allow easy pouring. The principle of using induction to melt material is relatively simple, and involves the use of a hollow copper coil as an induction. The water passing through this coil keeps it from melting, but allows a field to be generated, which couples with the metallic material in the crucible. This material then heats up, and given time, melts. The melting time is dependent on the geometry of the material: better inductive coupling occurs when the material is fairly large solid pieces, than when the material consists of small pieces (such as remelted iron) or flakes (such as manganese).

Figure 6. 1: A 6 kg induction furnace was used to melt experimental alloys

To avoid premature cracking of the crucible, the first melt in a new crucible was started very slowly, with a soaking time at a very low power setting, gradually increased over a period of

hours to 90% of the full power rating of the furnace. The raw materials were not added randomly, but in a pre-determined sequence dependent on their melting points, and tendency to burn off.

> ➤ Raw materials such ferrochrome, which is an iron and chromium mix, acquired in small rock-like form, is laid at the bottom of the crucible because of its high melting point.

> ➤ Remelted iron was used to make up the balance of the Fe content, and was partially added after the ferrochrome. The remelted iron was used because it is 99.5% pure and therefore simplifies considerably the determination of weights of raw materials to be used in a given melt. The melting process had to begin before all of the remelted iron could be gently pushed into the melting metal.

> ➤ Additions of materials such as nickel were the next to be added, and

> ➤ Electrolytic manganese followed. The addition of electrolytic manganese always caused difficulties, since it had a tendency to form a crust over the top of the melt instead of easily mixing in. Care was necessary to avoid a complete crust forming, since this caused superheating of the melt while a hole was broken through the crust from which to pour the molten metal.

> ➤ The last addition, where applicable, was carbon.

Figure 6. 2: Remelted iron can be seen on the top of the charge, which is beginning to melt.

Figure 6. 3: A ready-to-pour material

The melt was then poured into a permanent mould and allowed to cool slightly (see Figures 6.4(a) and (b)) before removal from the mould, heat treatment, and hot rolling, to remove some of the casting microstructure, and produce a more wrought material.

Figure 6. 4(a): Top view of a "just-poured" casting in a permanent mould
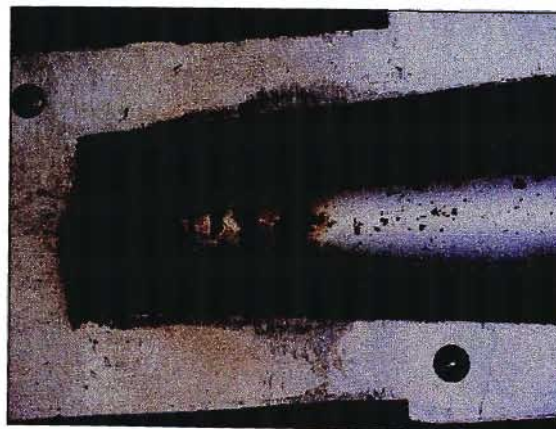
Figure 6. 4(b): Split permanent mould with side view of casting.

6.1.2 Tensile testing

Each candidate alloy was then subjected to a tensile test to ascertain yield and ultimate strengths in an Avery tensile machine shown in Figure 6.5. Specimen geometry is shown in Figure 6.6 below.
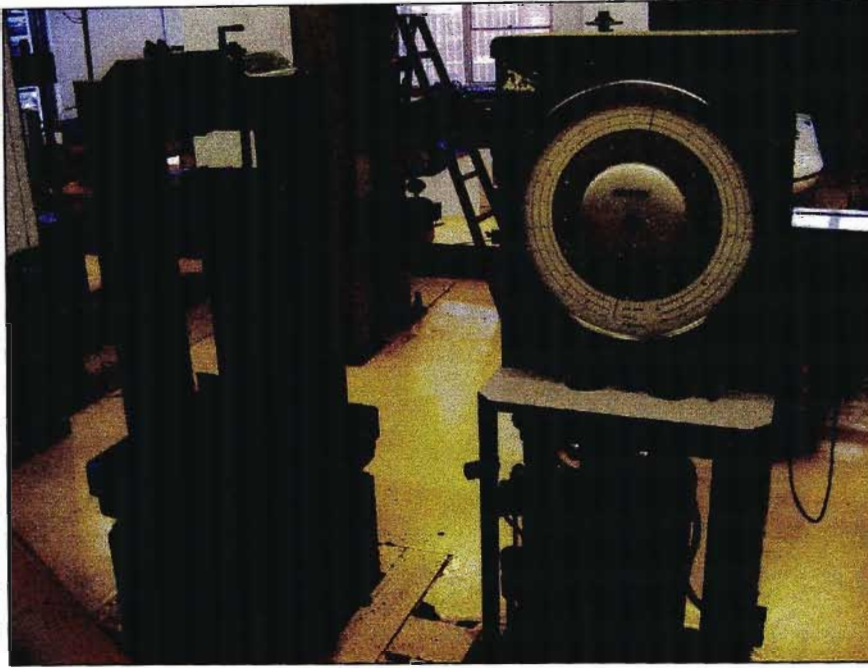
Figure 6.5: All tensile tests were performed on an Avery testing machine
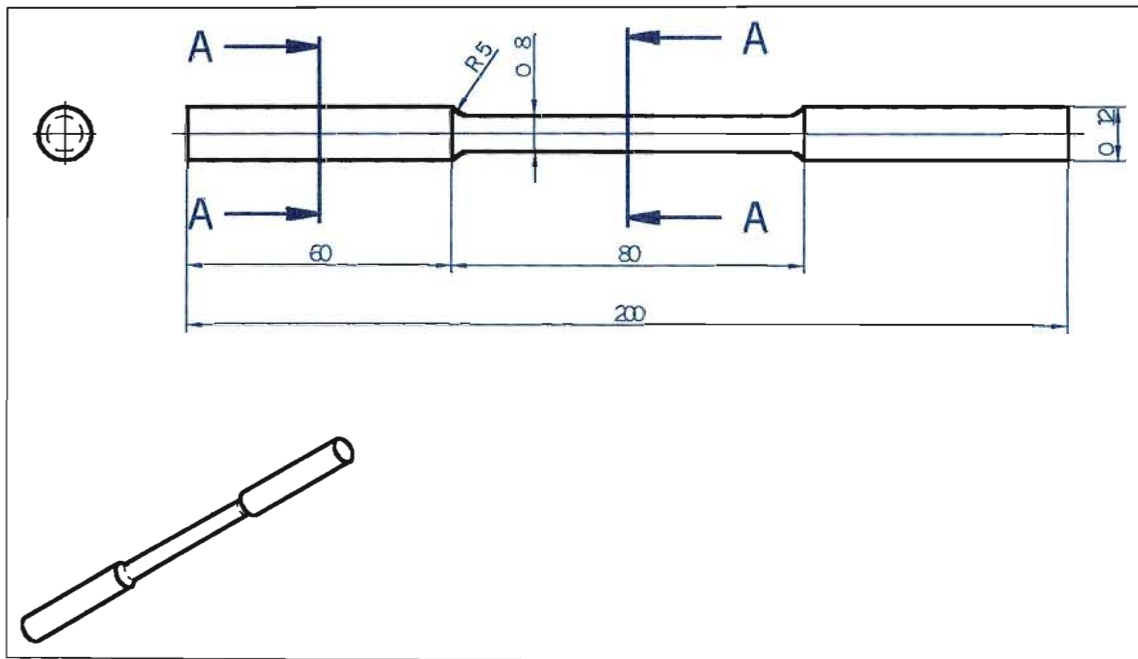
Figure 6.6: Tensile sample used for tensile properties as well as material inductive response

6.1.3 Inductive testing

Before tensile testing commenced, a coil was wound around the narrow test section of the specimen as shown in Figure 6.7 below, and this was connected to an inductance meter.

Figure 6.7: A coil was wound around the necked down section of the tensile sample

Graphs of uniaxial tensile strain were then plotted against inductance, which changed according to the changing permeability of the core material as predicted by the equation 3.5. The greater the percentage change in inductance over the testing range of the material, the more sensitive the material to strain-induced transformation. A combination of good strength characteristics as well as sensitive transformation characteristics was desirable.

6.1.4 Microstructural checks

A check on the correlation between inductance change and the percentage martensite present in the material was also conducted visually, using light and scanning electron microscopy. All samples were polished using an automatic Struers polishing machine, with a variety of grinding and polishing discs, as well as diamond suspensions and pastes. The exact polishing route can be found in the table below:

Table 6.1: Polishing method for all metallography

Grinding			Polishing		
Step	1st step	2nd step	Step	1st step	2nd step
Surface	MD Piano 220	MD Allegro	Surface	MD-Dac	MD-Chem
Abrasive	Diamond	DP-suspension	Abrasive	DP-suspension	OP-A
Grit size	-	9 μm	Grain size	3 μm	-
Lubricant	Water	Green/blue	Lubricant	Green/blue	-
RPM	300	150	RPM	150	150
Force (N)	180	180	Force (N)	180	90
Time (min)	Until plane	4	Time (min)	4	2

Many different etchants have been advocated for the etching of various metastable alloys [3,15] including some methods where it is possible to check four different phases at once, but for the purposes of this study, Kallings no.1 was found to be the most effective which is prepared according to Table 6.2.

Table 6.2: Kalllings etchant

Chemical	Amount
$CuCl_2$	1.5g
Ethanol	33 ml
HCl	33 ml
H_2O	33 ml

Any hardness tests performed were conducted using an automatic Rockwell Hardness Testing machine.

6.2 Alloy formulation

6.2.1 Previous Experience

Previous work on the use of strain memory alloys in passive peak smart strain sensors [84, 74] had indicated that good transformation characteristics could be produced using alloys from both the Fe-Cr-Ni and Fe-Cr-Mn groups. The strain sensing elements (of flat tensile specimen form) used in this smart strain sensor, were of minute proportions, and were electro-discharge machined from thin plate [0.4mm thick]. The changing magnetic permeability of the material was measured using a coil, and miniaturised electronic circuitry, which gave a reading measured in volts. The alloying chemistry of the two alloys used as sensor elements is given in the table below:

Table 6.3: Alloy compositions tested in a smart strain sensor

Alloy	Cr	Ni	Mn	C	N	S	P	Si	Fe
L1	13.08	1.94	15.65	0.01	0.0001	0.003	0.002	0.03	Bal
L1 was cast and rolled at Kawasaki steel in Japan, and is not locally available in South Africa									
Cr equivalent: 13.08 + 1.5(0.03) = 13.125 (using eqn. 4.1 Schaeffler de Long)									
Ni equivalent: 1.94 + 0.5(15.65) +30(0.01) +25(0.0001) = 10.07 (using eqn. 4.2)									
Alloy	**Cr**	**Ni**	**Mn**	**C**	**N**	**S**	**P**	**Si**	**Fe**
304	17.96	9.36		0.02	0.002			0.07	Bal
304 was bought locally, but "enormous" variability is found in the different batches purchased									
Cr equivalent: 17.96 + 1.5(0.07) = 18.06 (using eqn. 4.1)									
Ni equivalent: 9.36 + 30(0.02) + 25(0.002) = 10.01 (using eqn 4.2)									

6.2.1.1 Fe-Cr-Ni alloy

The stress-strain characteristics as well as the strain-voltage characteristics of 304 plate are shown in figures 6.8 and 6.9, while the mechanical properties are shown below in table 6.4.

Table 6.4: Mechanical properties of alloy 304

Alloy	304 plate (as received)
UTS (MPa)	850
σ_y (0,2%) (MPa)	500
elongation	70%
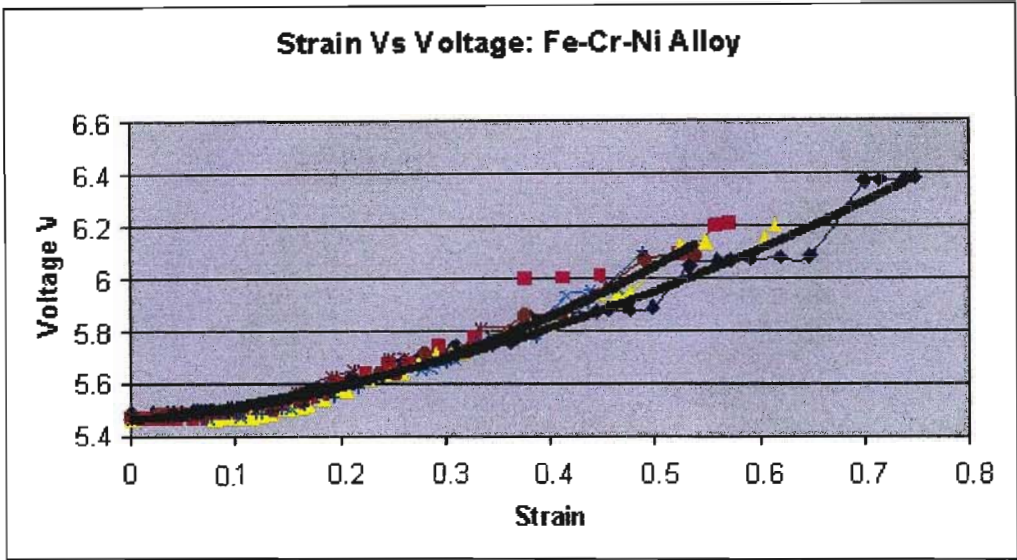
Figure 6. 8: Strain-voltage response of alloy 304
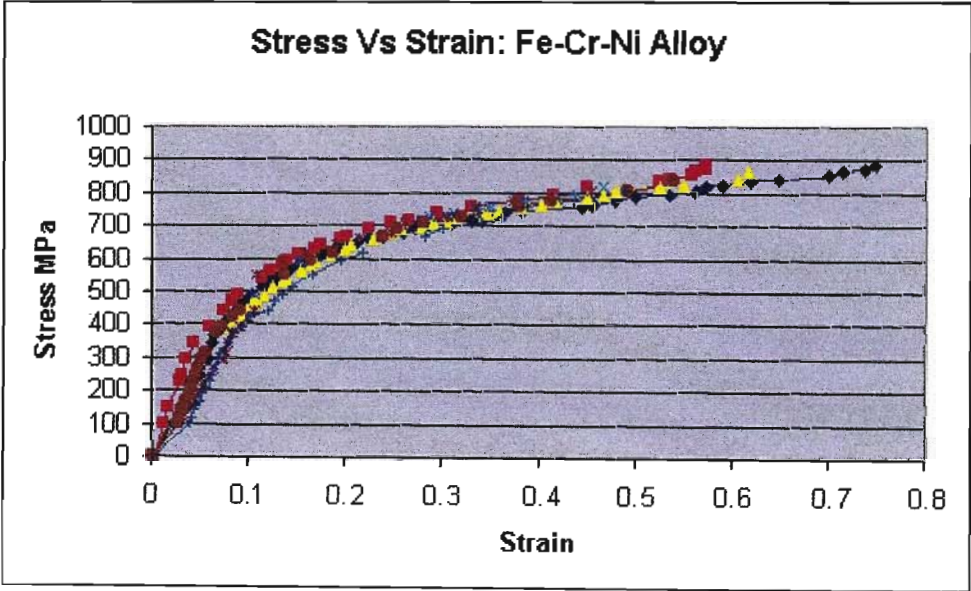
Figure 6.9: Stress-strain response of 304 alloy

6.2.1.2 Fe-Cr-Mn alloy

The mechanical properties for alloy L1 are given in Table 6.5 below, while the stress-strain characteristics, and strain-voltage characteristics are shown in Figures 6.10 and 6.11.

Table 6.5: Mechanical properties of alloy L1

Alloy	L1 (annealed)
UTS (MPa)	650
σ_y (0,2%) (MPa)	450
elongation	50%
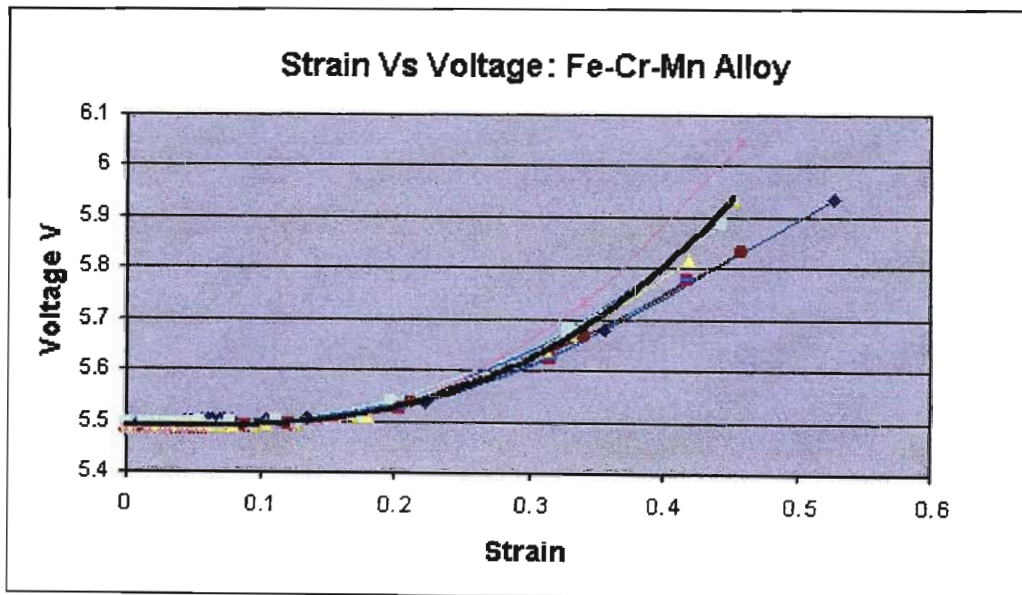
Figure 6.10: Strain voltage response of alloy L1
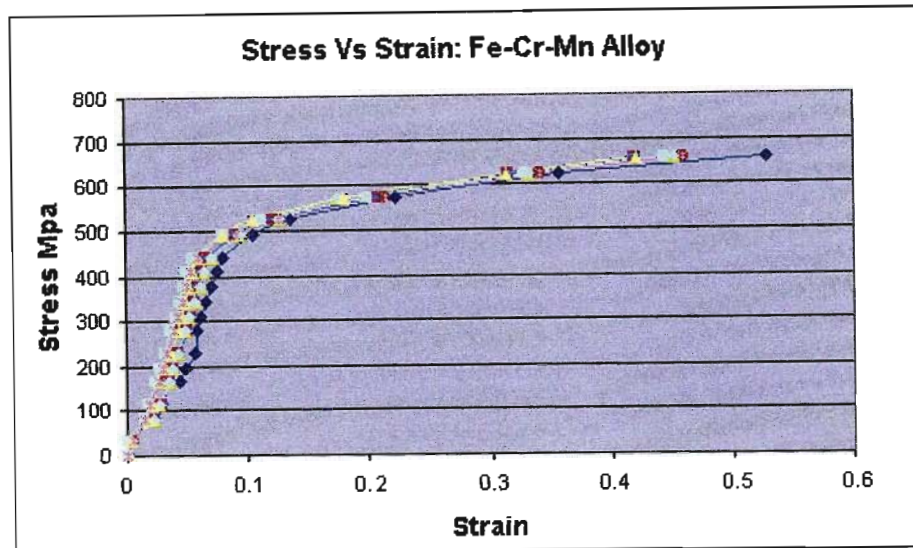
Figure 6.11: Stress-strain response of alloy L1

Both the yield strength and the tensile strength of the 304 alloy were found to be higher, as well as the elongation. The most interesting feature of graphs 1 and 2, however, is in the transformation characteristics of the two alloys. The L1 alloy produced a very smooth graph, with a continuously changing voltage as strain changed. The 304 alloy, however, displayed "steps" in the transformation, suggesting that perhaps the martensite formed in bursts. As a strain sensing material this is not a particularly desirable feature, since the strain may change, but not the damage indication – see Figures 6.8 and 6.10.

Using this previous research as a starting point, the commercially available option was considered, along with several other alloy compositions, as presented in the following sections. All alloys considered contained substantial amounts of chromium, for the corrosion resistance it imparts, as well as for the stabilisation of the BCC phase [190]. The remaining elements were selected on the basis of austenitic stabilising effect, strengthening effect, their influence on machinability, and all weighed against the cost factor.

126

6.2.2 Fe-Cr-Ni alloys:

The commercially available austenitic stainless steels known to be somewhat metastable with respect to deformation, are 301, 302 and 304. The nominal compositions of these alloys are shown below in Table 6.6.

Table 6.6 Nominal Compositions of metastable austenitic stainless steels

Alloy	Cr	Ni	C (max)
301	17	7	0.15
302	18	9	0.15
304	19	9	0.08

Of the three, only 304 is actually commercially available in South Africa, and was tested, along with a low carbon version of 301, specially prepared at Columbus Stainless Steel, the composition of which is given in table 6.8 below, and denoted C1. The alloy 304, although previously tested in thin plate form for the smart strain sensor, was re-tested in round bar form for the sake of completeness, as well as because the as received condition was unknown – that is suppliers do not specify whether the material arrives in annealed condition, or whether it has been cold-worked to some extent.

Table 6.7: Composition of alloy C1 melted at Columbus Stainless Steel

Alloy	Cr	Ni	Mn	C	N	Si	Cu	S	Mo	P	Fe
C1	16.32	7.04	0.13	0.042	0.0303	0.10	0.02	0.013	0.01	0.013	Bal
Cr equivalent: 16.32 + 1.5(0.1) = 16.47								(using eqn. 4.1)			
Ni equivalent: 7.04 + 30(0.042) + 0.5(0.13) + 25(0.0303) = 9.12								(using eqn. 4.2)			

A comparison of mechanical properties is given in Tables 6.8, while typical inductance values for various load values are plotted in Figures 6.12 and 6.13.

Table 6.8: Mechanical properties of alloys 304 and C1

Alloy	304 (annealed)	Alloy	C1
UTS (MPa)	733	UTS (MPa)	700
σ_y (0,2%) (MPa)	319	σ_y (0,2%) (MPa)	304
elongation	83%	elongation	85%
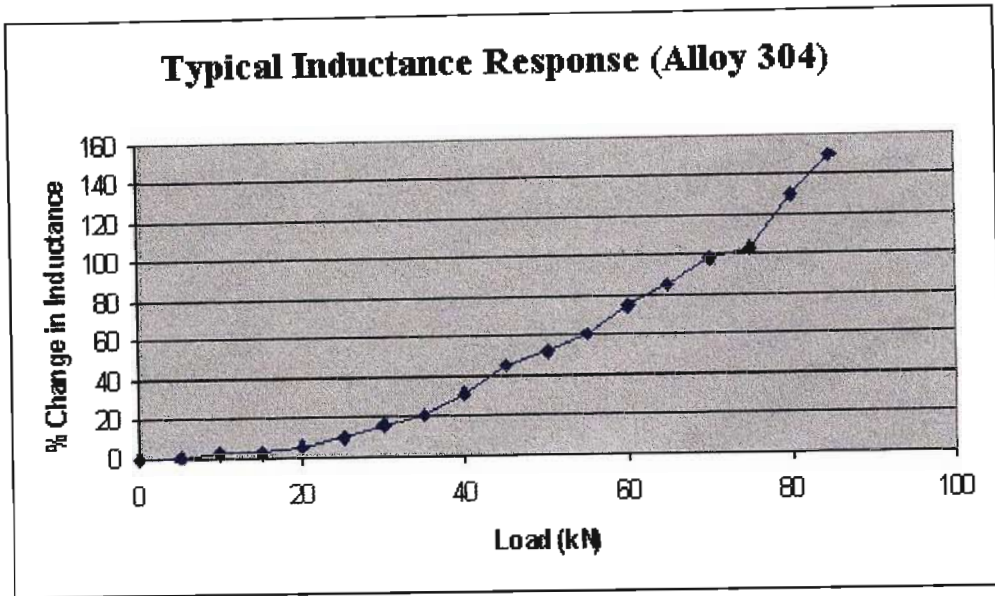
Figure 6.12:Typical Inductance Response for varying load – Alloy 304
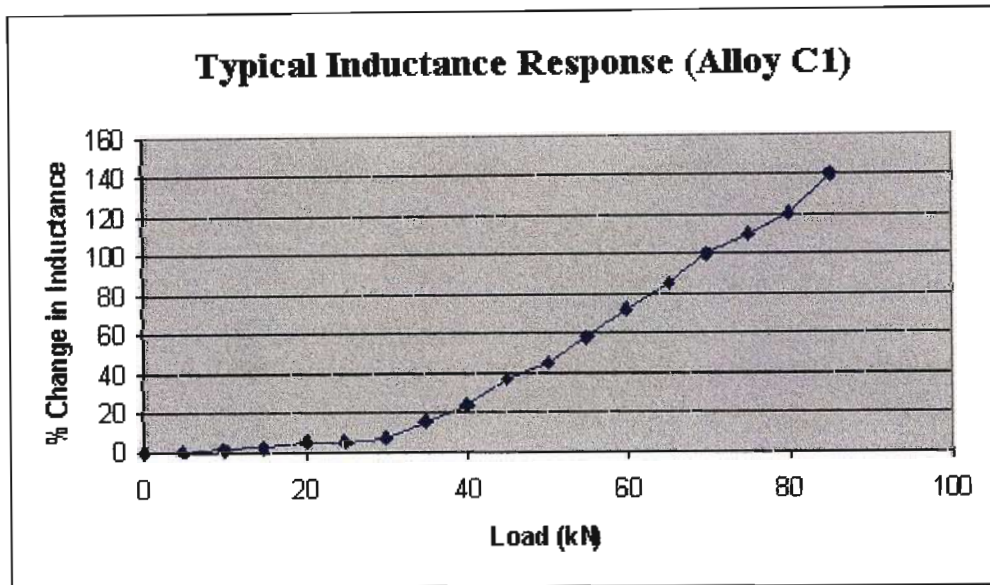
Figure 6.13: Typical Inductance Response for varying load – Alloy C1

The tables and figures presented above show that in terms of mechanical strength, there is not a huge difference in the two alloys, with similar characteristics in terms of transformation characteristics. Both alloys produced approximately a 140% change in inductance measurement as they transformed over the range of the tensile test. This transformation is further evidenced in microstructures taken from the necked region of the fractured tensile sample. The dark regions

128

in the scanning electron microscope image shown in Figure 6.14 below, are martensite, while the white regions are retained austenite.

Figure 6.14: Microstructure in neck region of tensile fracture of alloy 304. (Mag. 400x)

There are a number of disadvantages for this group of alloys, however, not least of which is the very high cost of Nickel as an alloying element. Some of the more common alloying materials are tabulated below, with their prices (July 2002) per kg.

Table 6.9: Costs of Raw Materials

Raw Material	Price (per kg)
Re-melted Iron	R 9-50
Ferrochrome	R 22-50
Nickel	R 109-00
Electrolytic Manganese	R 22-50
Carbon	R 4-15

The variability in the commercially acquired 304 is substantial, varying from supplier to supplier and batch to batch; and, the effect of this on transformation characteristics, would mean a calibration nightmare. If then the alternative was to develop a new alloy, which would be custom made for mining bolts alone (and facilities for such an operation do exist in South Africa, as we enjoy the existence of many smaller more flexible manufacturing companies) then the obvious strategy would be to replace some of the costly Nickel with the cheaper austenitic stabilisers. Further candidate materials were considered therefore considered.

6.2.3 Fe-Cr-Mn alloys

The replacement of Nickel (in the austenitic stainless steel group) either partially or totally, with Manganese, is well-documented; although decreased formability seems to have curtailed their wide-spread use. Alloy C2 was partially replaces nickel with manganese as its austenitic stabiliser, because the hot rolling characteristics of the material degrade as the manganese content rises. Having only half the "austenising power" of Nickel, manganese concentration bands are therefore more forgiving in terms of commercial specifications. The composition of alloy C2 is shown in Table 6.10, with mechanical properties (as extracted from tensile testing) are shown in Table 6.11.

Table 6.10: Composition of Fe-Cr-Mn alloy C2

Alloy	Cr	Ni	Mn	C	N	Si	Cu	S	Mo	P	Fe
C2	13.78	2.50	15.52	0.044	0.03	0.04	0.01	0.01	0.01	0.011	Bal
Cr equivalent: $13.78 + 1.5(0.04) = 13.84$					(using eqn. 4.1)						
Ni equivalent: $2.5 + 0.5(15.52) + 30(0.044) + 25(0.03) = 12.33$						(using eqn 4.2)					

Table 6.11: Mechanical Properties of Alloy C2

Alloy	C2
UTS (MPa)	963
σ_y (0,2%) (MPa)	574
elongation	70%

The typical inductance response (see Figure 6.15) of this alloy shows a 155% change in inductance over the testing range. The sudden increase occurring as the material starts to yield, which concurs with the pre-tensioning point of the mining bolt. The microstructure shown in Figure 6.16 is taken from the necked section of a fractured tensile sample, and again the dark areas are etched to be martensite, while the remaining white areas are austenite.

130
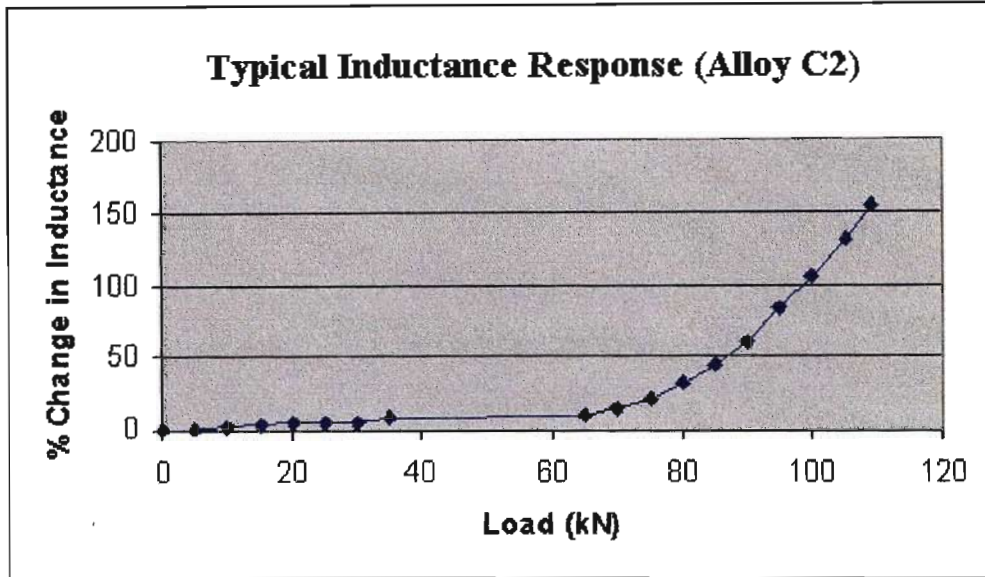
Figure 6.15: Typical Inductance Response of alloy C2, varying with applied load.
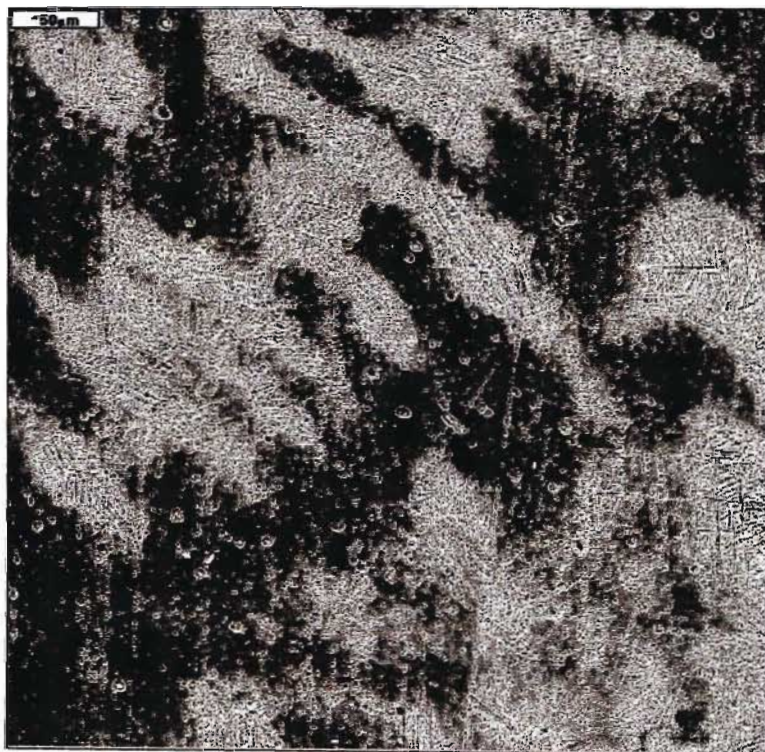
Figure 6. 16: Microstructure in neck region of tensile fracture of alloy C2. (Mag. 400x)

6.2.4 Fe-Cr-Mn-C alloys

The final alloy tested replaced the nickel completely with manganese and carbon as austenitic stabilisers. The chemistry of alloy B1 is shown in Table 6.12 below, and the mechanical properties in table 6.13. Although this alloy is actually the cheapest of the alloys to produce, and the transformation characteristics seen in Figure 6.17 below are very comparable to those of C2, the machining characteristics of this alloy are prohibitive. As the elongation indicates, the material is brittle, and on attempts to machine this composition, the conclusion was reached that it is unsuitable for the purposes of the smart mining bolt.

Table 6.12: Alloying chemistry for alloy B1

Alloy	Cr	Mn	C	N	S	P	Fe
B1	12±1.0	10±1.0	0.25±0.03	0.1 max	0.025 max	0.025 max	Bal.
Cr equivalent: 12							
Ni equivalent: $30(0.25) + 0.5(10) + 25(0.1) = 15$ max.							

Table 6.13: Mechanical properties of alloy B1

Alloy	B1 (annealed)
UTS (MPa)	1063
σ_y (0,2%) (MPa)	438
elongation	30
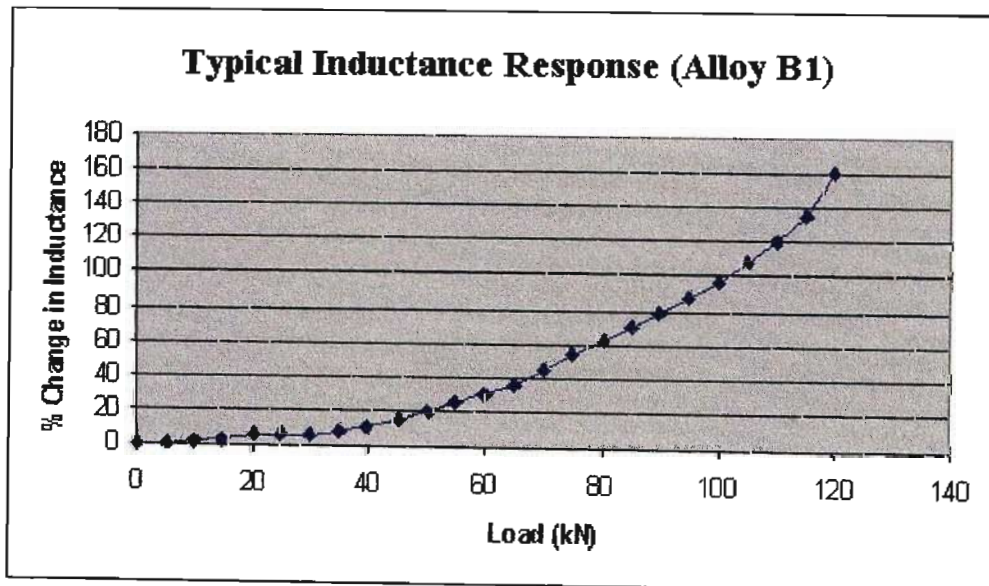
Figure 6. 17: Typical inductance response varying with load, for alloy B1

6.2.5 Alloy selection and further testing

The relative stabilities of alloys C1, C2 and B1 are shown in the modified Schaeffler De Long diagram of Figure 6.18 below, and confirms the better transformation properties of alloys C2 and B1. Based on the mechanical and transformation properties of C2, and the poor machining properties of alloy B1, the alloy C2 was chosen as the smart mining bolt material. Further testing of this material, as well as sensor testing then proceeded.
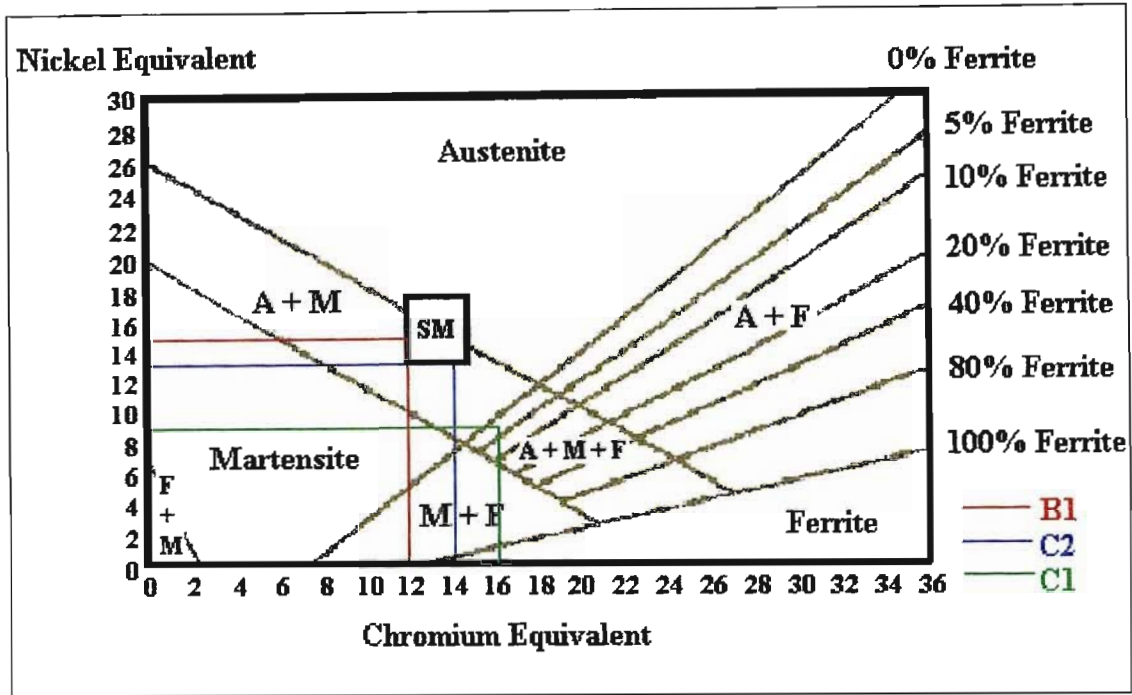
Figure 6. 18: Stability of alloys C1, C2 and B1 shown on Schaeffler De Long diagram.

6.2.5.1 Compression testing

Although the mining bolt will see predominantly tensile loading, the shear loading, and crushing of the bolt in extreme circumstances warranted a check of the inductive response of the material under compressive conditions. Several samples were then tested compressively in the same Avery machine as was used for the tensile testing, their deformed state is shown in Figure 6.19 below, and the inductance response in Figure 6.20. It is immediately evident that compressive loading does not produce the same difference in inductance as tensile loading, but a detectable difference is nevertheless produced. This phenomenon was to be expected in some degree, because many researchers [280] have noted that tensile extension produces more martensite than compressive stress.

133

Figure 6. 19: Deformed Compression samples (Alloy C2)
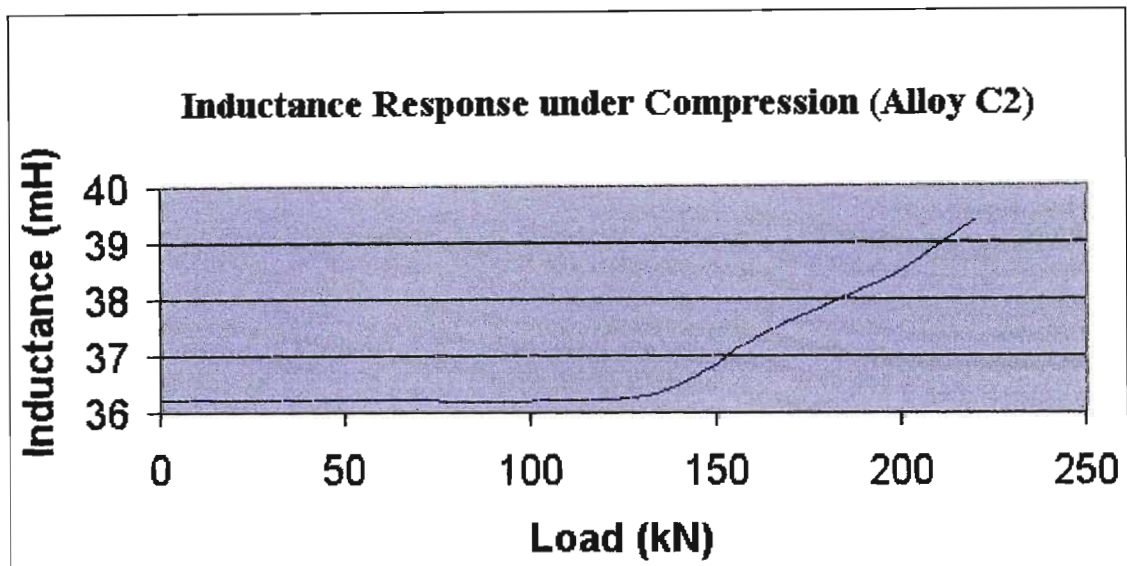
Figure 6. 20: Inductance change under compressive load (Alloy C2)

6.2.5.2 Thermal Processing

An attempt was also made to determine whether is would be possible to use Koppenaal's thermal processing technique to strengthen and destabilise the C2 alloy. The first part of the test was to discover whether martensite could be formed in sufficient quantities at liquid nitrogen temperature, to actually strengthen the alloy. An inductance reading was used as a measure of the martensitic transformation. The results of these tests can be seen in Tables 6.14, 6.15 [279].

The lack of appreciable change in the inductance suggested that the M_s temperature of alloy C2 was too low for large quantities of martensite to form at liquid nitrogen temperatures. The small increase in hardness after cooling, was attributed to the small amounts of martensite that did appear to form, as seen in the microstructure shown in Figure 6.21.

Table 6.14: Variation of inductance with temperature for alloy C2

Temperature (°C)	25	-156.7	-158	-160	-173
Inductance (mH)	111.3	110.8	110.8	110.8	110.8

Table 6.15: Hardness readings before and after cooling of alloy C2 to –173°C

Hardness reading before cooling (HR$_C$)	51.80
Hardness reading after cooling (HR$_C$)	54.87
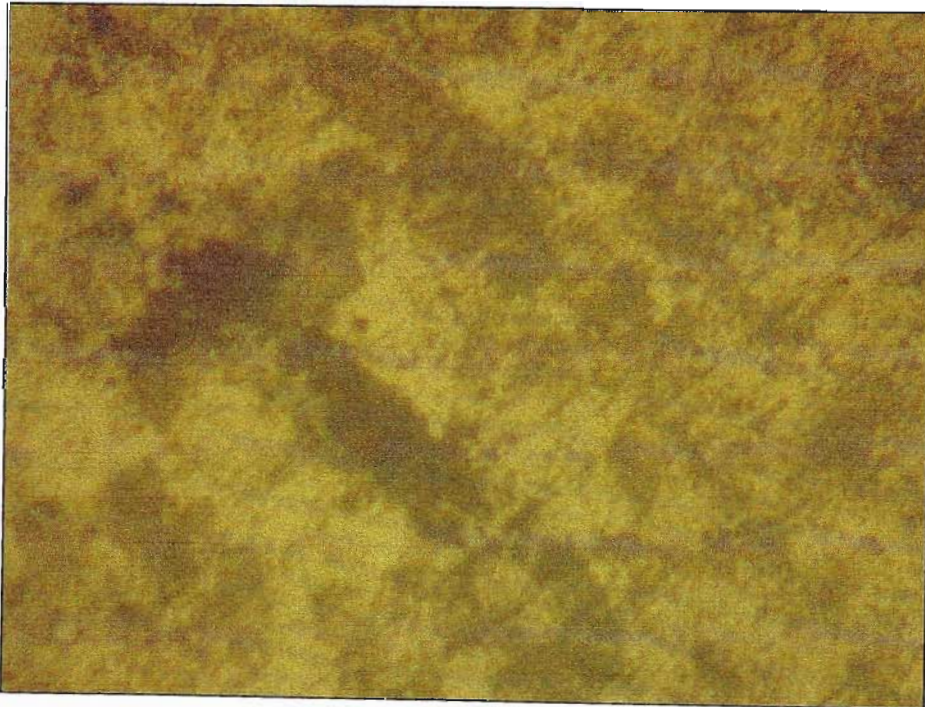
Figure 6. 21: Small amounts of martensite visible in alloy C2 after cooling to –173°C

It was therefore concluded that alloy C2 was unsuitable for thermal processing, and that any destabilisation of austenite would have to be applied through thermo-mechanical processing or rolling.

6.3 Sensor Testing

The sensor concept shown in chapter 3 was contracted to a company specialising in custom electronics. The first prototype of this sensor has been received and tested, the results of which are shown in Figure 6.22 below. As is evident, the circuit needs still needs fine-tuning, and further iterations are expected before final bolt testing.
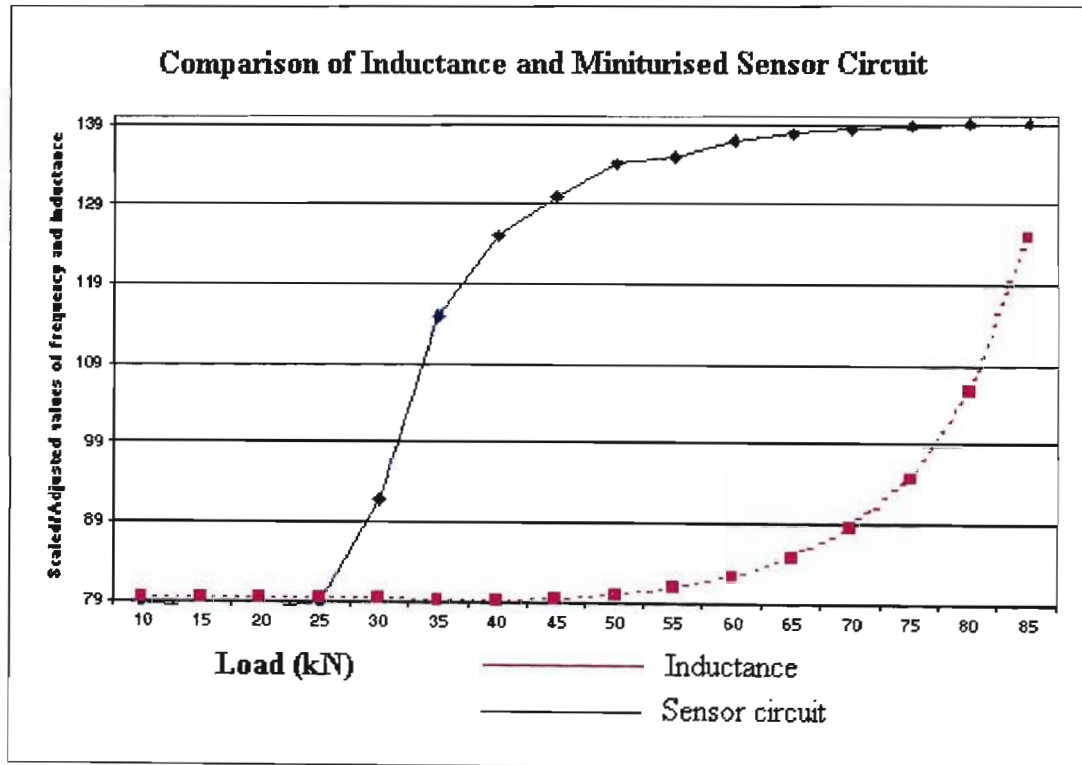
Figure 6. 22: Sensor Test – first prototype

6.4 Conclusion

After extensive alloy testing, a material has been selected for the smart mining bolt prototype, and has the following nominal chemistry:

Fe-13Cr-2.5Ni-16Mn – low carbon, low nitrogen

The selected alloy meets the SABS standard for mining bolt material, in terms of strength and ductility, as well as having sufficient corrosion resistance for the mining environment. The cost of this alloy is also favourable, having replaced much of the Nickel content with manganese, and machining characteristics are acceptable. Most importantly, the transformation characteristics of this material meet the requirements for it to act in a strain monitoring capacity.

CONCLUSION

A thorough study of the relatively new science of structural health monitoring, and the use of smart materials to achieve continuous monitoring, was conducted. Although many smart materials are costly, a group of relatively inexpensive metastable alloys known as strain memory alloys were identified as capable of use in the dual role of load-bearing and peak strain sensing. This attribute prompted a further investigation into the chemistry and processing of strain memory alloys with the view to using such a material to monitor the structural health of mining tunnels in South Africa, by replacing some of the currently used rock anchors with smart rock anchors. To implement such a health monitoring system, several inter-dependent tasks were performed, as detailed below.

In the search for a suitable material from which to construct a smart mining bolt, strain memory alloys were extensively researched in regard to their alloying constituents, processing, and subsequent transformation characteristics on application of strain. An analytical model was presented which takes account of the various energy contributions of temperature and strain, in the nucleation of martensitic embryos. As martensitic nucleation is known to occur preferentially at defect sites or grain boundaries, these conditions are modelled using both dislocation and disclination terms to account for the strain energy imparted by PDA. The existence of equilibrium and critical embryo sizes are shown to exist under certain external conditions of temperature and shear stress. It is also demonstrated that a critical external stress exists which induces athermal embryo nucleation when the nucleation energy barrier disaperas and the terms of equilibrium and critical embryo size lose their significance.

Several candidate alloys were then formulated from various alloy families including:

- Fe-Cr-Ni
- Fe-Cr-Mn, and
- Fe-Cr-Mn-C

Each candidate alloy was evaluated in terms of strength characteristics, with specific reference to the SABS standard requirements for mining bolt materials. At the same time as tensile testing was conducted, the martensitic transformation characteristics were also monitored by measurement of magnetic permeability using a coil and inductance meter.

The general corrosion characteristics were engineered at alloy formulation stage with the inclusion of sufficient chromium, and it was therefore not necessary to test specific corrosion response of the material. A major concern was however, the machinability and workability of the alloy, since manufacturing considerations impinged directly on the cost to produce a smart bolt.

The material considered to achieve the required cost, machining and transformation characteristics was of nominal composition:

$$Fe - 13Cr - 16Mn - 2,5Ni - low\ C - low\ N.$$
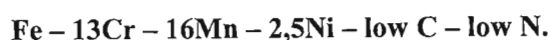
In selection of this alloy the commercial melting, forging and rolling processes were considered carefully to make sure that such a material could be produced industrially and within the compositional variation that prevails in commercial facilities. That is, account was taken of the fact that industrial melting facilities need an alloying window to work to. An alloy was therefore chosen which would be "forgiving" or have a decent operational window.

Apart from the alloy selection, careful attention was focused on incorporating within the final prototype design, a means of assessing the amount of damage incurred by the bolt. To this end consideration was given to a number of methods of measuring magnetic susceptibility, among them, the Hall effect, an inductance method, use of SQUID, as well as a fluxgate magnetometer. The selection of an inductance method was prompted by the fact that it was most easily adapted to the physical constraints of the rock anchor environment.

Thus, a material has been engineered, and a prototype design proposed for the production of a smart mining bolt. The material and design concept have been proven through experimental work, but the final acid test remains: an in-situ test. Further work is still required to confirm the behaviour of the bolt under mixed-mode loading, as well as the ruggedness test that only actual installation within a mine can satisfy. The in situ testing will prove not only the ruggedness, but will also be needed for the final programming of the data extraction sensor – that is the intervals deemed safe, cautionary and dangerous (denoted green, yellow, and red respectively on the digital display of the bolt sensor head) still need to be determined in co-operation with mining personnel.

GLOSSARY

Paramagnetic – Magnetic moments tend to align when an external magnetic field is applied, but only small positive susceptibility (10^{-2}) is exhibited. [240]

Ferromagnetic – The atoms of ions have magnetic moments which in certain domains are held in approximately parallel alignment in the absence of an externally applied magnetic field. When an external magnetic field is applied, the resultant moments of the domains tend to align. Permeability is considerable, most often greater than 2. [240]

Stope face – The stope face is the location at which the precious metal is actually mined from the thin seam that is ore-bearing. It is here that the miners blast and drill the rock to remove that which is profitable to transport to the surface and refine.

REFERENCES

1. M Tominaga, L Thompson, B Westermo, Design and Maintenance Conference, "Passive peak sensor technology: development and applications" October 1999, Japan.

2. L Thompson, B Westermo, "Damage detection and monitoring in composite materials using metastable alloy and mechatronic sensors", Proceedings QNDE Conference, Snowbird, UT, July, 1998.

3. L Thompson, B Westermo, et al, "Passive and Active Monitoring Experience: Civil Engineering Applications", Proceedings of QNDE, Montreal, Canada, 1999.

4. Q Liu, S S Rao, "Structural Health Monitoring: A Survey" Department of Mechanical Engineering, University of Miami, 2002, (currently unpublished).

5. Akhras G., Advanced composites for smart structures, Proceedings of the 12th International Conference on Composites Engineering, Paris, 1999.

6. Cross L. E., Piezoelectric and electrorestrictive materials for transducer applications, Goodyear Aerospace Corporation Report No. Ger 14188, Akron, USA, 1987.

7. Fisher M. and Hill E., Neural network burst pressure prediction in fibreglass/epoxy vessels using acoustic emission, Proceedings of the 6th International Symposium on Acoustic Emission from Composite Materials, San Antonio, Texas, June 1998

8. Smart Aircraft Bolt Technology project report 1999/2000, School of Mechanical Engineering, University of Natal. Prepared for ARMSCOR

9. L Thompson, B Westermo, M Tominaga, "Monitoring Based Maintenance for Civil Engineering Structures", International Conference on Safety and Reliability, Newport Beach, June 2001

10. Bauer, W., Event monitoring functions introduced by the on-board life monitoring system (OLMOS) into a German Aircraft, DFVLR-Mitt. 88-04, 1987.

11. Mook, G., Phol, J., Michel, F., Benziger, T., Damage evaluation of smart CFRP-Piezoelectric materials using non-destructive methods, Proceedings of the 12th International Conference on Composite Materials, Paris, 1999

12. Boller, C. and Biemans, C., Structural health monitoring in aircraft – state of the art, perspectives and benefits, Proceedings of the International Workshop on Structural Health Monitoring, Ed. Chang, F., Stanford, 1997.

13. Loewy, R. "Recent developments in smart structures with aeronautical applications". Smart Mater. Struct. (6) 1997.

14. Pines, J. and Lovell, P. "Conceptual framework of a remote wireless health monitoring system for large civil structures." IOP Publishing Ltd.,1998

15. Murukeshan, V.M., Chang, P.Y., Asudi, A. "On-line health monitoring of smart composite structures using fiber polarimetric sensor". Smart Mater. Struct. (8) 1999.

16. Wang, M.L., Heo, G., and Satpathi, D. "A health monitoring system for large structural systems". IOP Publishing Ltd., 1998.

17. Shakeri, C., Noori, M., and Hou, Z. "Smart Materials and Structures. A review." Tech. Report of Worcester Polytechnic Institute, 1998.

18. Aktan, A.E., Helmicki, A.J., and Hunt, V.J. "Issues in health monitoring for intelligent infrastructure". IOP Publishing Ltd., 1998

19. Rogers C. A., Liang C. and Li S., Active damage control of hybrid material systems using induced strain actuators, Proceedings of the 32nd AIAA Conference on Structures, Structural Dynamics and Materials, Baltimore, USA, 1991

20. Thompson L., Westermo B., Crum D., Law W. and Trombi R., Smart structural fasteners for aircraft and construction industries, Proceedings of the SPIE Conference on Smart Structures and Materials, Newport Beach, USA, 1999.

21. V Verijenko, **B Burton**, W Ostachowicz, "Development of Smart Composite materials with peak strain sensing capabilities" ICCE/8, July 2001, Tenerife, Spain

22. **B Burton**, V Verijenko, S Shaik, "Smart Composite materials with embedded metastable ferrous alloy sensors", ICCE/9, July 2002, San Diego, USA

23. Askar, Attila, "Lattice Dynamical Foundations of Continuum Theories: Elasticity, Piezoelectricity", *Series in Theoretical and Applied Mechanics, Volume 2,* World Scientific Publishing Company.

24. Buchanan, Relva C., "Ceramic Materials for Electronics", Marcel Dekker, Inc., 1971.

25. Cady, Walter Guyton (1946) "Piezoelectricity: An Introduction to the Theory and Applications of Electromechanical Phenomena in Crystals", reprinted by Dover Press, 1964.

26. Crandall, Dahl and Lardner, "An Introduction to the Mechanics of Solids", McGraw-Hill, 1978.

27. Gagnepain, J.J., and Meeker, T.R., "Piezoelectricity", 1982

28. Herbert, J.M. (1982), "Ferroelectric Transducers and Sensors", Gordon & Breach Science Publishers, 1982.

29. Ikeda, Takuro, "Fundamentals of Piezoelectricity", Oxford University Press, 1990.

30. Jaffe, Cook & Jaffe, "Piezoelectric Ceramics", Academic Press Inc. Ltd, 1971.

31. Katz, H.W., "Solid State Magnetic and Dielectric Devices", John Wiley, 1959

32. Lucas, I., "Transformation of Energy in Piezoelectric Drive Systems", 1975

33. Mason, Warren Perry, "Fifty Years of Ferroelectricity", *Journal of Acoustical Society of America, Volume 50, No. 5*, 1971.

34. Mason, Warren Perry, "Piezoelectricity: Its History and Applications", *Journal of Acoustical Society of America, Volume 70, No. 6*, 1981

35. Nye, J.F.,"Physical Properties of Crystals", Oxford University Press.

36. Okazaki, Kiyoshi, "Developments in Fabrication of Piezoelectric Devices", Ferroelectrics, Volume 41, 1982.

37. Rosen, Carol Zwick, et al, "Piezoelectricity", *Key Papers in Physics, American Institute of Physics*.

38. Taylor, George, "Piezoelectricity", *Ferroelectricity and Related Phenomena, Volume 4*, Gordon & Breach Science Publishers.

39. Tiersten, H.F., "Linear Piezoelectric Plate Vibrations - Elements of the Linear Theory of Piezoelectricity and the Vibrations of Piezoelectric Plates", Plenum Press, 1969.

40. Uchino, Kenji, "Piezoelectric Actuators and Ultrasonic Motors", Kluwer Academic Publishers, 1997.

41. van Randeraat, J., and Setterington, R.E., (Eds.), "Piezoelectric Ceramics", Eindhoven, The Netherlands, 1968.

42. Zheludev, I.S., "Physics of Crystalline Dielectrics, Volume 2, Electrical Properties", Plenum Press, 1971.

43. Zhong, Weilie, "Piezoelectric Physics", Science & Technology Publishing House (China), 1996.

44. Zaki,A.S., Pandell,T., Jacques,R., and Spangler, R. "Damage Detection in Thick Walled Composites using Surface Mounted Piezoelectric Elements" Tech.Report of Active Control eXperts, Inc., USA, 2000.

45. Egusa,S., Iwasawa, N., "Piezoelectric paints as one approach to smart structural materials with health-monitoring capabilities." Smart Mater. Struct. 7 (1998) 438-445.

46. Kang, Y., et al "Multi-Modal vibration control of laminated composite plates using piezoceramic sensors/actuators". J. Intelligent Material Systems and Struct. 12, 1999.

47. Pardo de Vera, C., and Guemes, G., "Embadded Self-sensing piezoelectric for damage detection." J. Intelligent Material Systems and Struct. 11, 1999.

48. Tracy, M., Fu-Kuo Chang "Identifying Impacts in composite plate with piezoelectric strain sensors" J. Intelligent Material Systems and Struct. 11, 1999.

49. Isupov, V. A. and Smirnova, E. P., "Electrostriction in Various Ferroelectric Ceramics with Diffuse Phase Transition", Ferroelectrics, Volume 90, 1989.

50. Smirnova, E. P., Sotnikov, A. V., Kochina, I. I. and Glazunov, A. E., "Effect of Microstructure on Electrostrictive Properties of Ceramics with Diffuse Phase Transition", *Izv. Acad. Nauk SSSR, Ser. Fiz., Volume 54*, 1990.

51. Lemanov, V. V., Yushin, N. K., Smirnova, E. P., Sotnikov, A.V., Tarakanov, E. A and Maksimov, A. Yu., "Giant Electrostriction of Ferroelectrics with Diffuse Phase Transition: Physics and Application", *Ferroelectrics, Volume 134*, 1993.

52. Smirnova, E. P., Rubinstein, O. V., and Isupov, V. A., "Dielectric and Electrostrictive Properties of PMN-Based Complex Perovskites", *Ferroelectrics, Volume 143*, 1993.

53. Yushin, N.K., Smirnova, E. P., Tarakanov, E. A. and Sommer, R., "Ferroelectric Lead Magnoscandoniobate Solid Solutions – Acoustic Dielectric and Electrostrictive Properties", *Fiz. Tverd. Tela (Physical Solid State), Volume 36*, 1994.

54. Yushin, N. K., Tarakanov, E. A. and Smirnova, E. P., "Acoustical Properties of Ferroelectric Ceramics with Diffuse Phase Transition", *Ferroelectrics, Volume 158*, 1994.

55. Isupov, V. A., Yushin, N. K., Smirnova, E. P., Sotnikov A. V., Tarakanov, E. A., and Maksimov, A. Yu., "Electrostrictive Actuators on Base of PMN – PSN Solid solution Ceramics", *Ferroelectrics, Volume 160*, 1994.

56. Martin G., Tarakanov, E. A., Weihnacht, M. and Yushin, N. K., "SAW Filter Resonant Frequency Adjustment by Electrostrictive and Piezoelectric Actuators", *Ferroelectrics Letters, Volume 17*, 1994.

57. Pronin, I. P., Rotenberg, B. A. and Tarakanov, E. A., "Electrostrictive Transducer Based on Barium Titanate-Zirconate Ceramics", *Pisma Zh. Tekh. Fiz. (Technical Physical Letters), Volume 22*, 1996.

58. Robinson, Harold c., "Methods of Calculating Coupling Coefficients for Electrostrictive Materials", *ASA 132nd Meeting, Hawaii*, December 1996.

59. Robinson, Harold C., "A New One-Dimensional Model for Electrostrictive Materials", *ASA 132nd Meeting, Hawaii*, December 1996.

60. Yamwong, T., Voice, A. M., Davies, G. R., Cochlin, R. L. and Feast, W. J., "Electrostrictive Elastomers – Artificial Muscles", 1999.

61. Jacob Aboudi, Smart Materials & Structures, Vol. 8, 663-671, 1999

62. Clark, A. E., "Magnetostrictive Rare Earth Fe_2 Compounds", *Ferromagnetic Materials, Volume 1*, North Holland Publishing Company, 1980.

63. Sewell, J. M., "Principles of Applicable to Terfenol Devices", *Proceedings of the First International Terfenol Conference on Giant Magnetostrictive Alloys*, Marbell, Spain.

64. Reddy, J N and Barbaso, JI, Smart Materials & Structures, Vol. 9, 49-58, 2000.

65. Grimes, C A et al, Smart Materials & Structures, Vol. 8, 639-646, 1999.

66. Barandiaran, J M and Gutierrez, Sensors and Actuators, A59, 38-42, 1997.

67. Calkins, F T and Flatan, A B, "Terfenol-D Sensor Design and Optimization", Journal of Noise Control Engineering, 1999.

68. Hall, D, "Dynamics and Vibrations of Magnetostrictive Transducers", PhD Dissertation, Iowa State University, 1995

69. Pratt, J and Flatan, A, Journal of Intelligent Material Systems and Structures, Vol 6, 639-648, 1995

70. Calkins, F T, Smith, R C and Flatan, A B, "An Energy Based Hysteresis Model for Magnetostrictive Transducers", IEEE Transactions on Magnetics, 1999

71. F Brailsford, "Physical Principles of Magnetism", D van Nostrand Company, London, 1966.

72. S Guruswamy et al, Scripta Materialia, 2000, pp 239-244.

73. H Kwun, K A Bartels, 1998, pp171-178.

74. **B Burton**, V Verijenko, C J von Klemperer, S Adali, "Smart Strain Sensor" International CARS and FOF, July 2001, Durban, South Africa.

75. **B Burton**, V Verijenko, "Structural health monitoring in marine structures", OMAE, June 2002, Oslo, Norway

76. V Verijenko, **B Burton**, "Smart Materials for structural health monitoring" ESDA, July 2002, Istanbul, Turkey.

77. V Verijenko, **B Burton**, S Shaik, "Smart materials for early damage detection", Fracture Mechanics, September 2002, Hawaii, USA

78. O E Schmid, R D Knutsen, "Reducing the Nickel Content in Metastable Austenitic Stainless Steel", Proceedings of the 1st international Chromium Steel and Alloys Congress, Cape Town, Vol.2, 1992, pp 151-156.

79. D P Roberts, "Testing of Mining Tunnel Support Elements and Systems for Hard Rock Mines", MSc thesis, University of Natal, 1995.

80. G Guler et al, "Definition of Systems Criteria, Technology Search and Evaluation for Access in the Depth Ranges of 3 to 4 km and 4 to 5 km" Deep Mine project report for Miningtek, September 1999

81. T R Stacey, "Reliable, cost effective techniques for ground stress measurement in deep gold mines" Steven, Robertson &Kirsten, SIMBAC, 1995.

82. A V Z Brink, T O Hager, "Survey and Assessment of techniques used to Quantify the Potential for Rockmass Instability", CSIR Miningtek, 2000.

83. A T Haile, T Jager, "Support for tunnels in defferent layout and stress regimes" CSIR Miningtek.

84. C Bemont, S Gray, D van Wyk, S Vilakazi, "Smart Stran Sensor" final year project report, University of Natal, 2001.

85. A Cichowics, "Rockfalls and rockburst" Wits University, 1994

86. A Chicowics, "A quantitative behaviour of rockmass in deep mines" SIMRAC report

87. R J Durrheim, A Miller, "Investigation at site response to rockburst", CSIR 1998

88. M Roberts, G Guler, G Quaye, "Improved support design", CSIR, 1996

89. http://www.steeledalescs.co.za/products.htm

90. www.tunnelintelligence.com

91. www.jkmrc.uq.edu

92. www.arcsandsparks.com

93. www.faraday.ukc.ac.uk

94. H D Young, "University Physics", 8th edition, Addison Wesley, 1992.

95. www.gaussmeter.com

96. www.fwbell.com

97. R Noble, "Fluxgate magnetometry", Electronics World & Wireless World, September 1991.

98. F Prindhal, Journal of Physics, 242 – 253, 1979

99. C J Perllerin, "A miniature two-axis fluxgate magnetometer, NASA technical, NASA, 1970.

100. www.vanderbit.edu

101. www.physics.monash.edu.au

102. www.ndt.net

103. www.maclab.alfred.edu

104. www.measurementsgroup.com

105. www.physics.mun.ca

106. J Clark, "SQUIDS" Scientific American, 46 – 53, August 1994.

107. S A Macintyre, "Magnetic Field Measurement", Electronic Design Journal, 1998.

108. E Olsen, "Applied Magnetism: A Study in quantities", Phillips Technical Library, 1966, Eindhoven.

109. D Bates, P Naidoo, S Shabane, "Smart Composites", final year project report 2002, Univeristy of Natal

110. SABS standard 1408, Pretoria, 2002.

111. J Lefevre, R Tricot, A Gueussier, R Castro, Metallurgical transactions, vol. 5, 1974, pp 2277 – 2285

112. V F Zackay, W J Justussin, D K Schmatz, "Strengthening by Martensitic Transformations", 1960.

113. G M Wayman, J E Hanafee, T A Read, Acta Metallurgica, vol. 9, 1961, pp 391 – 402.

114. R G Stringfellow, D M Parks, G B Olson, Acta Metallurgica, vol. 40 no. 7, 1992, pp 1703 – 1716.

115. V I Levitas, A V Idesman, G B Olson, Acta Metallurgica, vol. 47 no. 1, 1999, pp 219 – 233.

116. J S Bowles, J K MacKenzie, Acta Metallurgica, vol. 10, 1962, pp 625 – 635.

117. C J Gutner, R P Reed, Transactions of the ASM, vol. 55, 1962, pp 399 – 419.

118. I Tamura, T Maki, H Hato et al, "Strength and Ductility of Austenitic Iron Alloys accompanying Strain-Induced Martensitic Transformation", Conference, 1970, pp 900 – 904.

119. W S Owen, "Strengthening by Phase Transformation", Second International Conference of Strength of materials, Pacific Grove California, 1970, pp 795 – 814

120. R G Davies, C L Magee, "On the Occurrence of the Various Martensite Morphologies", Conference, 1970, pp 817 – 821.

121. J M Drapier, P Viatour, D Coutsouradis, L Habraken, "Hardening Mechanisms in Multiphase Alloys", Conference, 1970, pp 830 – 834.

122. F A Crossby, R W Lindberg, "Microstructural Analysis of a High Strength Martensite-Beta Ti Alloy", Conference, 1970, pp 841 – 845.

123. W B Morrison, "Plastic Instability During Luders Deformation in Ultrafine-Grained, Low Carbon Ferritic Steel", Conference, 1970, pp 879 – 883.

124. H Smith, D R F West, "The Strengthening of Stainless Steels by the Reverse Martensite Transformation", Conference, 1970, pp 892 – 893.

125. F Abrassart, F Lecroissey, A Pineau, "Martensitic Transfomrations and Plasticity in the Fe-Ni-Cr-C System", Conference, 1970, 905 – 921.

126. G F Bolling, R H Richman, Acta Metallurgica, vol. 18, 1970, pp 673 – 681.

127. D Goodchild, W T Roberts, D V Wilson, Acta Metallurgica, vol. 18, 1970, pp 1137 – 1145.

128. R A McCoy, W W Gerberich, V F Zackay, Metallurgical Transactions, vol. 1, 1970, pp 2031 – 2034.

129. D Hennessy, G Steckel, C Altstetter, Metallurgical Transactions, vol. 7A, 1976, pp 415 – 424.

130. M Arzin, G B Olson, R A Gagne, Materials Science and Engineering, vol. 23, 1976, pp 33 – 41.

131. G B Olson, M Arzin, H E Band, "AC Permeability Measurement of Strain-Induced Martensite During Tensile Deformation of TRIP Steels", Army Materials and Mechanics Research Centre, Watertown, Massachussettes, 1977.

132. G B Olson, M Arzin, Metallurgical Transactions, vol. 9A, 1978, pp 713 – 721.

133. E H R Wade, C M Preece, Metallurgical Transactions A, vol. 9A, 1978, pp 1299 – 1310.

134. J P Bressanelli, A Moskowitz, Transactions of the ASM, vol. 59, 1966, pp 223 – 239.

135. W W Gerberich, G Thomas, E R Parker, V F Zackay, "Metastable Austenites: Decomposition and Strength", Conference, 1970, pp 894 – 899.

136. G R Chanani, S D Antolovich, W W Gerberich, Metallurgical Transactions, vol. 3, 1972, pp 2661 – 2672.

137. S D Antolovich, D Fahr, Engineering Fracture Mechanics, vol. 4, 1972, pp 133 – 144.

138. G W Form, M W Baldwin, Transactions of the ASM, vol. *, 1956, pp 474 – 485.

139. C Altstetter, M Rashid, "Defects and Strengthening in Transformed Crystals", Conference, 1970, pp 846 – 850.

140. A R Marder, G Krauss, "The Effect of Morphology on the Strength of Lath Martensite", Conference, 1970, pp 822 – 829.

141. V F Zackay, M D Bhandarkar, E R Parker, "The Role of Deformation Induced Phase Transformation in the Plasticity of Some Iron-base Alloys", 1978.

142. D Fahr, Metallurgical Transactions, vol. 2, 1971, pp 1883 – 1892.

143. V F Zackay, E R Parker, D Fahr, R Busch, Transactions of the ASM, vol. 60, 1967, pp 252 – 259.

144. G Thomas, D Schmatz, W Gerberich, "Ausform Steel", 1964.

145. W W Gerberich, C F Martin, V F Zackay, Transaction of the ASM, vol. 58, 1965, pp 85 – 94.

146. A G Crocker, Acta Metallurgica, vol. 13, 1965, pp 815 – 825.

147. V F Zackay, W W Gerberich, R Busch, E R Parker, "The Strength and Toughness of Dynamically Strain-Aged Alloy Steel Sheets",1965

148. A J Morton, C M Wayman, Acta Metallurgica, vol. 14, 1966, pp 1567 – 1581.

149. J A Hall, V F Zackay, E R Parker, Transactions of the ASM, vol. 62, 1969, pp 965 – 976.

150. E R Parker, V F Zackay, Engineering Fracture Mechanics, vol. 5, 1973, pp 147 – 165.

151. D A Woodford, Metallurgical Transactions, vol. 3, 1972, pp 1137 – 1145.

152. W W Gerberich, P L Hemmings, M D Merz, V F Zackay, Transactions of the ASM, vol. 61, 1968, pp 843 – 847.

153. W W Gerberich, P L Hemmings, V F Zackay, E R Parker, "Interactions Between Crack Growth and Strain-Induced Transformation", Conference, 1968, pp 288 – 305.

154. S D Antolovich Transactions of the Metallugical Soceity of the AIME, vol. 242, 1968, pp 2371 – 2373.

155. E Gold, T J Keppenaal, , Transactions of the ASM, vol. 62, 1969, pp 607 – 610.

156. E W Page, P Manganon, G Thomas, V F Zackay, Transactions of the ASM, vol. 62, 1969, pp 45 – 54.

157. V F Zackay, E R Parker, "Some Fundamental Considerations in Design of High-Strength Metallic Materials", 1964.

158. G Thomas, D Schmatz, W Gerberich, "Structure and Strength of Some Ausformed Steels", 1969.

159. M Cherkaoui, M Breveiller, "Mechanics of Materials undergoing Martensitic Phase Change: A Micro-macro Approach for Transformation Induced Plasticity".

160. M Niinomi, T Kobayashi, L Inagaki, A W Thompson, Metallurgical Transactions A, vol. 21A, 1990, pp 1733 – 1744.

161. E Arnold, "Steels: Microstructures and Properties", Metallurgy and Materials Science series,, RWK Honeycombe, 1981, pp55-56.

162. Smith, "Structure and Properties of Engineering Alloys", McGraw-Hill, New York, 1993.

163. A G Pineau, R M Pelloux, Metallurgical Transactions, vol. 5, 1974, pp 1103 – 1112.

164. D Bhandarkar, V F Zackay, E R Parker, Metallurgical Transactions, vol. 3, 1972, pp 2619 – 2631.

165. R D Knutsen, M Sibanda, "Evaluation of the Formability Properties of Nitrogen Alloyed Metastable Austenitic Stainless Steels", Proceedings of Stainless Steels '93 Processes and Materials Innovation, vol.3, Florence, AIM, 1993, pp3.333 – 3.342.

166. M Sibanda, S L Vismer, R D Knutsen, Materials Letters 21, 1994, pp 203 – 207.

167. T Biggs, R D Knutsen, Journal De Physique IV, vol. 5, 1995, pp C8-515 – C8-520.

168. D J Drobujak, J G Parr, Metallurgical Transactions, vol.1, 1970, pp 759 – 765.

169. T Angel, Journal of the Iron and Steel Institute, May 1954, pp 165 – 174.

170. D Webster, "Development of a high stresngth stainless steel with improved toughness and ductility", Metallurigical Transactions, vol. 2, 1971, pp 2097 – 2104.

171. J C Shyne, V F Zackay, D J Schamtz, Transactions of the ASM, vol. 52, 1960, pp 347 – 361.

172. G R Chanani, S D Antolovich, Metallurgical Transactions, 1974, pp 217 – 229

173. P C Maxwell, A Goldberg, J C Shyne, Metallurgical Transactions, vol. 5, 1974, pp 1305 – 1318.

174. A Z Hanzaki, P D Hodgson, S Yue, ISIJ International, vol 35 no.1, 1995, pp 79 – 85.

175. Z A Bryuthanova, V V Usov, N M Shkatulyak, Steel in Translation, vol 22, 1992, pp 79 – 82.

176. Sugimoto et al, ISIJ International, vol 33 no. 7, 1993, pp 775 – 782.

177. K Eberle, P Cantineaux, P H Harlet, Ironmaking and Steelmaking, vol. 26 no. 3, 1999, pp 176 – 181.

178. TJ Koppenaal, Metallurgical Transactions, vol. 3, 1972, pp 1549 – 1554.

179. G R Chanani, S D Antolovich, W W Gerberich, Metallurgical Transactions, vol. 3, 1972, pp 2661 – 2672

180. F Abrassart, Metallurgical Transactions, Vol. 4, 1973, pp 2205 – 2216.

181. G R Chanani, V F Zackay, E R Parker, Metallurgical Transactions, vol. 2, 1971, pp 133 – 139.

182. J R C Guimarares, R J De Angelis, Metallurgical Transactions, vol. 4, 1973, pp 2379 – 2381

183. D C Ludvigson, J A Berger, Journal of the Iron and Steel Institute, Jan 1969, pp 413 – 419

184. W W Gerberich, P L Hemmings, V F Zackay, Metallurgical Transactions, vol. 2, 1971, pp 2243 – 2253.

185. G B Olson, R Chait, M Arzin, R A Gagne, Metallurgical Transactions A, vol. 11A, Jne 1980, pp 1069 – 1071.

186. S D Antolovich, B Singh, Metallurgical Transactions, vol. 2, 1971, pp 2135 – 2141.

187. P C Maxwell, A Goldberg, J C Shyne, Metallurgical Transactions, vol. 5, 1974, pp 1319 – 132

188. U Krupp et al, "Deformation-induced martensite formation in metastable austenitic steels in dependence on the carbon content", Institut fur Werkstofftechnik, Universitat Siegen, Germany, 2002.

189. F Lesroisey, A Pineau, Metallurgical Transactions, 1972, pp 387 – 396.

190. L D Thompson, "The FCC to HCP to BCC Phase Transformation Sequence in Metastable Fe-Cr-Mn alloys"

191. C.N.R. Rao and K.J. Rao: Phase Transitions in Solids, McGraw-Hill Inc., New York, NY, 1978, pp. 100-7.
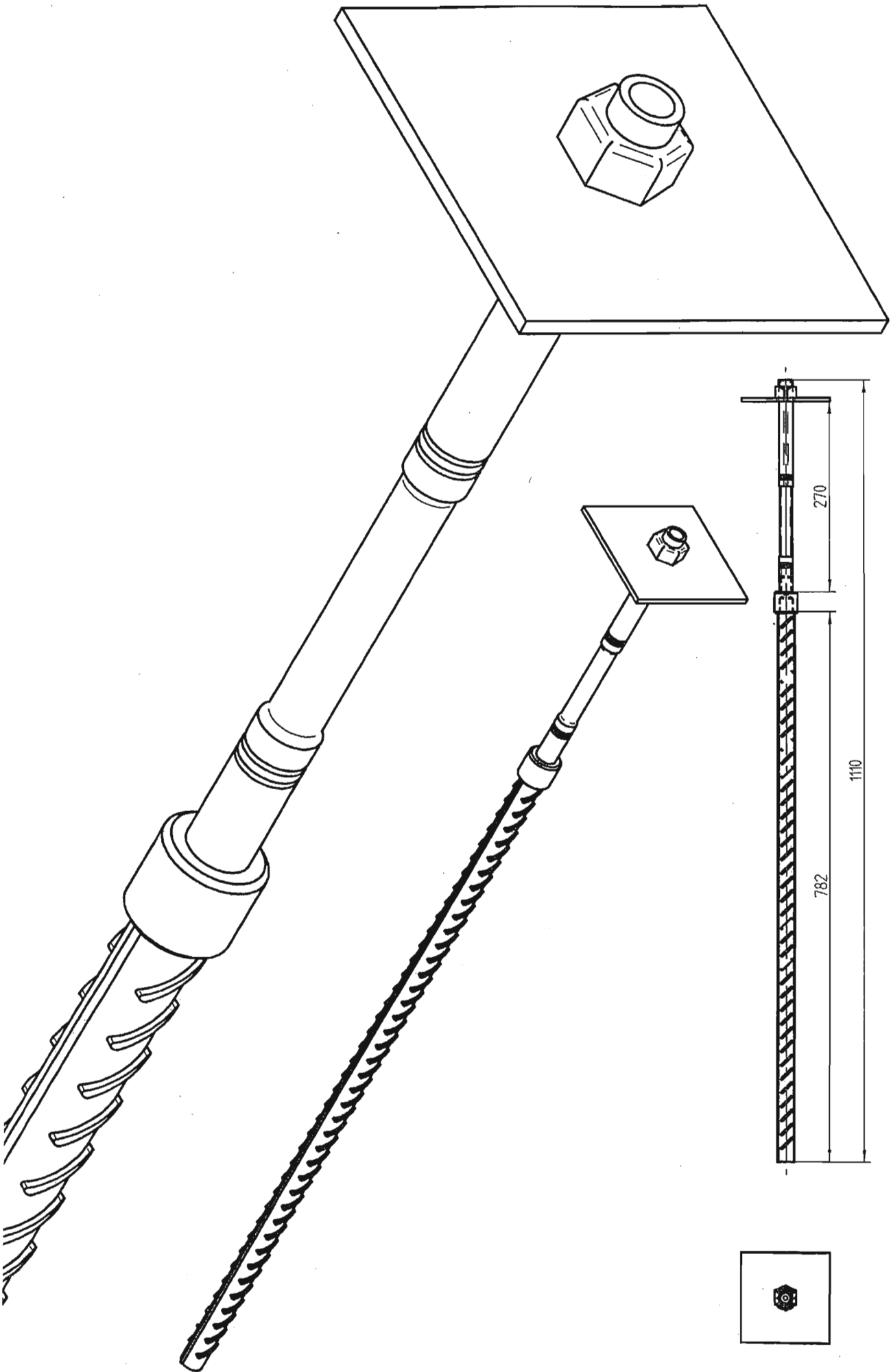
192. R.W.K. Honeycombe: Steels: Microstructure and Properties, Edward Arnold (Publishers)Ltd., London, 1981, pp. 90-4.

193. D.A. Porter and K.E. Easterling, Phase Transformations in Metals and Alloys, 2nd ed., Chapman & Hall, London, 1996, pp. 397-409.

194. G.B. Olson and M. Cohen: Metall. Trans. A, 1976, vol. 7A, pp. 1897-1904

195. G.B. Olson and M. Cohen: Metall. Trans. A, 1976, vol. 7A, pp. 1905-14.

196. G.B. Olson and M. Cohen: Metall. Trans. A, 1976, vol. 7A, pp. 1915-23.

197. J.G. Parr: J. Iron Steel Inst., 1952, vol. 171, pp. 137-41.

198. H.M. Otte: Acta Metall., 1957, vol. 5, pp. 614-27.

199. B. Cina: Acta Metall., 1958, vol. 6, pp. 748-62.

200. L. Remy: Metall. Trans. A., 1977, vol. 8A, pp. 253-8.

201. S.-H. Baik, J.C. Kim, K.K. Jee, W.Y. Jang and M.C. Shin: J. Phys. IV, Colloq., 1997, vol. 7, pp. 453-8

202. J.-H. Jun, S.-H. Baik, Y.-K. Lee and C.-S. Choi: Scripta mater., 1998, vol.39, pp. 39-44.

203. J.-H. Jun and C.-S. Choi: Mater. Sci. Eng. A, 1998, vol. 252A, pp. 133-8.

204. J-H. Jun and C.-S. Choi: J. Mater. Sci., 1999, vol. 34, pp. 3421-5.

205. A. Ariapour, I. Yakubtsov and D.D. Perovic: Mater. Sci. Engng. A, 1999, vol. 262A,   pp. 39-49.

206. C. Choi, T.K. Ha, H.C. Shin and Y.W. Chang: Scripta Mater., 1999, vol. 40, pp. 1171-7.

207. Cotes, A.F. Guillermet and M. Sade: Mater. Sci. Engng. A, 1999, vols. 273A-275A, pp. 503-6.

208. A. Baruj, A.F. Guillermet and M. Sade: Mater. Sci. Engng. A, 1999, vols. 273A-275A, pp. 507-11.

209. F. Gauzzi and R. Montanari: Mater. Sci. Engng. A, 1999, vols. 273A-275A, pp. 524-7.

210. Y.-K. Lee and C.-S. Choi: Metall. Mater. Trans. A, 2000, vol. 31A, pp. 355-60.

211. X. Lu, Z. Qin, Y. Zhang, B. Ding and Z. Hu: Scripta Mater., 2000, vol. 42, pp. 433-7.

212. A. Baruj, H.E. Troiani, M. Sade and A. Fernández Guillermet: Philos. Mag. A, 2000, vol. 80A, pp. 2537-48.

213. A. Baruj, A. Fernández Guillermet and M. Sade: J. Phys. IV, Colloq., 1997, vol. 7, pp. 405-10.

214. J.-H. Jun and C.-S. Choi: J. Maters. Sci. Lett., 1998, vol. 17, pp. 629-31.

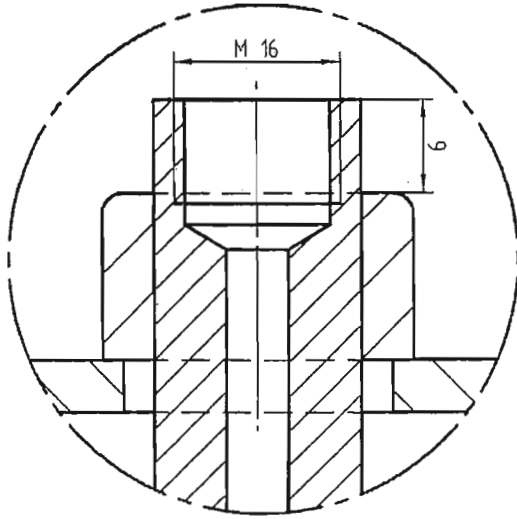215. J.-H. Jun, D.-K. Kong and C.-S. Choi: Mater. Res. Bull., 1998, vol. 33, pp. 1419-25.

216. L.D. Thompson: Mechanical Properties and Phase Transformations in Engineering Materials, The Metallurgical Society, Inc., Warrendale, Pa, 1986, pp. 391-408.

217. T.N. Durlu: J. Maters. Sci. Lett., 1997, vol. 16, pp. 320-1.

218. T.N. Durlu: J. Mater. Sci., 1999, vol. 34, pp. 2887-90.

219. A. Sato, Y. Yamaji and T. Mori: Acta Metall., 1986, vol. 34, pp. 287-94.

220. M. Andersson, R. Stalmans and J. Ågren: J. Phys. IV, Colloq., 1997, vol. 7, pp. 411-6.

221. A.Yu. Pasko, A.A. Likhachev, Yu.N. Koval and V.I. Kolomytsev: J. Phys. IV, Colloq., 1997, vol. 7, pp. 435-40.

222. G. Guénin: J. Phys. IV, Colloq., 1997, vol. 7, pp. 467-76.

223. M. Andersson, R. Stalmans and J. Ågren: Acta mater., 1998, vol. 46, pp. 3883-91.

224. S. Cotes, A. Fernández Guillermet and M. Sade: J. Alloys Compd., 1998, vol. 278, pp. 231-8.

225. Z. Guo, Y. Rong, S. Chen and T.Y. Hsu (Xu Zuyao): Scripta Mater., 1999, vol. 41, pp. 153-8.

226. B. Jiang and X. Qi: Bull. Mater. Sci. (India), 1999, vol. 22, pp. 717-21.

227. Z. Guo, Y. Rong, S. Chen, T.Y. Hsu (Xu Zuyao), J. Hong and X. Zhao: Mater. Trans. JIM, 1999, vol. 40, pp. 193-8.

228. T.Y. Hsu (Xu Zuyao): Mater. Sci. Engng. A, 1999, vol. 273A-275A, pp. 494-7.

229. H. Li, D. Dunne and N. Kennon: Mater. Sci. Engng. A, 1999, vol. 273A-275A, pp. 517-23.

230. O. Grässel, G. Frommeyer, C. Derder and H. Hofmann: J. Phys. IV, Colloq., 1997, vol. 7, pp. 383-8.

231. W.Y. Jang, J.I. Han, K.K. Jee, S.H. Baik, J.W. Kang and M.C. Shin: J. Phys. IV, Colloq., 1997, vol. 7, pp. 447-52.

232. N. Bergeon, G. Guénin and C. Esnouf: J. Phys. IV, Colloq., 1997, vol. 7, pp. 125-30.

233. N. Bergeon, G. Guénin and C. Esnouf: Mater. Sci. Eng. A, 1998, vol. 242A, pp. 77-86, 87-95.

234. F. Nishimura, N. Watanabe and K. Tanaka: Mater. Sci. Eng. A, 1998, vol. 247A, pp. 275-84.

235. Q. Liu, Z. Ma and N. Gu: Metall. Mater. Trans. A, 1998, vol. 29A, pp. 1579-83.

236. G.J. Arruda, V.T.L. Buono, M.S. Andrade: Mater. Sci. Engng. A, 1999, vol. 273A-275A, pp. 528-32.

237. J.C. Li, M. Zhao and Q. Jiang: Metall. Mater. Trans. A, 2000, vol. 31A, pp. 581-4.

238. N. Bergeon, S. Kajiwara and T. Kikuchi: Acta mater., 2000, vol. 48, pp. 4053-64.

239. L. Remy and A. Pineau: Mater. Sci. Engng., 1977, vol. 28, pp. 99-107.

240. S. Aktürk, A. Gencer and T.N. Durlu: J. Maters. Sci. Lett., 1997, vol. 16, pp. 389-91.

241. W.O. Binder: Metal. Prog., 1950, vol. 58, pp. 201-7.

242. B. Cina: J. Iron Steel Inst., 1954, vol. 177, pp. 406-22.

243. J.A. Venables: Phil. Mag., 1962, vol. 7, pp. 35-44.

244. R.P. Reed: Acta Metall., 1962, vol. 10, pp. 865-.

245. J.F. Breedis and W.D. Robertson: Acta Metall., 1962, vol. 10, pp. 1077-88.

246. J. Dash and H.M. Otte: Acta Metall., 1963, vol. 11, pp. 1169-.

247. A.J. Goldman, W.D. Robertson and D.A. Koss: Trans. AIME, 1964, vol. 230, pp. 240-1.

248. J.F. Breedis: Trans. AIME, 1964, vol. 230, pp. 1583-96.

249. R.P. Reed and C.J. Guntner: Trans. AIME, 1964, vol. 230, pp. 1713-20.

250. H. Fujita and S. Ueda: Acta Metall., 1972, vol. 20, pp. 759-67.

251. J.W. Brooks, M.H. Loretto and R.E. Shallman: Acta Metall., 1979, vol. 27, pp. 1828-38, 1839-47.

252. J.W. Christian: Proc. Roy. Soc. A, 1951, vol. 206, pp. 51-64.

253. C.R. Houska, B.L. Averbach and M. Cohen: Acta Metall., 1960, vol. 8, pp. 81-7.

254. E. Votava: Acta Metall., 1960, vol. 8, pp. 901-4.

255. F. Frey and H. Boysen: Acta Crystallogr. A, 1981, vol. 37A, pp. 819-26.

256. C. Hitzenberger, H.P. Karnthaler and A. Korner: Acta Metall., 1985, vol. 33, pp. 1293-305.

257. P. Huang and H.F. López: Mater. Letters, 1999, vol. 39, pp. 244-8, 249-53.

258. A.de J. Saldívar García, A. Maní Medrano and A. Salinas Rodríguez: Metall. Mater. Trans. A, 1999, vol. 30A, pp. 1177-84.

259. S. Mahajan, M.L. Green and D. Brasen: Metall. Trans. A, 1977, vol. 8, pp. 283-93.

260. T. Waitz and H.P. Karnthaler: Phys. stat. sol. (a), 1998, vol. 166, pp. 107-14.

261. C. Hitzenberger, H.P. Karnthaler and A. Korner: Acta Metall., 1988, vol. 36, pp. 2719-28.

262. C. Hayzelden, K. Chattopadhyay, J.C. Barry and B. Cantor: Phil. Mag. A, 1991, vol. 63, pp. 461-70.

263. T. Waitz and H.P. Karnthaler: Acta mater., 1997, vol. 45, pp. 837-47.

264. A.L. Roitburd: Soviet Phys. Dokl., 1981, vol. 26, pp. 92-4.

265. I-W. Chen and Y.-H. Chiao: Acta Metall., 1985, vol. 33, pp.1827-45.

266. V.I. Levitas, A.V. Idesman and G.B. Olson: Acta Metall., 1999, vol. 47, pp. 219-33.

267. J.V. Lill and J.Q. Broughton: Phys. Rev. Lett., 2000, vol. 84, pp. 5784-7.

268. J. Ronda and G.J. Oliver: Comput. Methods Appl. Mech. Engrg., 2000, vol. 189, pp. 361-417.
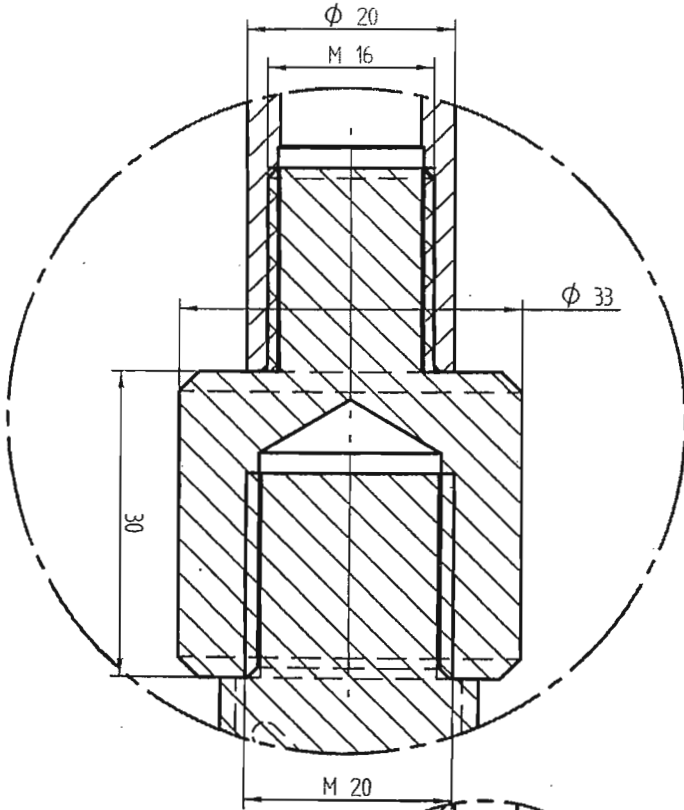
269. M.Yu. Gutkin, K.N. Mikaelian and V.E. Verijenko: University of Natal, Durban, South Africa, unpublished research, 2001.

270. H.I. Aaronson and M.G. Hall: Metall. Mater. Trans. A, 1994, vol. 25A, pp. 1797-819.

271. A.E. Romanov and V.I. Vladimirov: Dislocations in Solids, vol. 9, North Holland, Amsterdam, 1992, pp. 191-402.

272. J.W. Cahn: Acta metall., 1957, vol. 5, pp. 169-72.

273. M.Yu. Gutkin and I.A. Ovid'ko: Philos. Mag. A, 1994, vol. 70A, pp. 561-75.

274. M.Yu. Gutkin, K.N. Mikaelyan and I.A. Ovid'ko: Sov. Phys. - Solid State (USA), 1995, vol. 37, pp. 552-4.

275. M.Yu. Gutkin, I.A. Ovid'ko and K.N. Mikaelyan: NanoStruct. Maters., 1995, vol. 6, pp. 779-82.

276. M.Yu. Gutkin, K.N. Mikaelyan and I.A. Ovid'ko: Phys. stat. sol. (a), 1996, vol. 153a, pp.337-46.

277. M.Yu. Gutkin, A.E. Romanov and P. Klimanek: Local Lattice Rotations and Disclinations in Microstructures of Distorted Crystalline Materials (Proc. Intern. Workshop, Raushenbach/Erzgebirge, Germany, April 10-14, 2000), pp. 00-00.

278. J.P. Hirth and J. Lothe: Theory of Dislocations, John Wiley, New York, 1982.

279. A Harillal, N Venter, S Mthimkulu, "Casting and Processing of Metastable Alloys", Final year project report, University of Natal, 2002.

280. G W Powell, E R Marshall, W A Backofen, "Strain Hardening f Austenitic Stainless Steel", Transactions of the ASM, sol. 50, 1958, pp 478 – 497.
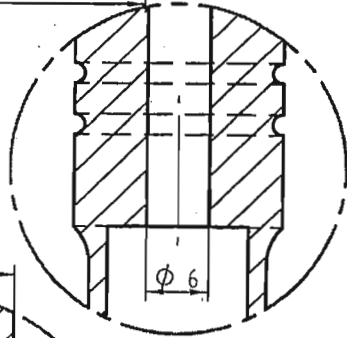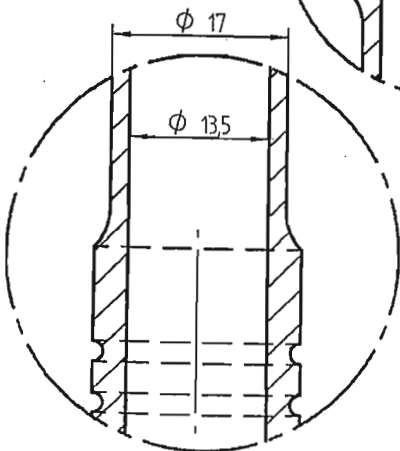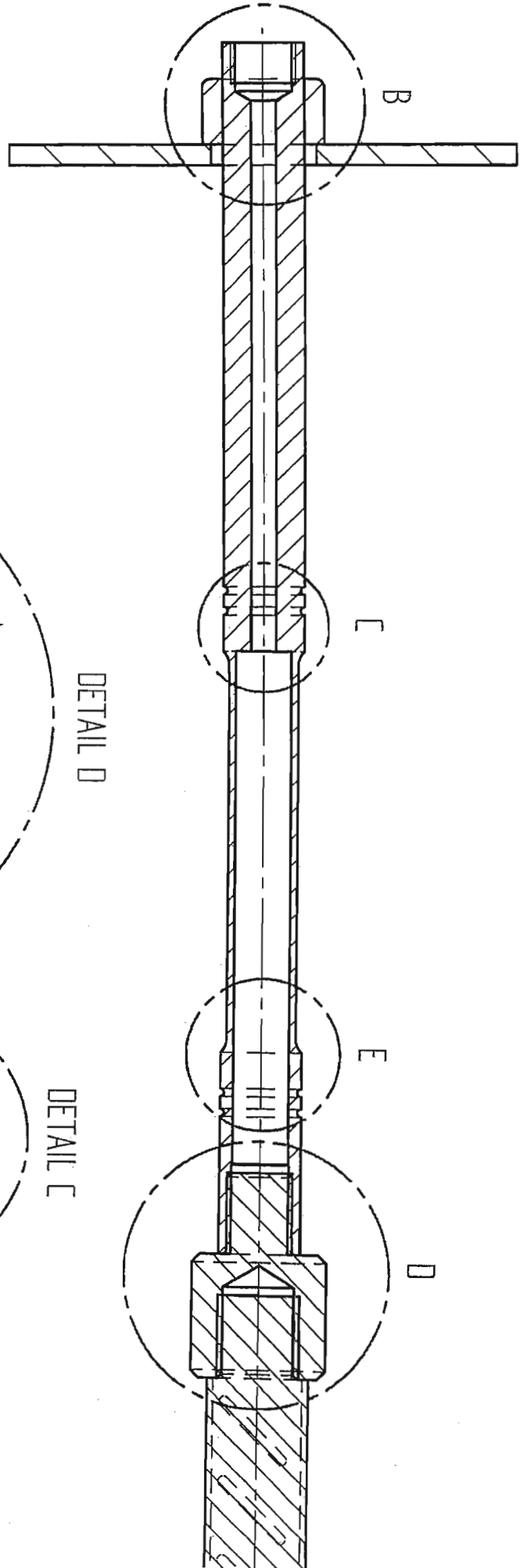
APPENDIX A

270

1110

782

M 16

9

DETAIL B

Ø 20

M 16

Ø 33

DETAIL D

30

M 20

DETAIL C

Ø 6

Ø 17

Ø 13,5

DETAILE

B

C

E

D

M 16

R 1

50

30

22

20

M 20

Ø 33

2 2 chamfers

SECTION A-A

A

A

SECTION A-A

M 20

300

5
10

100

50

35

22,5

20

M 16

Ø 20

A — A

DETAIL C

M 16

12

10

DETAIL B

Ø 17

Ø 13,5

R 5

5

4 x R 1